DISS. ETH NO. 19408

THREE-DIMENSIONAL PAIR DISTRIBUTION FUNCTION ANALYSIS OF DISORDERED CRYSTALS

A dissertation submitted to
ETH ZÜRICH

for the degree of
Doctor of Sciences

presented by
PHILIPPE ROGER SCHAUB
Dipl. phil. II, University of Basel

born 3rd June 1978
citizen of Rünenberg (BL)

accepted on the recommendation of

Prof. Dr. Walter Steurer, ETH Zürich
Prof. Dr. Reinhard Neder, University of Erlangen
Dr. Thomas Weber, ETH Zürich

2010

Summary

Structural disorder is naturally present in many crystals. To date, there is still need for applicable and straightforward single-crystal methods to analyse the local structure of disordered crystals. The new methods *three-dimensional* (3D) *Pair Distribution Function* (PDF) analysis and, in particular, *three-dimensional* Δ*PDF* (3D-ΔPDF) analysis are introduced. Based on 3D interatomic vectors, the presented approach is straightforward and illustrative, because 3D-PDFs can be directly linked with the real crystal structure. The 3D-ΔPDF allows the investigation of short- and medium-range disorder phenomena. It is a finite function, which is restricted by a maximum correlation length, thus there is no need for concepts in order to emulate infinite crystal structures. Selective interpretation and modelling of only parts of the local structure is possible. Further, multiple independent disordered motifs, which occur uncorrelated to each other at different places in a real structure, can be handled simultaneously as well. In contrast to state-of-the-art methods used for characterisation and modelling of disorder, which are based on diffuse scattering intensities in reciprocal space, the 3D-PDF approach has the advantage that the structural information provided by the PDF has the same metrics as the underlying crystal structure. Furthermore, structural information carried by specific atomic pairs appears in the 3D-PDF at well-defined and confined positions, and can therefore be measured or filtered in a straightforward way. In reciprocal space this information is continuously spread throughout the whole diffraction pattern.

The application of 3D-ΔPDF analysis is demonstrated on two studies of disordered materials. Illustrated by *N,N',N''*-tris-*t*-butyl-1,3,5-benzene tricarboxamide, qualitative 3D-PDF analysis is used to elucidate the proximity relationships of chiral molecular columns, which occur in two different helical hands. PDF analysis revealed a systematic preference to heterochiral arrangements of molecules. The second example is the interpretation of the 3D-ΔPDF of a decagonal Al–Cu–Co quasicrystal. A structural model of disorder for the twofold (~8 Å) superstructure is presented. The superstructure was found to be built from columnar units, having a maximum diameter of ~14.5 Å. The lateral correlation between these columns is weak. Internally, the columns consist of a long-range ordered alternation of flat and puckered layers. The differential evolution method was used to optimise this model. The obtained model is solely based on geometrical assumptions, without using any constraints on chemical or physical structural properties.

In addition, practical aspects of the ΔPDF method, including data collection, processing and filtering, are given. Extensive investigations were made on performance and reliability of differential evolution optimisation on ΔPDF densities of the structural model of the Al─Cu─Co quasicrystal.

Zusammenfassung

Fehlordung ist ein verbreitetes Phänomen in vielen Kristallstrukturen. Dennoch gestaltet sich die Auswertung fehlgeordneter Stukturen schwierig, und es gibt nur wenige ausgereifte Einkristall-Methoden zur Untersuchung von Fehlordnung, welche zumeist auf der Simulation diffuser Röntgenbeugungsintensitäten im reziproken Raum basieren. Die in dieser Arbeit vorgestellten Methoden der dreidimensionalen (3D) Paarverteilungsfunktions-Analyse (*Pair Distribution Function* (PDF) *analysis*), und im speziellen der daraus abgeleiteten 3D-ΔPDF-Analyse, beruhen hingegen auf der Auswertung interatomarer Paarkorrelationen. Da die Metrik des Korrelationsraumes identisch ist mit derjenigen des Realraumes, lassen sich die aus der PDF gewonnenen Informationen leicht in die Realstruktur des untersuchten Kristalls übertragen. In der ΔPDF-Methode werden Paarkorreltionen der periodischen Fernordnung ausgeblendet, so dass die Interpretation der verbliebenen Korrelationen Auskunft über die Fehlordnung im kurzen und mittleren interatomaren Distanzbereich gibt. Die 3D-ΔPDF wird in ihrer Ausdehnung durch eine maximale Korrelationslänge limitiert, so dass die Untersuchungen auf ein begrenztes Datenvolumen beschränkt werden können. 3D-ΔPDF-Analyse bietet überdies die Möglichkeit der selektiven und unabhängigen Auswertung und Interpretation von Teilstrukturen der Realstruktur. Ferner ist es möglich, zur gleichen Zeit mehrere unkorrelierte Teilbereiche der Realstruktur zu simulieren. Strukturinformationen im ΔPDF-Raum sind einfach zu interpretieren, weil sich die Beiträge eines einzelnen Atompaares auf wenige, bestimmbare Orte im Korrelationsraum konzentrieren und nicht wie im reziproken Raum über das ganze Volumen verteilt sind.

Die praktische Anwendung der 3D-ΔPDF-Analyse wird an zwei Beispielen fehlgeordneter Strukturen besprochen. Anhand des ersten Beispieles, *N,N',N''*-tris-*t*-butyl-1,3,5-Benzentricarboxamid, werden die Möglichkeiten der qualitativen 3D-ΔPDF-Analyse aufgezeigt. In dieser organischen Verbindung treten säulenförmig angeordnete Moleküle unterschiedlicher Händigkeit auf, welche in auf Bragg-Streuung abgestützten Strukturlösungen nicht voneinander unterschieden werden können. Mittels 3D-ΔPDF-Anlyse konnte bestätigt werden, dass eine heterochirale Vorzugsorientierung aneinandergrenzender Molekül-Säulen vorherrscht.

Eine zweite Studie befasst sich mit der zweifachen, fehlgeordneten Überstruktur von dekagonalem Al–Cu–Co. Das gefundene Fehlordnungsmodell beschreibt den Quasikristall entlang seiner periodischen Achse über säulenartige Strukturmotive, welche einen Durchmesser von etwa 14.5 Å aufweisen. Intern zeigen diese Strukturelemente deutliche Fehlordnung, währenddem sie gegenseitig lateral nur schwach korreliert sind. Die Säulen werden als eine Abfolge von flachen und von mit internen Vertikalversätzen behafteten Schichten interpretiert. Der Translationsvektor entlang der periodischen Achse wird lokal von ~4 Å in der mittleren Struktur auf ~8 Å im fehlgeordneten Strukturmotiv verdoppelt. Das fehlgeordnete Strukturmotiv wurde mittels des Verfahrens der differentiellen Evolution optimiert. Die Optimierung beruhte dabei ausschliesslich auf der 3D-ΔPDF, und es wurden keine chemischen oder physikalischen Modellparameter und Randbedingungen verwendet.

Über die Diskussion der erwähnten fehlgeordneten Strukturen hinaus werden praktische Aspekte zur Anwendung der 3D-PDF-Methode besprochen, wie z.B. die Messung und Aufbereitung der experimentellen Röntgenbeugungsdaten, das Filtern von Daten im reziproken und im PDF-Raum, sowie die rechnergestützte Umsetzung der benötigten Fourier-Transformationen. Im weiteren wird die Genauigkeit und Verlässlichkeit der ΔPDF-Modellierung (auch von partiellen Modellen), sowie die Optimierung mit differentieller Evolution ausführlich diskutiert.

Contents

Summary ii

Zusammenfassung iv

1. Introduction 1

2. Fundamentals 5

  2.1. Structural Disorder 6

    2.1.1. Real structures and average structures 6

    2.1.2. Bragg scattering from ordered and average crystal structures 7

    2.1.3. Diffuse scattering from disordered crystal structures 8

    2.1.4. Pair Distribution Function analysis 9

    2.1.5. One-dimensional PDF analysis of crystalline powder samples 11

    2.1.6. Disorder in quasicrystals 12

    2.1.7. Reciprocal space vs. PDF space methods 13

  2.2. Average-Structure Solution with Patterson Methods 14

    2.2.1. The Patterson function 14

    2.2.2. Harker lines and sections 15

    2.2.3. The heavy atom method 16

    2.2.4. Special applications of Patterson methods 16

  2.3. Real-structure Solution Based on Single-Crystal Diffraction 17

    2.3.1. Analytical mathematical expressions 17

    2.3.2. Infinite series expansions 17

    2.3.3. Monte Carlo methods 18

3. Exploring Local Disorder in Single Crystals by Means of the Three-Dimensional Pair Distribution Function 21

  Appendix 3.A: Addendum to bibliography 30

  Appendix 3.B: Supplementary 3D-ΔPDF data 30

4. Analysis and Modelling of Structural Disorder by the Use of the Three-Dimensional Pair Distribution Function Method Exemplified by the Disordered Twofold Superstructure of Decagonal Al–Cu–Co 33
Appendix 4.A: Decagonal rod groups 51
Appendix 4.B: Burkov's model 51
5. Practical Aspects of 3D-PDF and 3D-ΔPDF Analysis 55
5.1. Experimental impacts 56
5.2. Data quality enhancement 57
5.3. Bragg peak elimination 69
5.4. Fourier transform 71
5.5. Implementation note on Fourier Transforms 72
6. Practical Aspects of 3D-ΔPDF Modelling 75
6.1. Analysis of the sensitivity of ΔPDF models to PDF space resolution 76
6.1.1. Objective and method 76
6.1.2. Results and discussion 80
6.2. Comparative study of different partial models 82
6.2.1. Investigated models 82
6.2.2. Results and discussion 83
6.3. Analysis of the evolution of residual values and free model parameters during optimisation process 93
6.4. Model optimisation in reciprocal space 96
6.4.1. Objective and method 96
6.4.2. Results and discussion 101
6.5. Model optimisation via an alternative fitness function 102
6.5.1. The structural similarity index 102
6.5.2. Results and discussion 104
7. Summary & Outlook 107
7.1. 3D-ΔPDF analysis and modelling 108
7.2. Total scattering 3D-PDF analysis and modelling 109
7.3. Disorder in *N,N',N''*-tris-*t*-butyl-1,3,5-benzene tricarboxamide 110
7.4. Disorder in *d*-Al–Cu–Co and other decagonal quasicrystals 110
References 113
Acknowledgements 117

1. Introduction

1. INTRODUCTION

In early times of modern crystallography, *i.e.* in the first half of the 20th century, crystallographers used to describe their objects of interest as perfect infinite objects, uniformly built up by small unit cells, each identical to the other. Since then, plenty of experimental methods to substantiate this concept of ideal crystal structures were developed and continuously enhanced. All the same, it was realised soon that real crystals are not as perfect as primarily imagined, but that they show in reality a variety of deviations from their ideal structure in the form of defects and disorder. Early publications dealing with disordered crystal structures and the related diffuse scattering phenomena are, for instance, von Laue (1918), von Laue (1941, pp. 175ff.), Hendricks & Teller (1942), Lonsdale (1948), Guinier & Griffoul (1948), just to mention a few prominent examples. This general interest in disordered crystal structures notwithstanding, investigations remained limited for a long period, because experimental equipment to measure weak diffuse scattering intensities within an acceptable time frame was not available, theoretical concepts were inadequate, and the huge data volume for an in-depth analysis of disordered systems could not be processed with the resources of that time.

Only with recent advances in experimental equipment, such as fast and sensitive area detectors, it has nowadays become possible to scan reciprocal space area-wide and fast, and in this way to detect even weakest diffuse scattering intensities. Modern, fast, and powerful computers facilitate data processing and evaluation. As a result, disorder is reported from many crystals, sometimes prominent, sometimes scarcely observable.

Even if its name is contradictory, structural disorder is far away from being a cumbersome structural feature, disturbing the perfect infinite order of crystals. Disorder is an intrinsic part of crystalline structures, and detailed knowledge about local structural units of the real structures is an important key to the understanding of energetic and entropic stabilisation and atomic interactions within a crystal structure. For a detailed introduction into structural disorder refer *e.g.* to Welberry & Butler (1995), Frey (2003), Welberry (2009). Structural disorder is always associated with the occurrence of diffuse scattering (see section 2.1.3). Different kinds of disorder are known: displacive, substitutional or orientational disorder, domain-like ordering or disorder in composite structures, just to mention a few. Disorder that is time-invariant is grouped under the term *static disorder*. In contrast, thermal vibrations and rotations, or movements of ordered micro-domains within a crystal structure are time-dependent, *dynamic (or thermal) disorder* (for an overview see *e.g.* Welberry, 2009; Egami & Billinge, 2003, pp. 249ff). The focus in this work will be on a static interpretation of disorder, although disorder analysed by the discussed PDF methods can also have a dynamic origin.

By the discovery of more and more complex crystalline structures, having, *e.g.*, unit cells comprising up to several thousands of atoms, or aperiodic crystal structures, the concept of simple ordered unit cell based crystal structures became insufficient for a complete structural understanding and description. In many crystal structures, the free energy is reduced by local deviations from the idealised structure, which are not periodic on a long-range scale. Thus, disorder plays an important role in stabilisation of crystal structures. Furthermore, many properties of materials, such as optical properties, hardness, conductivity and superconductivity, or magnetic properties, are governed by disorder. For these reasons, enhanced methods for investigation of disorder became more and more important. Astonishingly, there are only a few methods for analysis and modelling of structural disorder (see sections 2.1.5 and 2.3). In this thesis, theoretical concepts and the practical application of *three-dimensional* (3D*) Pair Distribution Function* analysis, and particularly its variant, *three-dimensional* Δ*PDF* (3D-ΔPDF) analysis, are presented for investigation, characterisation, and modelling of disorder in single crystals.

2. Fundamentals

2. FUNDAMENTALS

2.1. Structural Disorder

2.1.1. Real structures and average structures

Important terms used in the framework of PDF analysis are *average structure*, *real structure* and *difference structure*. In case of X-ray scattering based investigations, these structures are represented by the respective electron density distributions.

The average structure of a crystal is formed by periodic translation of a unique unit cell along all crystallographic axes. Its electron density distribution can be expresses as the convolution of the electron density distribution of a unique average unit cell, $\overline{\rho}_{cell}(\mathbf{r})$, with a Dirac comb (the convolution operator is denoted by the symbol ⊗):

$$\overline{\rho}(\mathbf{r}) = \overline{\rho}_{cell}(\mathbf{r}) \otimes \sum_n \delta(\mathbf{r} - \mathbf{R}_n) . \tag{2.1}$$

Here, $\mathbf{R}_n$ runs over all translation vectors of the average translation lattice. In a completely ordered crystal structure, there is only one unit cell configuration, and the average structure is equal to the real crystal structure. In disordered crystal structures, on the other hand,

$$\overline{\rho}_{cell}(\mathbf{r}) = \frac{1}{N} \sum \rho_{cell,n}(\mathbf{r}), \tag{2.2}$$

in which $\rho_{cell,n}(\mathbf{r})$ is the real structure unit cell at translation lattice position $\mathbf{R}_n$, and N is the total number of real structure unit cells. For an ideal infinite crystal with any degree of freedom in disorder N tends towards infinity. In $\overline{\rho}_{cell}(\mathbf{r})$, partially occupied atom sites and unphysical interatomic distances may be observed, whereas in $\rho_{cell,n}(\mathbf{r})$ only fully occupied atoms at chemically reasonable distances are possible.

The real structure is built from these real structure unit cells:

$$\rho_{real}(\mathbf{r}) = \sum_n \left(\rho_{cell_n}(\mathbf{r}) \otimes \delta(\mathbf{r} - \mathbf{R}_n) \right). \tag{2.3}$$

A difference structure between the real structure and the average structure can be calculated by

$$\begin{aligned} \Delta\rho(\mathbf{r}) = \rho_{real}(\mathbf{r}) - \overline{\rho}(\mathbf{r}) &= \sum_n \left(\rho_{cell,n}(\mathbf{r}) \otimes \delta(\mathbf{r} - \mathbf{R}_n) \right) - \overline{\rho}_{cell}(\mathbf{r}) \otimes \sum_n \delta(\mathbf{r} - \mathbf{R}_n) \\ &= \sum_n \left[\left(\rho_{cell,n}(\mathbf{r}) - \overline{\rho}_{cell}(\mathbf{r}) \right) \otimes \delta(\mathbf{r} - \mathbf{R}_n) \right] . \end{aligned} \tag{2.4}$$

Note that $\rho_{real}(\mathbf{r})$ and also $\Delta\rho(\mathbf{r})$ are not periodic.

2.1.2. Bragg scattering from ordered and average crystal structures

In kinematical scattering theory, the Fourier transform of an electron density distribution $\rho(\mathbf{r})$ yields the structure factor $F(\mathbf{h})$. In the following, FT($g(\mathbf{x})$) denotes the Fourier transform operator on a function $g(\mathbf{x})$. Thus:

$$F(\mathbf{h}) = \mathrm{FT}\big(\rho(\mathbf{r})\big) = \int \rho(\mathbf{r})\, e^{2\pi i \mathbf{hr}} d\mathbf{r}\,. \tag{2.5}$$

$\mathbf{h} = (h,k,l)$ is a reciprocal-space vector. With the assumption that the electron density distribution of a crystal structure, $\rho(\mathbf{r})$, is the sum of electron densities $\rho_j(\mathbf{r})$ of individual atoms j located at positions $\mathbf{R}_j$, *i.e.*

$$\rho(\mathbf{r}) = \sum_j \big(\rho_j(\mathbf{r}) \otimes \delta(\mathbf{r} - \mathbf{R}_j)\big), \tag{2.6}$$

one obtains by Fourier transform and by use of the convolution theorem

$$F(\mathbf{h}) = \sum_j f_j(\mathbf{h})\, e^{2\pi i \mathbf{hR}_j}\,. \tag{2.7}$$

$f_j(\mathbf{h})$ is the atomic form factor of atom j, corresponding to the Fourier transform of the atomic electron density $\rho_j(\mathbf{r})$:

$$f_j(\mathbf{h}) = \int \rho_j(\mathbf{r})\, e^{2\pi i \mathbf{hr}} d\mathbf{r}\,. \tag{2.8}$$

With eq. 2.7 the structure factor of an average structure $\overline{\rho}(\mathbf{r})$ is obtained as

$$F_{hkl}(\mathbf{h}) = \sum_j \overline{f}_j(\mathbf{h})\, e^{2\pi i \mathbf{hR}_j^0}\,. \tag{2.9}$$

Here, $\overline{f_j}$ denotes the form factor of an atom site in the average structure. By the use of the periodicity of $\overline{\rho}(\mathbf{r})$ (eq. 2.1), $F_{hkl}(\mathbf{h})$ can be alternatively expressed as

$$F_{hkl}(\mathbf{h}) = \mathrm{FT}\big(\overline{\rho}_{cell}(\mathbf{r})\big)\, \mathrm{FT}\left(\sum_n \delta(\mathbf{r} - \mathbf{R}_n)\right) = \overline{f}_{cell}(\mathbf{h}) \sum_n e^{2\pi i \mathbf{hR}_n} = \overline{f}_{cell}(\mathbf{h}) \frac{1}{\overline{V}_{cell}} \sum_u \delta(\mathbf{h} - \mathbf{H}_u)\cdot \tag{2.10}$$

Here, $\overline{f}_{cell}(\mathbf{h})$ is the form factor of the whole average cell. In analogy to real space, the sum of Dirac δ-function in the above expression represents the reciprocal lattice, including all reciprocal lattice vectors $\mathbf{H}_u$. $\overline{V}_{cell}$ is the volume of the average unit cell, and is used for normalisation.

Experimentally accessible are the scattering intensities, for which in the kinematic limit holds

$$I(\mathbf{h}) = |F(\mathbf{h})|^2 = F(\mathbf{h})F^*(\mathbf{h})\,. \tag{2.11}$$

The scattering intensities of the average structure are thus

$$\begin{aligned} I_{Bragg}(\mathbf{h}) = |F_{hkl}(\mathbf{h})|^2 &= \sum_j \sum_{j'} \overline{f}_j(\mathbf{h})\overline{f}^*_{j'}(\mathbf{h})\, e^{2\pi i \mathbf{h}(\mathbf{R}_j^0 - \mathbf{R}_{j'}^0)} \\ &= \overline{f}_{cell}(\mathbf{h})\overline{f}^*_{cell}(\mathbf{h}) \frac{1}{\overline{V}^2_{cell}} \sum_u \partial(\mathbf{h} - \mathbf{H}_u)\,. \end{aligned} \tag{2.12}$$

Accordingly, Bragg scattering intensities are constricted to sharp peaks at discrete reciprocal lattice points. Bragg scattering is a coherent summation of intensities, *i.e.* all unit cells contribute scattering intensities in an equal measure to a given reciprocal lattice point. This allows structure solution by re-assigning phase information to experimentally measured intensities by *direct methods* and inverse Fourier transform of the obtained structure factors to the electron density distribution.

2.1.3. *Diffuse scattering from disordered crystal structures*

In the following, a disordered real crystal structure is considered that allows for both, chemical and positional disorder. The actual site $\mathbf{R}_j$ of each atom j is shifted by a displacement $\mathbf{u}_j$ from its average position, *i.e.* $\mathbf{R}_j = \mathbf{R}_j^0 + \mathbf{u}_j$. The electron density of a real structure site is $\rho_{real,j}(\mathbf{r})$. Vacancies are allowed with $\rho_{real,j}(\mathbf{r}) = 0$. With $f_{real,j}(\mathbf{h}) = \mathrm{FT}(\rho_{real,j}(\mathbf{r}))$, the structure factor of the real structure, $F_{real}(\mathbf{h})$, is

$$F_{real}(\mathbf{h}) = \sum_j f_{real,j}(\mathbf{h})\, e^{2\pi i \mathbf{h}(\mathbf{R}_j^0 + \mathbf{u}_j)} . \tag{2.13}$$

Similarly, the structure factor of the difference structure, $F_\Delta(\mathbf{h})$, is the difference of eqs. 2.13 and 2.9:

$$\begin{aligned} F_\Delta(\mathbf{h}) = F_{real}(\mathbf{h}) - F_{hkl}(\mathbf{h}) &= \sum_j f_{real,j}(\mathbf{h})\, e^{2\pi i \mathbf{h}(\mathbf{R}_j^0 + \mathbf{u}_j)} - \sum_j \overline{f}_j\, e^{2\pi i \mathbf{h}\mathbf{R}_j^0} \\ &= \sum_j \left(f_{real,j}(\mathbf{h})\, e^{2\pi i \mathbf{h}\mathbf{u}_j} - \overline{f}_j \right) e^{2\pi i \mathbf{h}\mathbf{R}_j^0} . \end{aligned} \tag{2.14}$$

Finally, the scattering intensities arising from $F_\Delta(\mathbf{h})$ are according to eq. 2.11:

$$\begin{aligned} I_{diffuse}(\mathbf{h}) &= \left| F_\Delta(\mathbf{h}) \right|^2 \\ &= \sum_j \sum_{j'} \left(f_{real,j}(\mathbf{h})\, e^{2\pi i \mathbf{h}\mathbf{u}_j} - \overline{f}_j(\mathbf{h}) \right) \left(f^*_{real,j'}(\mathbf{h})\, e^{-2\pi i \mathbf{h}\mathbf{u}_{j'}} - \overline{f}^*_{j'}(\mathbf{h}) \right) e^{2\pi i \mathbf{h}(\mathbf{R}_j^0 - \mathbf{R}_{j'}^0)} . \end{aligned} \tag{2.15}$$

In a completely ordered structure, all $\mathbf{u}_j$ become zero, and $f_{real,j} = \overline{f}_j$. As a consequence $I_{diffuse}$ vanishes. Conversely, if there is a random distribution of atoms in the real structure, interference of the Fourier coefficients vanishes, and the resulting diffuse scattering intensity distribution of uncorrelated atoms is broad and featureless (corresponding to *monotonic Laue scattering*, *cf.* von Laue, 1941, p. 177). However, all intermediate steps between perfect order and random disorder will cause interference of the Fourier coefficients in eq. 2.15. The resulting structured features in the continuous diffuse scattering distribution can be unravelled by use of reciprocal space methods (for examples see section 2.3), or by PDF analysis.

Unlike $I_{Bragg}(\mathbf{h})$, $I_{diffuse}(\mathbf{h})$ is a continuous function. Scattered wavetrains originating from different parts of the disordered structure show fluctuations in scattering amplitudes and phase shifts at a given **h**, and hence they effectuate an incoherent summation of intensities, which is averaged over space and time. This prevents structure solution by *direct methods*.

However, in order to investigate disorder by means of diffuse scattering intensities, it is practically impossible to sum up intensity contributions of all atom pairs in a crystal structure as it is suggested by eq. 2.15. Therefore it is more convenient to evaluate diffuse scattering in terms of statistical relationships of the form factors and atom positions. In this regard, a general description of diffuse scattering was given, *e.g.* by Welberry & Butler (1995). Their approach is based on short-range pair correlations of individual atoms taking into account chemical and displacive disorder. The diffuse intensity is thus

$$I_{diffuse}(\mathbf{h}) = \sum_{m}\sum_{j,k} N_m c_j c_k f_j f_k^* \left[\frac{p_m^{jk}}{c_k} \left\langle e^{2\pi i \mathbf{h}\mathbf{u}_m^{jk}} \right\rangle - \left\langle e^{2\pi i \mathbf{h}\mathbf{u}^{jk}} \right\rangle \right] e^{2\pi i \mathbf{h}\mathbf{R}_m} . \tag{2.16}$$

The summation runs over all interatomic pair vectors $\mathbf{R}_m$ of the average structure. N_m is the total number of atomic pairs associated with the vector $\mathbf{R}_m$ in the structure. The indices j and k denote the atom types connected by $\mathbf{R}_m$. c_j and c_k are the concentrations of these atom types, and p_m^{jk}, is the probability that there exists an atom of species k at the end of the vector $\mathbf{R}_m + \mathbf{u}_m^{jk}$, provided that there is an atom of species j at the origin of the vector. **u** is the local deviation of the respective interatomic vector from the associated average vector $\mathbf{R}_m$. Symbols $\langle \ldots \rangle$ indicate that the exponential functions are averaged over the appropriate displacements **u**: In case of $\mathbf{u}_m^{jk}$, this average is taken only over all displacements where atom types j and k are linked by $\mathbf{R}_m$, in case of $\mathbf{u}^{jk}$, by contrast, the average is taken over *all* displacements linking two appropriate atoms. For more details see Welberry & Butler (1995).

It can be seen from eqs. 2.12 and 2.15 that scattering intensities are not dependent on the absolute positions of atoms, but only on the difference $\mathbf{R}_j^0$ - $\mathbf{R}_{j'}^0$ of atomic pairs. For that reason, Patterson (see section 2.2) and PDF methods (see below) are just able to recover interatomic distances, but no atom positions.

2.1.4. Pair Distribution Function analysis

The *Pair Distribution Function* (PDF) is a density distribution function, accumulating the probability for a pair of densities being existent at a certain distance. It can also be interpreted as an auto-correlation function. Mathematically, the PDF is obtained by inverse Fourier Transform of the real-valued frequency domain of any density distribution into the pair correlation domain. In crystallographic and other materials-related applications, the basic underlying density distribution is in case of X-ray scattering methods the electron density, in case of neutron scattering it is the nuclear scattering length, respectively. The frequency domain is represented by X-ray or neutron diffraction patterns. The underlying pair correlation domain is made up by electron density or nuclear scattering length correlations, *i.e.* by interatomic distances between electron shells or atomic nuclei. In this work, the focus is put on X-ray diffraction only, but the concepts may be easily transferred to neutron diffraction investigations.

The density of the PDF at a given distance is proportional to the multiplicity of atom pairs separated by this distance, and to the products of the scattering power of each pair. In the present work, 3D-PDF densities are computed by Fourier Transform from single crystal scattering data. With the total scattering intensities

$$I_{tot}(\mathbf{h}) = I_{Bragg}(\mathbf{h}) + I_{diffuse}(\mathbf{h}) \tag{2.17}$$

one obtains the 3D-PDF

$$P_{tot}(\mathbf{r}) = \mathrm{FT}\left(I_{tot}(\mathbf{h})\right) = \mathrm{FT}\left(\left|F_{hkl}(\mathbf{h})\right|^2\right) + \mathrm{FT}\left(\left|F_{\Delta}(\mathbf{h})\right|^2\right). \tag{2.18}$$

However, Bragg scattering intensities are generally several orders of magnitude stronger than diffuse scattering intensities (*i.e.* $|F_{hkl}(\mathbf{h})|^2 >> |F_{\Delta}(\mathbf{h})|^2$). Consequently, pair correlations of the average structure are predominant in the resulting PDF (*i.e.* $\mathrm{FT}(|F_{hkl}(\mathbf{h})|^2) >> \mathrm{FT}(|F_{\Delta}(\mathbf{h})|^2)$), hiding the underlying correlations of the local, disordered structural features. The basic idea of the presented method of ΔPDF analysis is to extract the diffuse scattering intensities from the experimental data and to compute a PDF from diffuse scattering alone. As Bragg scattering intensities are omitted, the resulting PDF exclusively comprises all pair correlations of the deviations of the real crystal structure relative to the average structure, *i.e.* it shows the differences between the real structure and the average structure. By Fourier transform of the isolated diffuse scattering intensities, one obtains the so-called 3D-ΔPDF, being

$$P_{\Delta}(\mathbf{r}) = \mathrm{FT}\left(\left|F_{\Delta}(\mathbf{h})\right|^2\right) = \mathrm{FT}\left(I_{tot}(\mathbf{h}) - \left|F_{hkl}(\mathbf{h})\right|^2\right). \tag{2.19}$$

In practice, this approach is advantageous over computing the total scattering PDF, even though additional data processing steps are necessary. In PDF space, pair correlation lengths within local, disordered motifs of the real structure are similar to those of short atomic distances within the ordered average structure, which impairs the interpretation of a total scattering 3D-PDF. In reciprocal space, on the other hand, the frequency distribution of the average structure is confined to well-defined lattice points. Hence, in most parts of reciprocal space, the difference $I_{tot}(\mathbf{h})$ - $|F_{hkl}(\mathbf{h})|^2$ can be easily calculated. Special care has only to be taken at Bragg positions (see section 5.3). For a detailed derivation, definitions, and properties of the 3D-PDF and 3D-ΔPDF see sections 3.2 and 4.2.

2.1.5. One-dimensional PDF analysis of crystalline powder samples

One-dimensional (1D) PDF analysis is widely used for structural investigation of amorphous glasses and liquids, as well as of disordered crystals. For an introduction see *e.g.* Egami & Billinge (2003), Proffen *et al.* (2003), Proffen & Kim (2009). In the last years, it has become more and more successful in analysing the real structure of nano-particles (*e.g.* Neder & Korsunskiy, 2005; Billinge, 2008). Up to date, PDF analysis of crystallographic samples is carried out on the basis of powder scattering experiments. The total scattering intensities are included, *i.e.* information about the average structure (Bragg scattering) and local disorder (diffuse scattering) is processed at the same time. In contrast to other crystallographic methods, no periodicity is implied, which favours the method for investigation of structural disorder. As the method is based on 1D scattering intensities, the resulting PDF is also 1D, *i.e.* it is a function of the norms of interatomic vectors. Angular information on these interatomic vectors, however, is not available, which limits the structural interpretation noticeably. To avoid termination errors and to resolve accurately overlapping pair correlations with similar length (but possibly different angular orientations), it is necessary to measure up to very high diffraction angles in experiments.

Some structural information can be directly extracted from powder diffraction based PDFs (for an overview see Egami & Billinge (2003)): typical bond-lengths can be measured from PDF peak positions (*e.g.* Dove *et al.*, 1997; Petkov *et al.*, 1999), the integrated intensity of PDF peaks reveals information about coordination numbers (Louca & Egami, 1999; Petkov *et al.*, 1999). PDF peak widths as a function of temperature (Billinge *et al.*, 1996), doping (Bozin *et al.*, 2000), or interatomic distances (Jeong *et al.*, 1999) are used to obtain details about the atom-pair distribution probability. More reliable information, however, is acquired by simulation and optimisation of the PDFs of structural models. The powder PDF can directly be calculated from a structural model. To fit the model PDF to experimental data, the most common method is so-called *real-space Rietveld analysis* (Proffen & Billinge, 1999). However, to avoid ambiguities in the structural data projected to 1D, detailed preliminary knowledge of the structure is required. In literature, different definitions and formalisms of 1D PDFs are used. An overview of some variants is given by Keen (2001).

By extending the PDF method to 3D space, based on 3D single crystal diffraction, the above-mentioned limitations can be bypassed. Especially by abandoning the strict concept of total scattering transformation, the presented method of ΔPDF analysis (see sections 3.2 and 4.2.2) allows a straightforward interpretation of selected aspects of structural disorder.

2.1.6. Disorder in quasicrystals

One main focus of this work is on the investigation of structural disorder in a decagonal quasicrystalline phase (see chapter 4). For a recent general introduction to quasicrystals see *e.g.* Steurer & Deloudi (2009). Quasicrystals are complex materials and most approaches done so far to solve a quasicrystal's structure just give an approximation on the real structure. Diffuse scattering is a frequent feature in diffraction patterns of quasicrystalline structures. Presence of diffuse scattering intensities is not a stringent indication of disorder in quasicrystals (Weber & Steurer, 2008), but structural disorder is often a characteristic of aperiodic crystal structures (see *e.g.* Welberry & Butler, 1995; Steurer & Frey, 1998). The same types of disorder that are known from periodic crystals are also observed in quasicrystals. Static disorder like displacive, orientational, substitutional, or rarely glass-like disorder is found, as well as dynamic disorder due to phononic excitations, which becomes manifest in the form of thermal diffuse scattering (TDS). Additional types of disorder are particular for quasicrystals, such as phasonic disorder producing phasonic diffuse scattering (PDS, which is equivalent to TDS, but the underlying displacements are along higher-dimensional directions), quasiperiodic approximant domains, or out-of-phase domains in higher dimensions. In decagonal phases, which combine of 1D periodic ordering along a unique fivefold axis and aperiodic ordering in quasiperiodic layers perpendicular thereto, the frequent presence of diffuse scattering intensities indicates respectable structural disorder (Frey & Steurer, 1993; Frey, 2000; Frey & Weidner, 2003). Even there are many publications concerning diffuse scattering of quasicrystals, quantitative investigations of diffuse scattering and structural disorder of decagonal quasicrystals has still not been accomplished in detail so far. An overview on previous research is given in sections 4.1 and 4.3.2.

Up to now, there is still an uncertainty about energetic and/or entropic stabilization of quasicrystalline structures, and the role of disorder concerning this matter is not yet investigated sufficiently. It is not proven, whether quasicrystalline structures are a ground state of matter, *i.e.* they are stable down to 0 K, or if they are entropy stabilized high-temperature phases. In the latter case, disordered domains could be a transitional state in the transformation to periodic low-temperature phases. Further, the question, if quasicrystal structures are quasiperiodic in a strict sense, or if they are just quasiperiodic on average with locally disordered domains, in not answered yet. Thus, specific knowledge about disorder in quasicrystals may be of importance in solving these problems.

2.1.7. Reciprocal space vs. PDF space methods

The majority of current single-crystal methods for studying disorder is directly based on reciprocal space (see section 2.3). Qualitative interpretation of diffuse scattering patterns allows the understanding of the underlying disorder to a certain extent, *e.g.* the dimensionality of disorder, but a more detailed analysis is often intricate. By contrast, PDF space has the same metrics as real space. As a result, PDF analysis allows a direct interpretation of structural features, such as the lengths and directions of the pair correlations and the maximum correlation length.

Fourier transforms are invertible. Hence the information content carried by diffuse scattering intensities is identical to that of their Fourier transform, *i.e.* the ΔPDF. Although the transformation into PDF space is an additional effort in data processing, modelling of disordered structures may be easier and more comprehensible by fitting within the pair correlation domain. Whereas the change of the properties of one single atomic position causes a slight modification of the whole reciprocal space intensities, in PDF space only correlation vectors associated with the changed atom are affected, resulting in a limited number of locally well-confined variations of ΔPDF densities. In human perception, changes in PDF space are easier to grasp than in reciprocal space, and qualitative interpretation of ΔPDF densities provides good starting models. Also in structural analysis and modelling by means of automated data processing and filtering, implementations in PDF space have the advantage that data can be manipulated at straightforwardly determinable coordinates. The use of intricate frequency filters becomes obsolete in reciprocal space (*cf.* section 6.4).

As it will be shown below, ΔPDF modelling permits easily to model isolated parts of the disordered local structure and fitting these to selected parts of the ΔPDF, without considering the complete crystal structure. In this way, multiple self-contained structural motifs can be modelled simultaneously with independent, overlapping PDF densities, provided that their internal pair-correlations are not too similar to be distinguished. Moreover, if specific correlation lengths are of major or minor interest respectively, pair-correlation densities can be accentuated, weakened or excluded from evaluation by the use of straightforward weighting or masking filters. Such localised and selective data handling, on the same scale as the associated structural features, makes PDF modelling of disordered structures a very powerful tool, and even partial or partially correct models will lead to interpretable results (for an example see section 4.3.5).

All data manipulation and filtering processes applied in PDF space can, of course, also be realised in reciprocal space, and vice versa. However, *e.g.* simple weighting or masking filters, which are implemented by multiplication of data values in one space, are equivalent to more intricate band-pass filters realised by convolution operations in the complementary space. Thus, for each required data manipulation it is essential in which domain, reciprocal space or PDF space, the data are treated, because the implementation and the understanding of the data manipulations will be simplified. Examples for data manipulations in reciprocal space implemented in this work are the removal of background intensities (see section 5.2) and the separation of Bragg and diffuse scattering intensities (see section 5.3) in experimental data, or the application of a detector envelope mask function on modelled data in order to simulate truncation effects when computing the PDF (see section 4.3.5). On the contrary, modelling of intra-cluster disorder by the use of an attenuation function (see section 4.3.5), or the restriction of fitness function evaluation to a maximum correlation range during model refinement (see section 4.3.6) could easier be realised in PDF space than in reciprocal space (see also section 6.4.2).

2.2. Average-Structure Solution with Patterson Methods

2.2.1. The Patterson function

Patterson methods are well-established for the solution of average structures of crystals. In particular before direct methods became widely available they were one of the most important tools in structural crystallography. Patterson methods base on the analysis of correlations between atomic pairs. They are closely related to the PDF method, with the main difference that Patterson methods base on Bragg scattering, and that they reveal information about average structures, thus.

The basis of all methods that are grouped under the term *Patterson methods* is the *Patterson function* (Patterson, 1934, 1935). Here, the Patterson function is discussed in terms of electron density distributions in X-ray scattering investigations, but it can be applied on any density distribution, *e.g.* the nuclear scattering length in neutron diffraction investigations. The Patterson function is

$$P_{hkl}(\mathbf{r}) = \rho(\mathbf{r}) \otimes \rho(-\mathbf{r}) = \int \rho(\mathbf{r_0})\,\rho(\mathbf{r_0}+\mathbf{r})\,d\mathbf{r_0}\,. \tag{2.20}$$

Alternatively, $P_{hkl}(\mathbf{r})$ can be expressed as the Fourier transform of Bragg scattering intensities:

$$P_{hkl}(\mathbf{r}) = \int \left|F_{hkl}(\mathbf{h})\right|^2 e^{2\pi i\mathbf{rh}}\,d\mathbf{h} \tag{2.21}$$

or, as $|F_{hkl}(\mathbf{h})|^2 = |F_{hkl}(-\mathbf{h})|^2$,

$$P_{hkl}(\mathbf{r}) = \int \left|F_{hkl}(\mathbf{h})\right|^2 \cos(2\pi\mathbf{rh})\,d\mathbf{h}\,. \tag{2.22}$$

P_{hkl} is a distribution function of interatomic distances. As no phase information is included, the Patterson function does not allow the determination of absolute atom positions. It only reveals the relative positions of all atomic pairs within a crystal structure. The integrated density of a Patterson peak is proportional to the product of scattering power, *i.e.* the atomic number, of the two atoms at the origin and the end of the interatomic vector **r**, and to the multiplicity of all atomic pairs separated by **r** in the whole crystal structure. $P_{hkl}(\mathbf{r})$ is always centrosymmetric, having the Laue symmetry of the crystal's unit cell combined with the Bravais lattice symmetry. There are 24 of such possible centrosymmetric space groups. The periodicity and the unit cell of $P_{hkl}(\mathbf{r})$ are the same as of the associated crystal structure. However, the peak density in a Patterson cell is much higher than in the corresponding electron density distribution: If a crystal structure consists of N atoms, there are N^2 interatomic vectors. N of these, which correlate each atom with itself, have zero length and contribute to the strong origin peak of a Patterson function. The remaining $N(N-1)$ vectors are distributed throughout Patterson space. All the same, the interpretation of Patterson functions is considerably hampered by several factors that produce a high level of overlapping peaks. First of all, the above-mentioned peak density in a Patterson map is increased by a factor N compared to $\rho(\mathbf{r})$. Further, Patterson peaks are broader than electron density peaks of atoms, because their width results from the convolution of both of the constituent electron density peaks. And, not least of all, there are often multiple similar or equal independent interatomic vectors present in a structure, generating superimposed Patterson peaks.

2.2.2. Harker lines and sections

Harker (1936) realised that the symmetry elements of a crystal structure influence the spatial distribution of Patterson peaks. Atoms located on general positions have particularly oriented interatomic vectors to equivalent positions linked by a symmetry operation. Atom pairs linked by a planar element, *i.e.* a mirror plane or a glide plane, produce Patterson peaks that are located on lines (*Harker lines*) normal to the orientation of that plane. Conversely, atom pairs linked by linear symmetry elements, *i.e.* rotation axes and screw axes, effectuate Patterson peaks that are clustered in planes (*Harker sections*) in an orientation perpendicular to these axes. By analysis of such special sections with accumulated peak density in Patterson space, the space group symmetry of a crystal structure can be identified. However, Harker analysis is limited, as atoms on special positions do not contribute to Harker lines or sections corresponding to the symmetry elements they are lying on; in contrast, there may be a notable amount of randomly coinciding, but symmetry-independent peaks in Harker sections.

2.2.3. The heavy atom method

The integrated density of a Patterson peak is proportional to the atomic number of the atom pair involved. If there is a limited number of atoms with high atomic number in a structure that consists of comparatively light atoms otherwise, the Patterson function will contain a manageable number of strong peaks due to correlations between the heavy atoms. A bigger number of intermediate peaks is due to heavy–light correlations, but most peaks are weak, due to light–light correlations. The latter can usually not be resolved in a satisfying way and merge to a background signal.

From the distribution of the strong Patterson peaks, it is oftentimes possible to guess the electron density distribution function of the partial structure made up by heavy atoms. If the position of the heavy atoms is known, also their phase contribution to $F_{hkl}(\mathbf{h})$ is known. The phases of heavy atoms dominate the total phases sufficiently in order they can be used as an approximation to these, and thus, also positions of light atoms can be roughly assigned. Based on this information, it is possible to successively refine all phases and atom positions in an iterative process.

The heavy atom method is in particular successful for centrosymmetric crystal structures, where the assignment of phases is just a decision between the two possible values 0 or π. In this case, the signs of the heavy atom phases match to a high degree the correct solution.

Structural solution techniques similar to the heavy atom method are possible, if a Patterson map contains peaks that originate from high multiplicity of a known structural unit, such as a molecule or a structural cluster (*e.g.* Nordman & Nakatsu, 1963; Burnett & Rossmann, 1971).

2.2.4. Special applications of Patterson methods

Apart from the techniques explained above, many other applications of Patterson methods were used for structure solution so far. These applications often base on problem-related assumptions, or need specific requirements to be fulfilled. Out of these variants, one particular example is specially worth mentioning, because it illustrates the parallels of Patterson analysis to the PDF approach presented in this work. Black (1955) determined the (average) structure of monoclinic $Al_{13}Fe_4$. As we know today, this compound is an approximant structure to *d*-Al–Cu–Co quasicrystals (see section 4.3.2). Black (1955) compared special 2D sections of the 3D Patterson function to show that the layered structure of $Al_{13}Fe_4$ is made up of a stacking sequence of alternating flat and internally puckered layers. These Patterson sections were chosen so that they either comprised intra-layer pair correlation vectors of flat layers, intra-layer pair correlation vectors of puckered layers, or inter-layer pair correlation vectors between adjacent flat and puckered layers. A very similar approach to Black's one was now successfully applied in PDF analysis (chapter 4). But instead of analysing the Patterson function calculated from Bragg intensities in case of the long-range ordered approximant structure, the PDF investigation was based on diffuse scattering intensities of disordered *d*-Al–Cu–Co.

2.3. Real-structure Solution Based on Single-Crystal Diffraction

Whereas PDF analysis is a well-established investigation technique for the real structure of disordered crystalline powders (see section 2.1.5), in single crystal investigations reciprocal-space based modelling techniques are commonly in use nowadays. An overview of such diffuse scattering simulation techniques is given in the following.

2.3.1. Analytical mathematical expressions

A way in which diffuse scattering may be described is by simulation of the diffraction pattern by analytical mathematical expressions. This approach allows very fast computations, as there is no need to build up large atomic structure models, as it is *e.g.* the case in Monte Carlo simulations (see below), However, it is restricted to relatively simple structures as mathematical complexity increases drastically with the complexity of the underlying problem. A recent application was presented *e.g.* by Bürgi *et al.* (2005).

2.3.2. Infinite series expansions

An alternative mathematical approach to describe diffuse scattering is the use of infinite series expansions. The basic concept is to approximate the observed diffuse scattering intensities by expansion of an expression describing the scattering intensities of a structural model. Thus, the diffuse scattering intensities are expressed as an infinite sum of terms of increasing order:

$$I_{diffuse} \approx I^{(0)} + I^{(1)} + I^{(2)} + I^{(3)} + I^{(4)} + \dots \tag{2.23}$$

Possible expansions are *e.g.* power series (Cowley, 1995, pp. 266ff), Taylor series (Butler & Welberry, 1993), or Fourier-Bessel series (Frey, 1995). A first-order expansion to a Taylor series of atomic displacements was introduced by Warren *et al.* (1951), and different extensions to higher-order series were made since then (*e.g.* Borie & Sparks, 1971; Butler & Welberry, 1993).

The more high-order terms are included in the calculation, the better the whole diffraction pattern is approached. However, the contribution of higher-order terms to the scattering intensities decreases with increasing order, whereas the complexity of the terms grows with their order, and the number of component intensities that have to be calculated increases rapidly. A detailed discussion of this aspect on Taylor series expansions is given in (Butler & Welberry, 1993; Welberry & Butler, 1994).

2.3.3. *Monte Carlo methods*

Monte Carlo models are a powerful and widely used state-of-the-art method for description of 3D real structures of single-crystals. It is based on iterative optimisation using random alterations of a model. For an overview see *e.g.* Proffen & Welberry (1998), McGreevy (2001), Welberry (2009). Structural modelling is based on the known average structure, on a qualitative interpretation of experimental diffuse intensities, or on a model representation guessed by trial-and-error. Monte Carlo models are set up as a function of random variables describing atom positions and occupancies, or orientations of bigger structural units such as clusters or molecules.

In the variant of *direct Monte Carlo* simulation, which is based on a method by Metropolis *et al.* (1953), near-neighbour interatomic or intermolecular interactions are defined to describe the energy of the model structure. After random changes of the parameters of a randomly chosen site, the total energy of the altered structure is compared to the energy of the previous state. The change of parameters is then accepted or rejected based on a probability, which is a function of the difference in energies. In this way a minimum energy conformation is searched by successive iteration. When an energetic equilibrium state is sufficiently approached, the diffraction pattern of the structure is computed and compared to the experimental data, to test whether the new model fits better to the data than the previous one. The procedure is repeated, until the model converges to an optimal configuration. Optimisation is done using either least-squares minimisation (Welberry *et al.*, 1998), or evolutionary optimisation techniques (Weber & Bürgi, 2002; Weber, 2005). Least-squares refinements have the tendency to get trapped in local minima during the iteration, *i.e.* the starting model has to be located close to the global minimum in search space. Evolutionary refinement techniques on the other hand, may start with a wide parameter range in search space and approach the global minimum successively. However, convergence may be fairly slow.

Direct Monte Carlo simulation has the advantage that propagation of near-neighbour interactions throughout the whole model structure allows setting up large models with only a few free parameters to be optimised. However, the model structure has to be sufficiently large enough to be representative for a real crystal structure. In order that statistical effects are small, and the obtained diffraction pattern does not show strong noise, Welberry *et al.* (1998) recommend to cover at least 32×32×32 unit cells. Hence Monte Carlo models typically comprise hundred thousands or millions of atom sites, and the resulting computational effort is therefore big and time-consuming. Another drawback is that the parameters used for optimisation do often not have a direct physical or crystallographic meaning. Thus, a direct structural interpretation, control of the model parameters, or a comparison to other systems is hardly possible.

Another variant, *reverse Monte Carlo* modelling (McGreevy, 2001), was first developed by McGreevy & Pusztai (1988) and was later adapted to single-crystal simulation (Nield *et al.*, 1995; Proffen & Welberry, 1997).

In reverse Monte Carlo optimisation, the procedure is basically the same as in the direct Monte Carlo method, except that the differences between observed and calculated scattering intensities after alteration of a randomly chosen atom site are directly evaluated, instead of minimizing the total energy before. The computation of the energy terms is omitted, but instead, more iterations, including extensive computations of diffuse scattering patterns, may be necessary to reach convergence, as more inappropriate model configurations will be produced. Further, because of a common over-parameterisation, reverse Monte Carlo simulations are not unique and tend to fit artefacts (Welberry & Proffen, 1998; Weber, 2005). Though the resulting modelled scattering intensities may show a good agreement to the observed ones, the structural solution may be quite likely different from the real crystal structure or even unphysical. Accordingly, reverse Monte Carlo models need often to be constrained using additional structural information.

3. Exploring Local Disorder in Single Crystals by Means of the Three-Dimensional Pair Distribution Function

3. PAPER REPRINT (I)

This chapter contains a reprint of the article:

Schaub, Ph., Weber, Th. & Steurer, W. (2007): Exploring local disorder in single crystals by means of the three-dimensional pair distribution function. *Philosophical Magazine* **87** (18-21), p. 2781-2787.

Additional results and figures to this article are presented in Appendices 3.A and 3.B.

Philosophical Magazine,
Vol. 87, Nos. 18–21, 21 June–21 July 2007, 2781–2787

Exploring local disorder in single crystals by means of the three-dimensional pair distribution function

P. SCHAUB*, T. WEBER and W. STEURER

Laboratory of Crystallography, Department of Materials, ETH Zürich,
CH-8093 Zürich, Switzerland

(*Received 30 August 2006; in final form 27 October 2006*)

Pair distribution function (PDF) analysis, based on experimental X-ray or neutron diffraction data of crystalline powders, provides an insight into structural disorder of complex materials. However, the observation of interatomic vectors is confined to their norms. Based on three-dimensional single crystal X-ray diffraction data, the methodical approach presented here is an upgrade of current PDF analysis that considers the effective spatial orientation of interatomic vectors and, thus, provides a basis for a better and direct understanding of the structural composition of complex crystalline materials. The usability of three-dimensional difference PDF analysis is exemplified by the disordered structure of *N*,*N*′,*N*″-tris-*t*-butyl-1,3,5-benzene tricarboxamide.

1. Introduction

The pair distribution function (PDF) expresses the probability of finding two atoms at a given distance. In practice, the PDF is obtained by Fourier transform of the total scattering intensities (i.e. both Bragg and diffuse scattering) of X-ray or neutron diffraction experiments.

PDF analysis of powder data is a familiar tool for the investigation of structural disorder in crystalline materials. A full overview of this technique and its applications is given by [1]. Nonetheless, the common powder PDFs are rotational projections of three-dimensional (3D) interatomic vectors onto a one-dimensional Patterson space. Accordingly, no information on the spatial orientation of interatomic vectors is considered. At the same time, distinct interatomic vectors of similar lengths but disparate directions, are superimposed in the powder PDF. The interpretation of a powder PDF is, as a consequence, not always unambiguous and often demands precise presumptions about the structure.

In the present study, a new method for the PDF analysis is introduced which is based on single crystal X-ray scattering data and, hence, eliminates the deficiencies mentioned above. Since the primary data are 3D, the computed PDF is also 3D and represents both the lengths and the angular information of interatomic vectors. Computation is performed in an analogue way to the powder PDF by Fourier transform, except that three dimensions are now considered.

---

*Corresponding author. Email: schaub@mat.ethz.ch

Philosophical Magazine
ISSN 1478–6435 print/ISSN 1478–6443 online © 2007 Taylor & Francis
http://www.tandf.co.uk/journals
DOI: 10.1080/14786430701367971

2. Three-dimensional difference PDF

Disorder in a crystal structure may be considered as a set of non-periodic deviations from a virtual average structure with a periodic lattice. Hence, the electron density $\rho(\boldsymbol{r})$ of a disordered crystal may be split up into two parts – a periodic term that corresponds to the average structure and a non-periodic term that covers all deviations of the former:

$$\rho(\boldsymbol{r}) = \bar{\rho}(\boldsymbol{r}) + \Delta\rho(\boldsymbol{r}). \tag{1}$$

By the same token, the scattering intensities $I(\boldsymbol{u})$ of an ideal infinite crystal can be expressed as a composite of two terms [2]:

$$I(\boldsymbol{u}) = |\bar{F}(\boldsymbol{u})|^2 + |\Delta F(\boldsymbol{u})|^2 \tag{2}$$

$|\bar{F}(\boldsymbol{u})|^2$ is the Bragg scattering originating from the average structure. Conversely, $|\Delta F(\boldsymbol{u})|^2$ is the diffuse scattering due to local disorder.

A PDF is generally obtained by Fourier transform (FT) of scattering intensities. With equation (2), one obtains:

$$P_{\text{tot}}(\boldsymbol{r}) = FT[I(\boldsymbol{u})] = FT\left[|\bar{F}(\boldsymbol{u})|^2\right] + FT\left[|\Delta F(\boldsymbol{u})|^2\right] = P_{hkl}(\boldsymbol{r}) + \Delta P(\boldsymbol{r}) \tag{3}$$

$P_{\text{tot}}(\boldsymbol{r})$ is called the generalized Patterson function or the total scattering PDF. Its calculation involves the whole reciprocal space. In contrast, the periodic Patterson function $P_{hkl}(\boldsymbol{r})$ is restricted to the integral reciprocal lattice vectors and represents the correlation function of the periodic average lattice. $\Delta P(\boldsymbol{r})$ is the auto-correlation function of the non-periodic component in the real crystal structure and it is exempt from all information on the periodic average lattice. Since it is defined as the difference between the total scattering PDF and the periodic Patterson function, it is referred to as the difference 3D-PDF, henceforth.

Diffuse scattering is usually several orders of magnitude weaker than Bragg scattering. As a result, the total scattering PDF will be primarily dominated by the auto-correlation of the average structure. Thus, the pair correlations of the average structure may prohibit the characterization of local disorder starting from the total scattering PDF. To bypass this problem, the method of difference PDF analysis focuses on the computation and interpretation of $\Delta P(\boldsymbol{r})$.

3. Data processing

A prerequisite for the presented method of difference 3D-PDF analysis is a single crystal dataset of high quality. It is beneficial to have a high signal-to-noise ratio on the diffuse scattering and low background noise. The recorded oscillation range should cover at least one asymmetrical unit in reciprocal space; however, a major redundancy of symmetry is favourable because it increases the signal-to-background ratio and diminishes observational errors by means of the symmetry averaging process described below. Finally, the maximum diffraction angle measured should be chosen as wide as possible because it determines the pixel resolution of the calculated PDF.

The process of obtaining the difference 3D-PDF from experimental single crystal data that fulfil the above requirements involves several successive steps: reconstruction of a volume of scattering intensities from raw data into reciprocal space coordinates, data-quality enhancement by use of 3D symmetry equivalent averaging, extraction of diffuse scattering from the total scattering intensities, and ultimately the computation of the difference 3D-PDF by Fourier transform of these diffuse intensities.

The reconstruction of the intensities in undistorted reciprocal space coordinates is carried out with appropriate crystallographic software. Depending on the orientation of the sample during the measurement and the covered oscillation range, the reconstructed volume of scattering intensities is, usually, irregularly shaped. To minimize spurious truncation effects in the Fourier transform, the volume of reciprocal space, however, should be as large and complete as possible. To accomplish this, the reconstructed volume is averaged with all its symmetrically equivalent orientations in respect of the Laue symmetry of the sample. By means of this averaging process, not only the largest possible volume is achieved, but the signal-to-noise ratio is also statistically augmented.

Thereafter, the non-periodic intensities have to be separated from those of the average structure. This removal of Bragg peaks can be achieved in different ways; a simple but effective approach, which will be detailed below, is by the use of the *punch and fill* method. This method was originally introduced by Kobas *et al.* [3] for cluster analysis of decagonal quasiperiodic crystals but, as we shall see, it is suitable for all kinds of disordered crystals that produce a clear diffuse scattering. Complementary to the filtering of Bragg scattering, subtraction of background scattering has to be performed. Realistic models must consider anisotropy and angular dependence of background intensities.

Finally, the difference 3D-PDF is computed by Fourier transform of the extracted 3D diffuse scattering intensities.

4. Example of application

The method was tested with the known structure of N,N',N''-tris-t-butyl-1,3,5-benzene tricarboxamide. This organic compound crystallizes in a hexagonal structure of space group $P6_3/m$ with the lattice parameters $a = 14.100\,\text{Å}$ and $c = 6.930\,\text{Å}$ [4]. The molecules are stacked in well-ordered homochiral columns along the c-axis. These stacks exist in two different helical hands – so called ‘up’ and ‘down’ –, which laterally prefer an ‘up-down’ neighbouring. This local preference shows, however, no long-range order [4].

This compound was chosen as it shows very clear diffuse scattering. Due to the structure being well-ordered along the c-axis, the diffuse scattering is localized in discrete and narrow layers perpendicular to the l-axis at integral values of l. Within these layers, the diffuse scattering is arranged in hexagonal honeycomb-like patterns. The Bragg peaks lie in the centre of the combs and barely overlap with the diffuse scattering (see figure 1). The single crystal data were measured at the

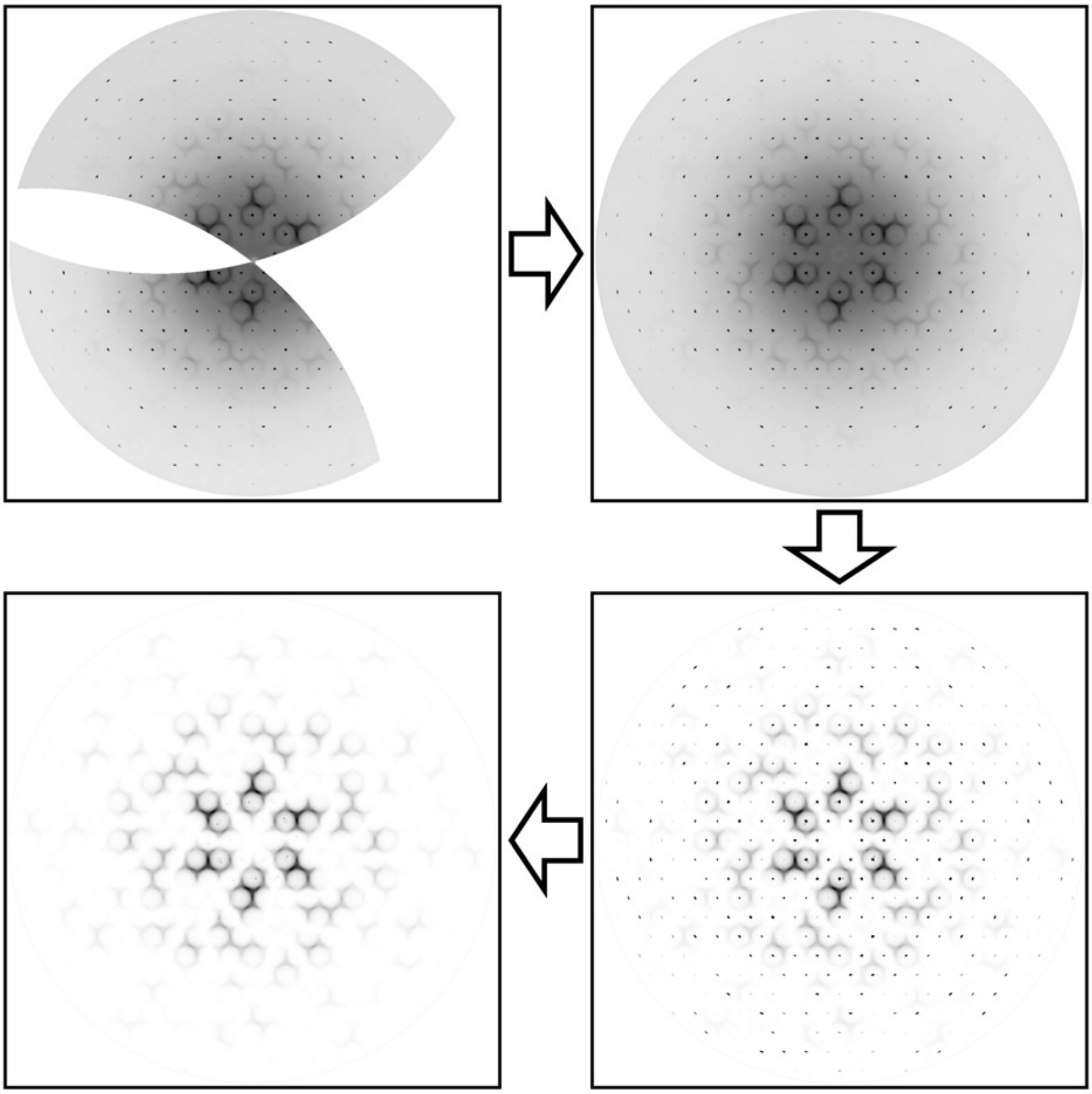

Figure 1. Steps of data processing applied to the diffraction pattern of the *hk*1-layer of *N*,*N*′,*N*″-tris-*t*-butyl-1,3,5-benzene tricarboxamide. From top left, in clockwise order: as reconstructed from the raw data, after symmetry averaging, after subtraction of background intensities, and after applying the *punch and fill* filter. The edges of each box cover a range of ±0.91 Å^{-1}.

Swiss–Norwegian beamline at the ESRF synchrotron source in Grenoble (France), using a *Mar* image plate detector.

The reconstruction of reciprocal space coordinates was performed with *Xcavate* software [5]. As the scattering intensities are sparse in reciprocal space and limited to layers with integral *l*-coordinates, only 13 *hk*-layers with $l = -6, \ldots, 6$ were reconstructed. The *hk*0-layer had the widest extent of available data with a maximum radius of $2\sin\theta/\lambda = 0.91$ Å^{-1}. All the reconstructed layers were stacked into a three-dimensional array of $1215 \times 1215 \times 13$ voxels. Such volumes were reconstructed for all 12 symmetry equivalent orientations corresponding to the Laue group $6/m$ and, finally, these data were taken together and averaged. From this volume of averaged intensities, a volume of background intensities was subtracted. Based on the assumption that background noise does not change significantly with small changes in position, the background volume was obtained by symmetry equivalent averaging of slices of reciprocal space that lay slightly above and below the layers containing the scattering intensities.

After background removal, the diffuse scattering intensities were isolated with the *punch and fill* method. As $|\bar{F}(\boldsymbol{u})|^2$ is a sum of Dirac δ-functions, it shows, in the case of an ideal experiment, point-like non-zero values only for reciprocal position vectors $\boldsymbol{u}$ with integral coordinate triplets. These Bragg peaks are broadened in the experimental dataset of real crystals owing to convolution with a resolution function, but they still remain restricted to comparatively small volumes of reciprocal space. Thus, for most of the reciprocal space, the assumption $|\Delta F(\boldsymbol{u})|^2 = I(\boldsymbol{u})$ is valid (irrespective of the underlying static background noise) and these scattering data persist, unaffected by the *punch and fill* method. On the other hand, at the position of each observed Bragg peak, a volume of data voxels is cleared ('punch'). Not only are Bragg intensities culled thereby but also part of the diffuse scattering intensities. These intensities have to be reestablished from the surroundings of the eliminated volume ('fill'). In the present example, fixed spherical volumes with radius 0.01 Å were punched out. Thereafter, they were refilled with an average value computed from their surroundings (see figure 1). To obtain the difference 3D-PDF, the remaining data volume was finally Fourier transformed by the use of the Fast Fourier transform algorithm of the *FFTW3* libraries [6]. This yielded a real space volume with an edge length of 667 Å in the *x*- and *y*-direction and 6.93 Å in the *z*-direction.

To test the effect of filtering Bragg intensities in 3D-PDF analysis, a total scattering 3D-PDF including Bragg and diffuse scattering was calculated simultaneously.

5. Discussion

It is beyond the purpose of this publication to discuss the described data processing and the quality of the data obtained. This will be the subject in a forthcoming paper. In the following, an overview is given on some illustrative aspects of the interpretation of the difference 3D-PDF of *N*,*N*′,*N*″-tris-*t*-butyl-1,3,5-benzene tricarboxamide.

When the difference 3D-PDF of our test sample is compared to the total scattering 3D-PDF, it is obvious that the information contained in the difference PDF can barely be seen in the total scattering PDF because the auto-correlation of the average structure is predominant over all the space (see figure 2).

The difference 3D-PDF describes the frequency distribution of interatomic vectors in the real structure in relation to the average structure. The origin of the distribution function lies in the centre of the data volume, with all position vectors spanning relative to it. Positive values indicate interatomic vectors that occur more frequently than in the average structure; negative values, on the other hand, indicate a lowered frequency. Although the data are 3D, the focus in this discussion is limited to a two-dimensional slice, normal to the *c*-axis and going through the origin. This special layer comprises information on interatomic vectors with a vertical component $|\Delta c| < 0.267$ Å, i.e. all horizontal and sub-horizontal interatomic vectors

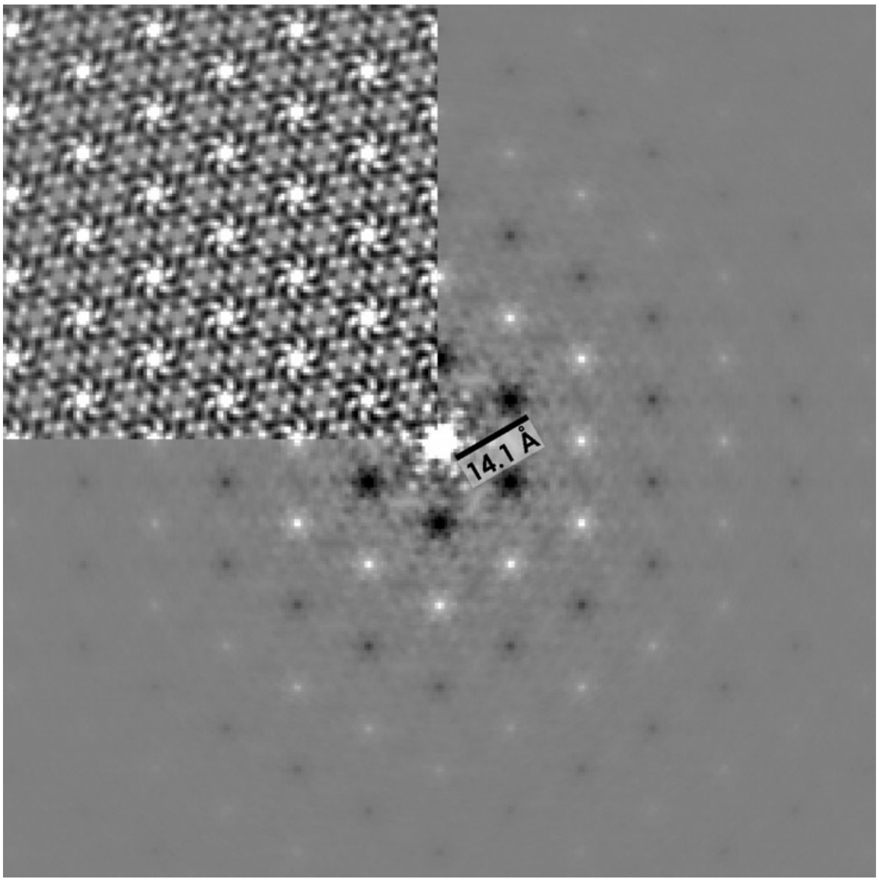

Figure 2. Two-dimensional, horizontal slice at $c = 0$ of the difference 3D-PDF of N,N',N''-tris-t-butyl-1,3,5-benzene tricarboxamide. The superimposed pattern in the upper left corner is the accordant total scattering PDF. Negative values are mapped in black colour; positive ones in white. *Note*: strong negative values in the total scattering arise from the missing $F(000)$ reflection in the source data.

of the given structure. It contains hexagonal patterns around the origin, alternating with negative and positive values with increasing radial distance (see figure 2). The main peaks, having radial distances of integer multiples of ~14 Å, lie on the vertices of a lattice, which matches the hexagonal lattice of the average structure. Consequently, these main peaks originate from the translation vectors in the *a*-direction, whereas the less distinct satellite peaks can be assigned to inter- or intramolecular vectors.

The alternating change of positive and negative correlation with radial distance reveals that there must be a systematic preference of the neighbouring molecules that differs from the average structure. Actually, it is a lateral preference to heterochiral pairs of molecules – compared to the average structure, the probability of finding homochiral pairs is lower for the direct neighbours (negative PDF peaks) and higher for the second-order neighbours (positive PDF values), etc. The continuous radial falloff of the absolute values of the peaks indicates the short-range correlation of disorder.

Note that this information on the real structure can even be obtained without knowledge of the average structure.

6. Conclusion

Difference 3D-PDF analysis is a useful tool for investigating disorder in crystalline materials available as single crystals. The application potential is shown in a simple example. With this new method, local disorder can be described considering spatial direction, i.e. interatomic vectors can be resolved via their angular orientation. In the given example with substitutional disorder only, a standard synchrotron X-ray scattering dataset was sufficient to provide results of satisfactory quality. Displacive disorder, however, would imply higher experimental resolution. Nevertheless, difference 3D-PDF analysis makes large demands on data processing, in particular, the huge amount of data to be handled. Background subtraction and removal of Bragg reflections by means of the *punch and fill* method could be realized with comparatively simple techniques in the example studied because diffuse scattering was restricted to narrow single layers and the Bragg reflections just marginally overlapped with the diffuse scattering. For more intricate systems, of course, more advanced approaches in data processing are needed. Likewise, our understanding of the 3D-PDF needs to be improved and adequate techniques developed for the realization of complete models of disorder based on the 3D-PDF.

Acknowledgements

This work is supported by the Swiss National Science Foundation (200020-105158).

References

[1] T. Egami and S.J.L. Billinge, *Underneath the Bragg Peaks: Structural Analysis of Complex Materials* (Pergamon, New York, 2003).
[2] J.M. Cowley, *Diffraction Physics*, 3rd revised ed. (Elsevier, Amsterdam, 1995).
[3] M. Kobas, T. Weber and W. Steurer, Phys. Rev. B **71** 224205 (2005).
[4] M. Kristiansen, P. Smith, H. Chanzy, *et al.*, J. Am. Chem. Soc. (2007) submitted.
[5] M.A. Estermann and W. Steurer, Phase Transit. **67** 1 (1998).
[6] M. Frigo and S.G. Johnson, Proc. IEEE **93** 2 (2005).

Appendix 3.A: Addendum to bibliography

The definitive, correct bibliographical record for reference [4] in the reference section above is:

[4] M. Kristiansen, P. Smith, H. Chanzy, *et al.*, Crystal Growth & Design **9** 6 (2009).

Appendix 3.B: Supplementary 3D-ΔPDF data

Fig. 3.3 shows the complete 3D-ΔPDF of *N,N',N''*-tris-*t*-butyl-1,3,5-benzene tricarboxamide including, supplementary to Fig. 3.2, also correlation vectors with a component along **c** direction other than ~0.000 Å. In all ΔPDF-layers, the correlations between columnar molecules are reflected in the arrangement of the main peaks on a hexagonal lattice. The ΔPDF-layer comprising vectors with a vertical component of ~3.41 Å ≈ $c/2$ contains densities similar to those at ~0.000 Å, tough the signs are inverted. This indicates that the 'up' and 'down' hand of the molecules are shifted by $c/2$ along **c** relative to each other. Minor satellite peaks are due to intra-molecular correlations and to inter-molecular correlations that are, owing to the connection of different parts of the molecular columns, slightly shorter or longer than the lattice vectors.

From Fig. 3.4 the maximum correlation length (for a definition see section 4.2.2) perpendicular to **c** can be estimated to be approximately 150 Å. This length corresponds to a range of about 10 neighbouring shells of molecules.

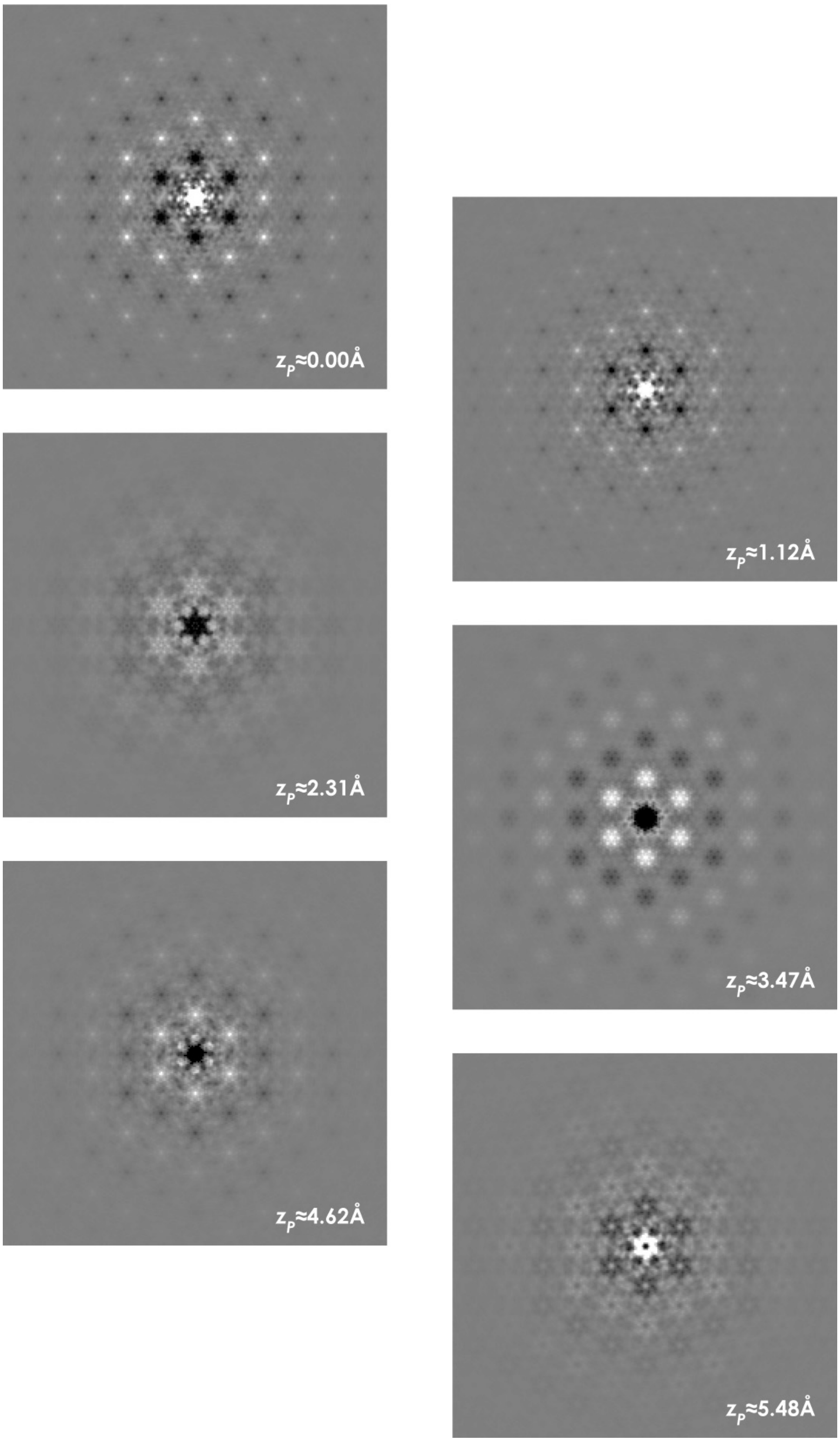

Figure 3.3: Two-dimensional (x_P, y_P)-sections at different z_P of the 3D-ΔPDF of *N,N′,N″*-tris-*t*-butyl-1,3,5-benzene tricarboxamide, computed from single crystal X-ray diffuse scattering (extracted from total scattering intensities via a *"punch-and-fill"* filter). Positive pair correlations are in white colour, negative ones in black. The centre of the sections is at $x_P = y_P = 0$. The images cover ±68.6 Å along each axis. (For a definition of the coordinate system (x_P, y_P, z_P) see section 4.3.3.

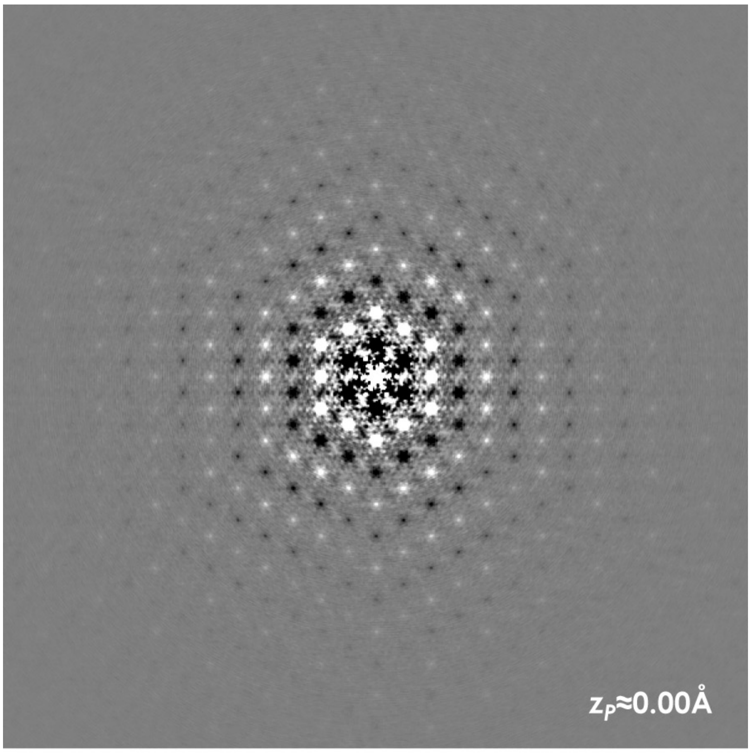

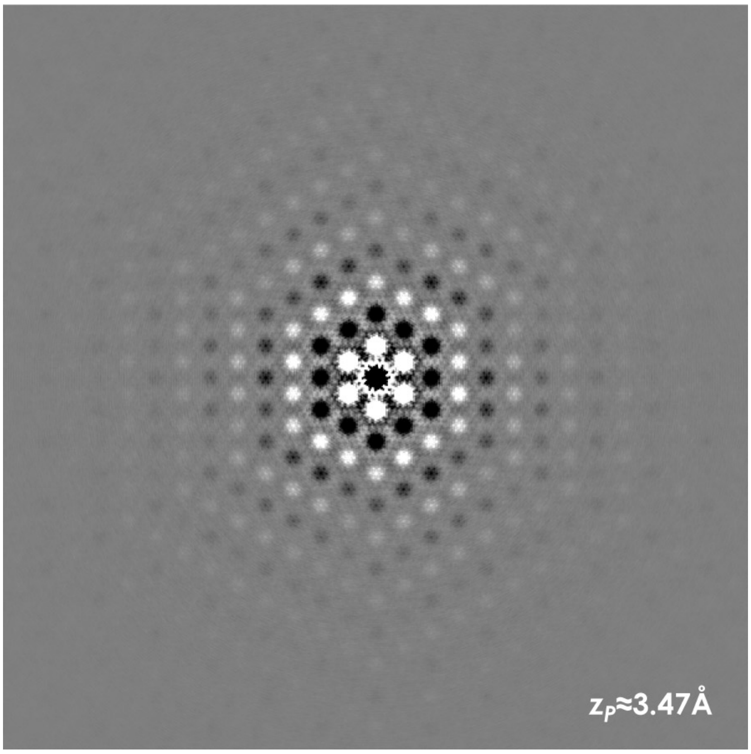

Figure 3.4: Larger two-dimensional sections of the 3D-ΔPDF of *N,N',N''*-tris-*t*-butyl-1,3,5-benzene tricarboxamide (*cf.* Fig. 3.3), showing inter-molecular neighbouring correlations up to about 10th order. The images cover ±164.7 Å along each axis. In order to visualise weak medium-range pair correlations, the colour contrast was amplified compared to Fig. 3.3.

4. Analysis and Modelling of Structural Disorder by the Use of the Three-Dimensional Pair Distribution Function Method Exemplified by the Disordered Twofold Superstructure of Decagonal Al–Cu–Co

4. PAPER REPRINT (II)

This chapter contains a reprint of the article:

Schaub, Ph., Weber, Th. & Steurer, W. (2011): Analysis and modelling of structural disorder by the use of the three-dimensional pair distribution function method exemplified by the disordered twofold superstructure of decagonal Al–Cu–Co. *Journal of Applied Crystallography* **44** (1), in press.

Additional results and figures to this article are presented in Appendices 4.A and 4.B.

Journal of
Applied Crystallography
ISSN 0021-8898

Received 11 August 2010
Accepted 2 November 2010

© 2011 International Union of Crystallography
Printed in Singapore – all rights reserved

Analysis and modelling of structural disorder by the use of the three-dimensional pair distribution function method exemplified by the disordered twofold superstructure of decagonal Al–Cu–Co

Philippe Schaub,* Thomas Weber and Walter Steurer

Laboratory of Crystallography, ETH Zürich, CH-8093 Zürich, Switzerland. Correspondence e-mail: schaub@mat.ethz.ch

Theoretical concepts and the practical application of the three-dimensional pair distribution function (3D-PDF) method and its variant, the three-dimensional Δ-pair distribution function (3D-ΔPDF) method, are presented. In analogy to traditional Patterson function analysis, advantage is taken of the Fourier transformation either of the full three-dimensional diffraction pattern of a disordered crystal or just of the isolated diffuse scattering, respectively. By the use of three-dimensional information, analysis of disorder becomes straightforward, and it becomes possible to investigate far more complicated structures than is feasible with well established powder diffraction-based PDF analysis. Compared to more traditional modelling techniques, such as Monte Carlo simulation, the 3D-ΔPDF provides direct access to disorder models and allows selective modelling of distinct structural features, which are, in contrast to reciprocal space, well localized in PDF space. The principles of the 3D-ΔPDF approach are exemplified using an analysis of the twofold ($\sim$8 Å) periodic superstructure of a decagonal $Al_{65}Cu_{20}Co_{15}$ quasicrystal. Although analysis of disorder in quasicrystals is far more demanding than in the case of periodic structures, details of the disordered structure could be elucidated. The superstructure is found to be built from columnar units, having a maximum diameter of $\sim$14.5 Å. The lateral correlation between these columns is weak. Internally, the columns consist of a long-range-ordered alternation of flat and puckered layers. The development of the model and the atomic structure of the columns are described in detail.

1. Introduction

Crystals are defined as long-range-ordered objects, which are uniformly built up from unit cells, each identical to one another. Real crystals, however, do not fulfil the concept of strict infinite translation symmetry, but they show a variety of deviations like disorder and defects. For an introduction to structural disorder and the associated diffuse scattering see *e.g.* Welberry & Butler (1995), Frey (2003) and Welberry (2004). Astonishingly, there are only a few methods for analysis and modelling of structural disorder. In recent years, simulation-based methods such as Monte Carlo modelling have become popular for analysing disorder. They aim to build real-structure computer models containing hundreds of thousands or even millions of atoms, which are supposed to be representative of the macroscopic crystal. Such simulations are powerful tools, since they allow modelling of even complex materials. However, the size of the simulated systems and the complexity of the models require very time-consuming computations. The relation between the Monte Carlo model parameters and the resulting diffuse scattering is complicated; thus establishing a satisfying model often involves numerous trial-and-error cycles. Alternatively, diffuse scattering may be described by analytical mathematical expressions. This approach allows very fast computations; however, it is restricted to relatively simple problems as mathematical complexity increases drastically with the complexity of the underlying problem (see *e.g.* Bürgi *et al.*, 2005). The three-dimensional pair distribution function (PDF) method presented in this paper is intended to fill the gap between the aforementioned approaches: it is easy to use, it is able to analyse even complex structures, and computations are fairly fast.

Currently, the PDF method is widely used for total scattering analysis of the real structures of amorphous glasses, liquids and disordered crystals. For an overview see *e.g.* Egami & Billinge (2003), Proffen *et al.* (2003) and Proffen & Kim (2009). In recent years, it has become more and more successful in analysing the real structures of nanoparticles (*e.g.* Neder & Korsunskiy, 2005; Billinge, 2008). To date, PDF

doi:10.1107/S0021889810044742

analysis of crystallographic samples has been carried out on the basis of powder scattering experiments. In contrast to other crystallographic methods, periodicity is not explicitly required for analysing a structure, which favours the method for investigation of structural disorder. The powder PDF describes the probability of pairs of scattering densities, like electron densities in the case of X-rays or nuclear scattering lengths for neutrons,[1] being existent at a certain distance. It is obtained from the Fourier transform of the experimental powder diffraction data and can be understood as a three-dimensional to one-dimensional angular projection of the auto-correlation function of the real crystal. Although the projection may lead to severe overlaps of density peaks, information about real interatomic distances is preserved, while information about the direction of interatomic vectors is lost. Both overlapping of densities and loss of angular information limit the structural interpretation noticeably, particularly in the case of complex systems. To facilitate the resolution of overlapping pair correlation maxima with similar lengths, but possibly different angular orientations, powder PDF analysis requires measurements up to very high diffraction angles. Moreover, *a priori* knowledge about the structure is often required to avoid ambiguities. These limitations become less severe when extending the PDF method to three dimensions (Schaub *et al.*, 2007). So far, the three-dimensional PDF (3D-PDF) method has been considered to be hardly practicable (He *et al.*, 1993; Egami & Billinge, 2003, p. 78), because of the huge amount of continuous three-dimensional scattering intensity data to be collected and processed. However, with the availability of fast computers and modern experimental equipment, such as fast and sensitive area detectors, characterization of disordered crystals by means of the 3D-PDF has become feasible.

In this paper, the application of the 3D-PDF approach to a disordered decagonal Al–Cu–Co (*d*-Al–Cu–Co) quasicrystal will be demonstrated. Quasicrystals are complex aperiodic materials, which require a higher-dimensional (*n*D, with $n > 3$) description to allow a periodic embedding of the structure. For a recent introduction to quasicrystals, see *e.g.* Steurer & Deloudi (2009). Diffuse scattering is a common feature in diffraction patterns of quasicrystals. Quasicrystals may show the same types of disorder as periodic crystals (for an overview see *e.g.* Steurer & Frey, 1998): static structural disorder phenomena, such as displacive, orientational, substitutional or rarely glass-like disorder, are observed, as well as dynamic disorder due to phononic excitations, which becomes manifest in the form of thermal diffuse scattering (TDS). Other types of disorder are specific to quasicrystals, such as phasonic disorder producing phasonic diffuse scattering (PDS, which is equivalent to TDS, but underlying displacements are along higher-dimensional directions), quasiperiodic arrangements of approximant domains or out-of-phase domains in higher dimensions. Decagonal phases combine one-dimensional periodic ordering along a tenfold axis and quasiperiodic ordering perpendicular thereto. Although there are many publications concerning diffuse scattering from quasicrystals, quantitative investigations of disorder in quasicrystals are mainly restricted to phononic and phasonic disorder described in the framework of hydrodynamic theory (*e.g.* De Boissieu, 2008). Examples for investigation of structural disorder on an atomic level are rare. Frey *et al.* (2000) presented a model for twofold (~8 Å) superordering in decagonal Al–Ni–Co. Weber *et al.* (2007) discussed possibilities of three-dimensional and *n*D modelling concepts. Kobas *et al.* (2004, 2005*b*) modelled disorder related to TDS and PDS in Patterson space based on diffuse scattering in Bragg layers for *d*-Al–Ni–Co. There are several reasons for the investigation of disorder in quasicrystals being far more demanding than that in periodic structures. Firstly, the average structure of quasicrystals is usually not known to the accuracy that is nowadays standard for periodic structures. Furthermore, the three-dimensional representation of the average structure typically does not show quasiperiodic repetitions of exactly the same disordered motif. Although three-dimensional structures of quasicrystals are usually built from a limited number of prototypic tiles or clusters, motifs found in the three-dimensional average structures often show a broad variety even of *average* representations of structural units throughout three-dimensional space. Note that the presence of such variants does not necessarily reflect disorder but may be a consequence of the underlying concept of strict quasiperiodicity. This lack of well defined average disordered motifs complicates the use of constraints in the determination of the real structure.

One-dimensional PDF analyses of powder samples have been carried out for decagonal (Dubois & Janot, 1988) and icosahedral (Hu *et al.*, 1992; Brühne *et al.*, 2003, 2004, 2006; Brühne, Uhrig, Gross *et al.*, 2005; Brühne, Uhrig, Luther *et al.*, 2005) quasicrystalline phases. The complexity of the structures requires good *a priori* knowledge of the real structure when using powder PDF methods. He *et al.* (1993) presented a two-dimensional PDF study on a *d*-Al–Cu–Co single crystal. In essence, the PDF information is one-dimensional, but by calculating the PDF from two-dimensional diffraction layers, they gained an additional degree of freedom in the spatial interpretation of the PDF.

So far it is still unknown whether quasicrystals are stabilized by energy or entropy. In the latter case, they would transform to periodic approximant structures when approaching 0 K, otherwise quasicrystals would be a ground state of matter. Unfortunately, the slow kinetics of metallic structures at low temperatures does not allow an easy experimental answer to this question, and *ab initio* structure simulations suffer under the lack of periodic boundary conditions. Investigation of disorder in quasicrystals is therefore one of the few techniques that allow a better understanding of the role of entropy for stabilization of quasicrystals.

In §2, theoretical and practical aspects of 3D-PDF modelling methods will be outlined. In §3, the application of 3D-PDF methods will be demonstrated using the example of the disordered ~8 Å superstructure in decagonal $Al_{65}Cu_{20}Co_{15}$. §4 will summarize the results.

---

[1] Throughout this paper, the focus will be on X-ray diffraction, but the concepts may be adapted straightforwardly to neutron diffraction applications.

2. Pair distribution function analysis in three-dimensional space

2.1. Diffuse scattering and the 3D-PDF method

The electron density distribution $\rho(\mathbf{r})$ of any disordered crystal that has an average structure can be expressed by the term

$$\rho(\mathbf{r}) = \overline{\rho}(\mathbf{r}) + \Delta\rho(\mathbf{r}), \tag{1}$$

where $\overline{\rho}(\mathbf{r})$ is the periodic electron density distribution of the average structure and $\Delta\rho(\mathbf{r})$ is the difference electron density distribution, which comprises all local deviations of the real crystal structure relative to $\overline{\rho}(\mathbf{r})$. $\Delta\rho(\mathbf{r})$ is a nonperiodic infinite function describing the local difference electron density for the whole crystal structure. Similarly, within the scope of kinematic scattering theory, the structure factor $F(\mathbf{h})$ of a disordered crystal may also be split into two components:

$$\begin{aligned} F(\mathbf{h}) &= \mathrm{FT}[\rho(\mathbf{r})] = \mathrm{FT}[\overline{\rho}(\mathbf{r})] + \mathrm{FT}[\Delta\rho(\mathbf{r})] \\ &= F_{hkl}(\mathbf{h}) + F_{\Delta}(\mathbf{h}) \end{aligned} \tag{2}$$

where $\mathrm{FT}[f(\mathbf{x})]$ denotes the Fourier transform of a function $f(\mathbf{x})$ and $\mathbf{h}$ is a vector in reciprocal space.

The total diffraction intensity distribution is given by

$$I_{\mathrm{tot}}(\mathbf{h}) = F(\mathbf{h})\,F^{*}(\mathbf{h}) = \left|F_{hkl}(\mathbf{h})\right|^{2} + \left|F_{\Delta}(\mathbf{h})\right|^{2}. \tag{3}$$

$|F_{hkl}(\mathbf{h})|^2$ is the Bragg scattering, and $|F_{\Delta}(\mathbf{h})|^2$ is the diffuse scattering intensity. Diffuse and Bragg scattering sum up incoherently, *i.e.* the cross terms $F_{hkl}(\mathbf{h})F^{*}_{\Delta}(\mathbf{h})$ and $F^{*}_{hkl}(\mathbf{h})F_{\Delta}(\mathbf{h})$ are zero (Cowley, 1995, p. 148). Bragg scattering intensities are sparsely distributed into sharp peaks at reciprocal lattice points with integral coordinates *hkl*. For an infinitely sized ideal (but possibly disordered) crystal, they are shaped as Dirac δ functions. On the other hand, diffuse scattering intensities are continuously distributed throughout reciprocal space.

Fourier transformation of the scattering intensities yields the total scattering PDF:

$$\begin{aligned} P_{\mathrm{tot}}(\mathbf{r}) &= \mathrm{FT}\big[I_{\mathrm{tot}}(\mathbf{h})\big] = \mathrm{FT}\Big[\left|F_{hkl}(\mathbf{h})\right|^{2}\Big] + \mathrm{FT}\Big[\left|F_{\Delta}(\mathbf{h})\right|^{2}\Big] \\ &= P_{hkl}(\mathbf{r}) + P_{\Delta}(\mathbf{r}), \end{aligned} \tag{4}$$

with $P_{hkl}(\mathbf{r}) = \overline{\rho}(\mathbf{r}) \otimes \overline{\rho}(-\mathbf{r})$ and $P_{\Delta}(\mathbf{r}) = \Delta\rho(\mathbf{r}) \otimes \Delta\rho(-\mathbf{r})$ ($\otimes$ denotes the convolution operator). P_{tot} can be interpreted as the auto-correlation function of the real electron density distribution of a crystal. P_{hkl} is the classical crystallographic Patterson function. When used in three-dimensional vector space, we call P_{tot} the total scattering three-dimensional pair distribution function (total scattering 3D-PDF), and P_{Δ} the 3D-ΔPDF (Schaub *et al.*, 2007).

2.2. The 3D-ΔPDF approach

Single-crystal diffraction often allows a clear separation of Bragg and diffuse scattering, which permits us to benefit from the properties of the 3D-ΔPDF described in the following.

From equation (4) one obtains

$$\begin{aligned} P_{\Delta}(\mathbf{r}) &= P_{\mathrm{tot}}(\mathbf{r}) - P_{hkl}(\mathbf{r}) = \mathrm{FT}\Big[I_{\mathrm{tot}}(\mathbf{h}) - \left|F_{hkl}(\mathbf{h})\right|^{2}\Big] \\ &= \mathrm{FT}\Big[\left|F_{\Delta}(\mathbf{h})\right|^{2}\Big]. \end{aligned} \tag{5}$$

Note that $P_{hkl}(\mathbf{r})$ and $P_{\Delta}(\mathbf{r})$ are not as easily separable as the corresponding diffraction intensities often are, *i.e.* the long-range-ordered and the disordered contributions to the PDF fully overlap. It is therefore most practicable to compute $P_{\Delta}(\mathbf{r})$ by isolating the diffuse diffraction intensities first, and subsequently Fourier transforming them.

An important fact that favours ΔPDF methods over total scattering PDF approaches is that Bragg intensities are often several orders of magnitude stronger than diffuse scattering intensities. Consequently, pair correlations of P_{hkl} are predominant in the resulting total scattering PDF. Systematic and statistical errors caused by Bragg scattering may easily amount to a magnitude comparable to the total diffuse scattering intensities, and thus artefacts from Bragg intensities will significantly bias information about disorder. By removing Bragg intensities before Fourier transformation, artefacts originating from Bragg scattering are avoided in the PDF, and at the same time, information about disorder becomes accessible with higher reliability. In many cases, like in the study presented in §3, separation is straightforward, because Bragg and diffuse scattering hardly overlap. In more intricate situations the 'punch-and-fill' approach (Kobas *et al.*, 2005*a*) may be used.

3D-ΔPDF densities are proportional to the frequency of the corresponding interatomic vectors in the real disordered structure relative to the average structure. Hence, they allow a direct qualitative interpretation of disorder. Positive values show that the corresponding vectors occur more frequently than in the average structure (positive correlation); negative ones indicate a lowered frequency (negative correlation). In the case of zero densities, average and real-structure correlations are the same, *i.e.* the corresponding pairs of electron densities are uncorrelated. As a consequence of $\Delta\rho(\mathbf{r})$ not being periodic, all ΔPDF densities beyond a finite distance $|\mathbf{r}_{\max}|$ must be zero. Hereinafter, $|\mathbf{r}_{\max}|$ will be called the correlation length of the disorder. In PDF space, the investigated volume can therefore be limited to $\pm|\mathbf{r}_{\max}|$, *i.e.* the ΔPDF volume to be examined is finite. Additionally in reciprocal space, the pixel size of the measured diffuse scattering can be limited so as not to be considerably less than $|\mathbf{r}_{\max}|^{-1}$.

2.3. Impact of the experimental limitations

When average structures are investigated, Bragg scattering intensities are integrated at the stage of data reduction over the reciprocal space volume covered by the respective peak. If done properly, the reciprocal-space resolution function has therefore no influence on the structure obtained. In the case of diffuse scattering, however, resolution-function effects cannot be corrected easily. Sharp diffuse streaks or layers may be integrated along the long-range-ordered direction(s) to partly eliminate resolution effects. On the other hand, along the disordered dimensions, the resolution function still affects the data and corresponding errors propagate into PDF space. Features that are diffuse along all directions cannot be integrated, and thus resolution errors fully propagate to PDF space. Since the resolution function may vary in reciprocal space, a simple deconvolution procedure cannot be applied to correct for resolution effects. The influence of the experimental resolution function $r_s(\mathbf{h})$ on PDF maps may be estimated roughly (Weber & Steurer, 2009; for similar discussions about experimental limitations in powder PDF refinements see *e.g.* Toby & Egami, 1992; Qiu *et al.*, 2004). For the sake of simplicity, it is assumed that the properties of $r_s(\mathbf{h})$ are constant. The observed diffraction pattern $I_{\rm obs}(\mathbf{h})$ may then be described as

$$I_{\rm obs}(\mathbf{h}) = I(\mathbf{h}) \otimes r_s(\mathbf{h}), \tag{6}$$

where $I(\mathbf{h})$ denotes the scattering intensity expected from an ideal experiment. By applying the convolution theorem one obtains in PDF space

$$P_{\rm obs}(\mathbf{r}) = P(\mathbf{r})\, R_s(\mathbf{r}). \tag{7}$$

$R_s(\mathbf{r})$ is the Fourier transform of $r_s(\mathbf{h})$. The resolution function can be directly gauged from the experimental profiles of the Bragg peaks. If $r_s(\mathbf{h})$ is assumed to be an isotropic Gaussian, it can be written as

$$r_s(|\mathbf{h}|) = \exp(-b^2|\mathbf{h}|^2). \tag{8}$$

The full width at half-maximum (FWHM) of $r_s(|\mathbf{h}|)$ is given by

$$w_r = (2/b)(\ln 2)^{1/2}. \tag{9}$$

$R_s(|\mathbf{r}|)$ is also a Gaussian:

$$\begin{aligned} R_s(|\mathbf{r}|) &= {\rm FT}\big[r_s(|\mathbf{h}|)\big] = (\pi^{1/2}/b)\exp(-\pi^2|\mathbf{r}|^2/b^2) \\ &= \left(\frac{\pi w_r^2}{4\ln 2}\right)^{1/2} \exp\left(\frac{-\pi^2|\mathbf{r}|^2 w_r^2}{4\ln 2}\right) \end{aligned} \tag{10}$$

with a FWHM

$$W_r = \frac{4\ln 2}{\pi w_r}. \tag{11}$$

This means that PDF densities become more and more attenuated with increasing distance from the origin. In a typical experimental setup with area detectors, w_r is of the order of 10^{-3}–10^{-2} Å^{-1}. Consequently, W_r is of the order of 10^2–10^3 Å. The effect of $R_s(\mathbf{r})$ on the decay of $P_{\rm obs}(\mathbf{r})$ is accordingly small for short-range correlations, but may become significant for medium-scale correlations.

Additionally, the finite size of the experimentally accessible reciprocal space influences the observed diffraction pattern and thus the real-space resolution, *i.e.*

$$I_{\rm obs}(\mathbf{h}) = \big[I(\mathbf{h}) \otimes r_s(\mathbf{h})\big]\, d(\mathbf{h}) \tag{12}$$

and

$$P_{\rm obs}(\mathbf{r}) = \big[P(\mathbf{r})\, R_s(\mathbf{r})\big] \otimes D(\mathbf{r}). \tag{13}$$

$d(\boldsymbol{h})$ describes the reciprocal-space volume covered by measurement [$d(\mathbf{h})$ = 1 for measured reciprocal-space areas, $d(\mathbf{h})$ = 0 elsewhere], and $D(\mathbf{r})$ is its Fourier transform. If one assumes that the radius $d^*_{\max}$ of the volume covered by $d(\mathbf{h})$ is of the order of a few Å^{-1}, then $D(\mathbf{r})$ will cause truncation ripples in close proximity to intense PDF peaks. This effect may be reduced by measurements including very high diffraction angles, which is, in comparison, far more difficult for single crystals than it is in the case of powder samples. On the other hand, in 3D-PDF maps, the peak density is significantly lower than in powder PDFs, because by mapping peaks in three dimensions instead of one, the angular information about interatomic vectors is preserved. The requirements for resolution in three-dimensional PDF space are therefore not so stringent. Advantageously in 3D-ΔPDFs, information about ordered parts of the crystal is not visible, and hence the peak density is further reduced.

3. Pair distribution function analysis and modelling in three-dimensional space: decagonal Al–Cu–Co

3.1. The average structure of *d*-Al–Cu–Co

Decagonal Al–Cu–Co was the first stable decagonal quasicrystal ever observed (He *et al.*, 1988). The structure was first refined by Steurer & Kuo (1990) by the use of five-dimensional techniques. A number of further structure models have been published since then. For an overview see *e.g.* Steurer (2004) and references therein. All these models have in common that they only describe the ~4 Å periodic average structure, while local ~8 Å ordering is unaccounted for. Further, these models are just approximate, partly inconsistent descriptions of the quasiperiodic structure, leaving open many questions. For the present study, an average electron density distribution calculated from the structural description of $Al_{65}Cu_{20}Co_{15}$ by Steurer & Kuo (1990) was chosen to serve as a basic model for the average structure (Fig. 1).

As is common for decagonal phases, *d*-Al–Cu–Co is built up of tenfold columnar clusters,[2] which are periodic along their unique tenfold *c* axis.[3] Along lateral directions, the clusters are packed with different amounts of overlap, resulting in a two-dimensional quasiperiodic distribution normal to the cluster axis. Geometrically, the structure may be interpreted as a sequence of two-dimensional quasiperiodic layers, which are stacked periodically along the *c* axis. The spacing between these layers is ~2 Å. From a crystal-chemical point of view, interpretation as a layered structure, however, is inappropriate, as interatomic distances within and between the layers are of the same scale. The periodicity of the average structure of *d*-$Al_{65}Cu_{20}Co_{15}$ along **c** is ~4 Å, *i.e.* one period covers two layers. Its space group was determined by Steurer & Kuo (1990) to be $P10_5/mmc$, with periodicity c = 4.148 Å. The existence of ~8, ~12 and ~16 Å periodic *d*-Al–Cu–Co phases has also been reported (He *et al.*, 1988), but so far their atomic structures have not been investigated.

---

[2] In this paper, the term cluster is solely used in the sense of geometrical structure motifs, and not to indicate strong internal bonds.

[3] In the case of decagonal quasicrystals, the unique periodic axis is usually denoted as the a_5 axis, following the five-dimensional coordinate system $a_1 \ldots a_5$. In the following, the classical crystallographic notation *c* axis is used [parallel to the *z* direction in an orthogonal coordinate system (*x*, *y*, *z*)], in order to outline that PDF analysis is carried out in three-dimensional space, and no *n*-dimensional description is needed. Similarly, reciprocal-space coordinates will be denoted by the coordinate triplet *hkl* instead of the five-dimensional notation $h_1 \ldots h_5$.

3.2. Disorder in related decagonal and approximant structures

Disorder and diffuse scattering in *d*-Al–Cu–Co has not been investigated in detail so far, except the two-dimensional PDF analysis by He *et al.* (1993) mentioned above. However, several studies were carried out for different decagonal phases of Al–Ni–Co, including the ~8 Å periodic disordered superstructure (*e.g.* Frey & Steurer, 1993; Frey *et al.*, 2000, 2002; Kobas *et al.*, 2005*a*,*b*). *d*-Al–Ni–Co is structurally closely related to *d*-Al–Cu–Co and their diffuse scattering intensity distributions are similar [see Figs. 2 and 9 in this work and, *e.g.*, Figs. 3 and 4 of Katrych & Steurer (2004)]. Thus the results for disorder in *d*-Al–Ni–Co are considered to be relevant for the ~8 Å superstructure of *d*-Al–Cu–Co, and *vice versa*. Frey *et al.* (2000) postulated an ~8 Å superstructure of *d*-Al–Ni–Co that is caused by off-plane displacements in the **c** direction ('puckering'). Cervellino *et al.* (2002) found that every second layer of *d*-$Al_{70.6}Co_{6.7}Ni_{22.7}$ is puckered and the others are flat. The flat layers act as mirror planes for *z* displacements in the puckered layers, resulting in a four-layer superstructure with a period of ~8 Å. This superordering is found in columnar domains, which are long-range ordered along the *c* axis. In the real structure, neighbouring clusters may be either at the same *z* coordinate or displaced by ~4 Å along the **c** direction, leading to an average periodicity of ~4 Å. Steurer *et al.* (2001) have shown that the diffuse scattering in the main layers of *d*-Al–Ni–Co, which represent the ~4 Å periodic structure, undergoes a different thermal evolution compared to the diffuse interlayers, which reflect disorder of the ~8 Å superstructure. They concluded that the main and interlayers represent different, mostly uncorrelated, types of disorder. Kobas *et al.* (2005*b*) have shown that the diffuse scattering in the main layers of $Al_{70}Co_{12}Ni_{18}$ is mainly caused by phasonic disorder, which can also be interpreted as fivefold orientational disorder of ~20 Å-sized clusters. Weber *et al.* (2004) investigated the thermal behaviour of the diffuse interlayers of *d*-Al–Ni–Co using 'zero-layer Patterson map' analysis, which is a simplified variant of the 3D-PDF method presented here. It was shown that a columnar cluster-like arrangement with diameter of about 15 Å is stable over a wide thermal range, whereas formation of larger superclusters is temperature dependent.

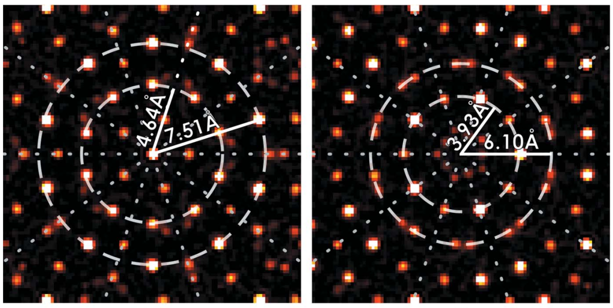

(*a*) (*b*)

Figure 1
Electron density maps of the two quasiperiodic atomic layers of the average structure of *d*-$Al_{65}Cu_{20}Co_{15}$, based on structure factor amplitudes and phases from Steurer & Kuo (1990). The two sections (*a*) and (*b*) are separated by a distance of ~2 Å along the periodic direction. Ring-like structural motifs that were identified to be disordered are marked. Mirror planes of the average structure, which are *c*-glide planes in the local cluster, are highlighted (dotted lines). The edge length of each image is 20 Å.

The presence of flat and puckered layers is also known from periodic approximant structures to *d*-Al–Cu–Co. For an overview of known approximants see Steurer (2004) and references therein. Approximants to *d*-Al–Cu–Co mostly form a monoclinic $Al_{13}Co_4$-type structure (Hudd & Taylor, 1962), which is closely related to the $Al_{13}Fe_4$ type (Black, 1955*a*,*b*). Other approximant structures are those of orthorhombic $Al_{13}Co_4$ (Grin *et al.*, 1994*a*; Fleischer *et al.*, 2010).

3.3. Experimental and data processing

The single-crystal diffraction data of decagonal $Al_{65}Cu_{20}Co_{15}$ were measured at the Swiss–Norwegian beamline (SNBL) at the ESRF in Grenoble, France, at ambient conditions (Scholpp, 2001). The wavelength was $\lambda = 0.70019$ Å. The oscillation range measured was $\varphi = 180^\circ$, with step increments of 0.5° and an exposure time of 50 s per frame. A Marresearch mar345 image-plate detector was used. The crystal–detector distance was 150.0 mm. The orientation matrix of the sample was determined using the software package *XDS* (Kabsch, 1993). The period along **c** of the average structure was determined to be $c_{\rm aver} = 4.11\ (8)$ Å. The data were reconstructed into undistorted reciprocal-space coordinates using the software *Xcavate* (Estermann & Steurer, 1998). Nineteen layers at $l = -4.5, -4.0, \ldots, 4.0, 4.5$ were reconstructed. Each layer had an extent of 1582 × 1582 pixels in the orthogonal *h* and *k* directions with a pixel size of 0.0015 Å^{-1}, thus covering a range of -1.187–1.187 Å^{-1} (reciprocal-space length units are defined as $d^*_{hkl} = 1/d_{hkl} = 2\sin(\Theta)/\lambda$, Θ being the Bragg angle, *i.e.* they are a factor 2π smaller than the reciprocal-space units frequently used in powder PDF investigations). According to the Laue symmetry 10/*mmm*, there are 40 possible symmetrically equivalent orientations, which can be used for symmetry-equivalent averaging. Since the diffraction patterns obtained from *Xcavate* are mapped to an orthogonal grid, there is a mismatch between the tenfold symmetry of the scattering intensities and the orthogonal coordinate system of the data representation. Thus, symmetry-equivalent averaging cannot be achieved directly by linear transformation of one reconstructed data set. Consequently, the scattering intensities were reconstructed into orthogonal grids in all possible symmetrically equivalent orientations (in total 380 layers), *i.e.* symmetry transformation was done before mapping the reconstructed pattern to the Cartesian grid. Subsequently, the beam-stop shadow was masked, and the symmetrically equivalent data sets were averaged.

Within the experimental resolution, the reciprocal space layers are sharp along **c*** (Fig. 2*a*). In order to compensate for experimental resolution effects and inaccuracies of the orientation matrix, reconstructions of the layers were not calculated as sharp cuts through reciprocal space, but integrated over a thickness of ±0.005 Å^{-1} along **c***. As the background intensities are monotone between the layers, it can be assumed that the background within a layer can be approximated by interpolation of the background intensities above and below the layers. For that reason, pure background layers were reconstructed in all symmetrically equivalent orientations on both sides of the layers at a distance of 0.022 Å^{-1} (in total 760 layers) and processed in the same way as the diffuse layers. The estimated interpolated background intensities were then subtracted from the diffuse layers. It was not possible to extract integrated intensities of Bragg reflections from the experimental data, because the experiment was optimized for the measurement of diffuse intensities, and thus most of the Bragg reflections were saturated.

As it will be explained below, diffuse intensities of the Bragg layers were excluded from the computation of the ΔPDF. For this reason, only the intensities of the ten diffuse interlayers at $l = -4.5, \ldots, 4.5$ were included in the further process. The intensities of the nine main layers at $l = -4.0, \ldots, 4.0$ were set to zero. The 3D-ΔPDF (see Fig. 3) was computed using the fast Fourier transform routines provided by the *FFTW* software library (Frigo & Johnson, 2005). In contrast to the coordinate triplet x, y and z used in real space, the coordinates in PDF space are denoted by x_P, y_P and z_P henceforth. Even though the two coordinate systems have the same metric, this notation emphasizes the different characteristics of the two spaces. x_P, y_P and z_P are given in Cartesian units, while Z_P represents fractional units with respect to the average ~4 Å periodicity. The computed 3D-PDF has dimensions of 1582 × 1582 × 20 pixels. The voxel size of the resulting pattern is 0.411 Å along the periodic direction and 0.421 Å perpendicular thereto. This amounts to a rectangular volume with an extent of $x_P = \pm333.2$ Å, $y_P = \pm333.2$ Å and $z_P = -4.11$–3.70 Å. As the Fourier transform is symmetry conservative, the 3D-ΔPDF map has the Laue symmetry of the diffuse scattering pattern, *i.e.* $10/mmm$.

3.4. Observations and qualitative interpretation of diffraction patterns and ΔPDF maps

The single-crystal diffraction pattern of *d*-Al–Cu–Co (Fig. 2) shows a sequence of layers containing Bragg and diffuse scattering (Bragg layers) and halfway between layers with diffuse scattering only (interlayers). The Bragg layers are separated by a distance of $1/c_{\rm aver} = 0.243$ Å^{-1}. Inspection of the odd-numbered Bragg layers shows that the *c*-glide plane symmetry required by the space group $P10_5/mmc$ as proposed by Steurer & Kuo (1990) is weakly broken. From the behaviour of the extinction rule-violating reflections (*i.e.* symmetry and profiles) it is not expected that this is an artefact from *Umweganregung*. The presence of interlayers indicates that the periodicity of the real structure is twice the average translation, *i.e.* $c_{\rm real} = 8.23$ Å. Along **c*** interlayers are as sharp as Bragg reflections, and consequently, the underlying disordered motif is long-range ordered along the periodic direction and short-range ordered along quasiperiodic directions. A set of five extinction zones, which were already reported in selected-area electron diffraction patterns by Saitoh *et al.* (1996), is observable in all interlayers (Figs. 2*c* and 9). As these extinction zones cannot be found in the Bragg layers, the presence of local *c*-glide plane symmetry with respect to the ~8 Å superstructure can be assumed. Note that these local *c*-glide planes are not identical to those of space group $P10_5/mmc$ of the average structure.

Diffuse scattering present in the Bragg layers is not considered in the following investigations. We know from *d*-Al–Ni–Co that it is most probably caused by phasonic disorder, which is not correlated with disorder of the ~8 Å superstructure (Kobas *et al.*, 2005*b*; Weber *et al.*, 2007). Similarity of the diffuse diffraction patterns of *d*-Al–Ni–Co and *d*-Al–Cu–Co corroborates this supposition also in the present case. This assumption is further supported by the observation

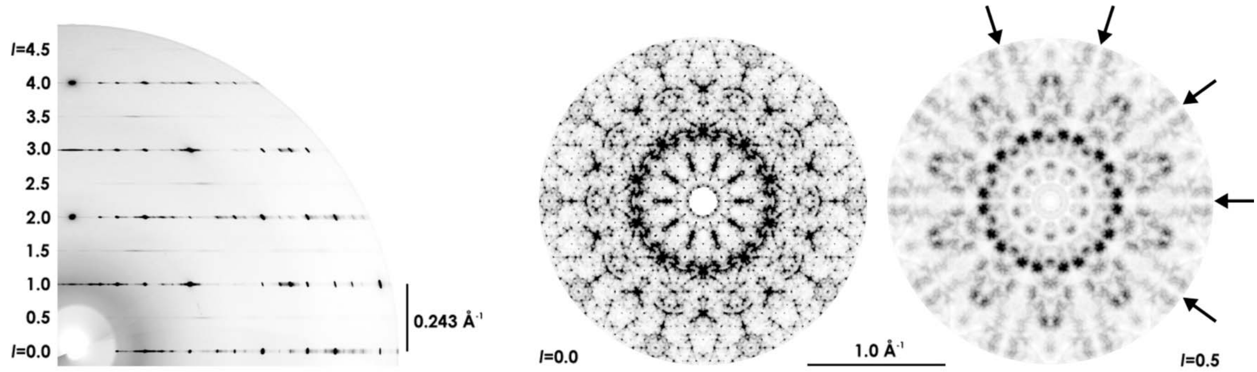

(*a*) (*b*) (*c*)

Figure 2
Experimental X-ray diffraction pattern of $Al_{65}Cu_{20}Co_{15}$. (*a*) Section including the periodic axis *c**. Between the Bragg layers at integral positions of *l*, weaker diffuse interlayers are present. (*b*) Main layer at $l = 0.0$, containing Bragg and diffuse intensities. (*c*) Diffuse interlayer at $l = 0.5$. Arrows mark tenfold extinction zones (see text). Images (*b*) and (*c*) are symmetry averaged, and background intensities were removed.

that the appearance of diffuse scattering in Bragg layers of *d*-Al–Cu–Co differs clearly from the diffuse intensities in the interlayers (*cf.* Fig. 2).

The diffraction data set is a discrete real even function, *i.e.* $I(\mathbf{h}) = I(-\mathbf{h})$. Consequently, Fourier transformation can be reduced to a real discrete cosine transform (DCT). By the use of diffraction intensities from interlayers only [$l = (2n+1)/2$, n is an integer], which represent information about the ~8 Å disorder, the 3D-ΔPDF is calculated as

$$P_\Delta(x_P, y_P, Z_P) = 2\sum_{n\geq 0}\sum_{h,k}\big\{I[h,k,(2n+1)/2] \times \cos\big[2\pi(hx_P + ky_P)\big]\cos\big[\pi(2n+1)Z_P\big]\big\}. \quad (14)$$

The term $\cos[\pi(2n+1)Z_P]$ is +1 for all even integral values of Z_P and −1 for all odd-numbered integral Z_P. At half-integer Z_P positions, the term is zero. Accordingly, the 3D-ΔPDF has mirror planes at integral Z_P (*i.e.* at $z_P \simeq \ldots, -4, 0, 4, \ldots$ Å) and anti-mirror planes halfway in between ($z_P \simeq \ldots, -6, -2, 2, 6, \ldots$ Å) (*cf.* Fig. 4*d*). In the anti-mirror planes, the ΔPDF density must be zero, *i.e.* the interatomic correlations of the real structure over distances $z_P = (2n+1)c_{\rm aver}/2$ are identical to those found in the average structure. Symmetry considerations allow us to restrict our attention to $0 \leq Z_P \leq 0.5$ ($0 \leq z_P \leq {\sim}2$ Å). According to the z_P voxel size, this includes the layers at $z_P = 0.00, 0.41, 0.82, 1.23, 1.65$ and 2.06 Å (Fig. 3).

Strong correlation densities up to distances of about 14.5 Å away from the central axis are found in (x_P, y_P) layers at $z_P = 0.00$, 0.82 and 1.65 Å. Beyond this circular region, only weak correlations are observed (Fig. 3) up to radial distances of about 100 Å, which will be neglected in the following. Consequently, the considered maximum correlation length (perpendicular to the cluster axis) for the interpretation of the disordered structure is about 14.5 Å. Layers at $z_P = 0.41$ and 1.23 Å show throughout very weak densities. The layer at $z_P = 2.06$ Å shows only zero densities, as expected from equation (14).

Geometrically, *d*-Al–Cu–Co can be seen as a layered structure, which is also reflected in the PDF space properties. Features in the PDF maps can be easily assigned to intralayer and interlayer vectors by considering their z_P components. If a four-layer periodic alternating sequence of puckered and flat layers and a constant puckering amplitude Δz for all atoms in the puckered layers is premised, intralayer disorder within flat layers occurs at $z_P = 0.00$ Å only, while intralayer disorder within puckered layers is found in the layers at $z_P = 0.00$ Å *and* $z_P = 2\Delta z$ (*cf.* Fig. 4). The splitting of the last-mentioned correlation vectors is due to atom pairs that show parallel or antiparallel off-plane displacements, respectively. Correlations between next neighbouring flat and puckered layers are observed in the layers at $c_{\rm real}/4 - \Delta z$ and $c_{\rm real}/4 + \Delta z$ ($c_{\rm real}/4$ is the distance between two layers). It is important that the layer

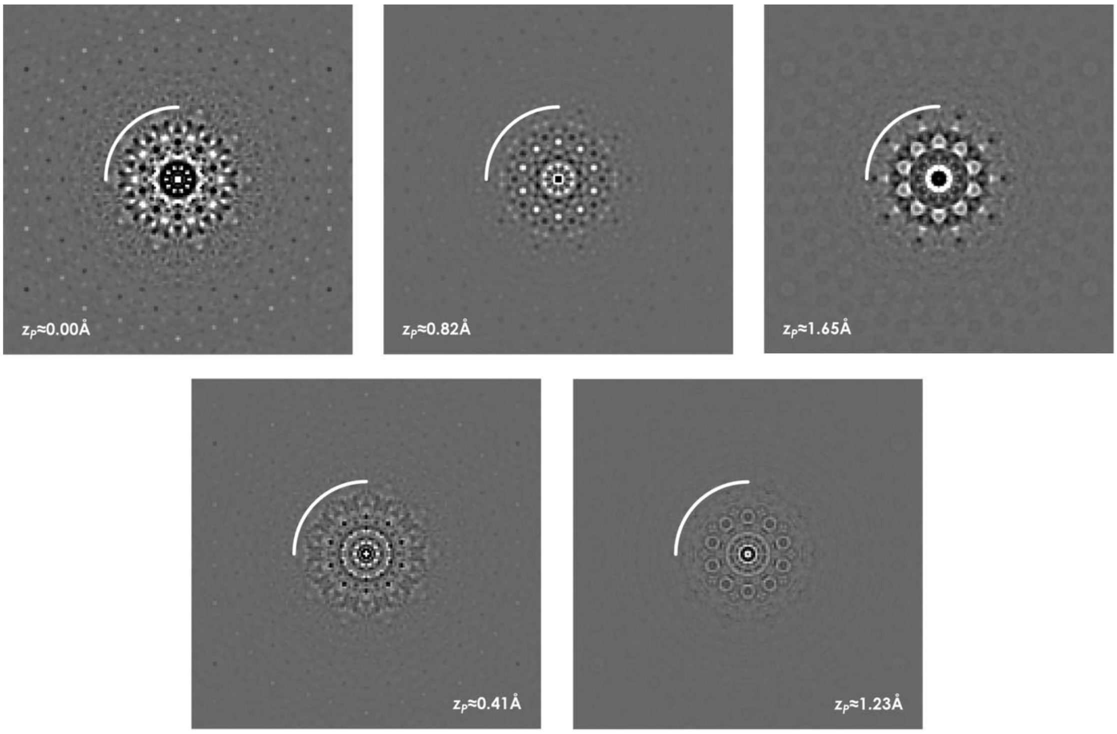

Figure 3
Two-dimensional (x_P, y_P) sections at different z_P of the 3D-ΔPDF of d-Al$_{65}$Cu$_{20}$Co$_{15}$, computed from single-crystal X-ray diffuse scattering. Positive correlations are in white and negative ones in black. The centre of the sections is at $x_P = y_P = 0$. The images cover ±35.17 Å along each axis. As a reference, a circular arc with a radius of 14.5 Å is drawn in each image, corresponding to the considered maximum correlation length used for modelling. Note that the section at $z_P = 2.06$ Å contains only zero values and is not shown here.

at $z_P = 2\Delta z$ contains exclusively information about puckered but no information about flat layers, provided that $c_{\rm real}/4 - \Delta z$ is significantly different from $2\Delta z$, *i.e.* in the case of *d*-Al–Cu–Co $\Delta z << {\sim}0.69$ Å. From approximant structures it is known that puckering amplitudes are typically of the order of less than 0.4 Å. In the experimental ΔPDF maps, there are strong density peaks in the layer at $z_P = 0.82$ Å. These are an indication that this layer represents information about disorder in the puckered layers, with an average puckering amplitude of roughly 0.82 Å/2 $\simeq$ 0.4 Å. When comparing the layer at $z_P = 0.82$ Å with that at $z_P = 0.00$ Å (Fig. 3), one recognizes that the main peaks of the 0.82 Å layer also occur in the 0.00 Å layer, but their signs are inverted. The opposite is not the case, *i.e.* there are features in the 0.00 Å layer that are not observed in the 0.82 Å layer. This complimentary behaviour can be easily explained (*cf.* also Fig. 4): in contrast to the average structure, a given atomic pair in the real puckered layer can only show parallel or antiparallel out-of-plane displacements, but never both at the same time. For given x_P and y_P coordinates, preference for parallel displacements leads accordingly to positive peaks at $z_P = 0.00$ Å and negative peaks at $z_P = 0.82$ Å. In the case of antiparallel displacements the behaviour is inverse. In particular, the pattern in the 0.00 Å layer is expected to be the negative of the pattern in the 0.82 Å layer if solely information about the puckered layers is considered. Any deviations therefrom must hence be due to disorder in the flat layer.

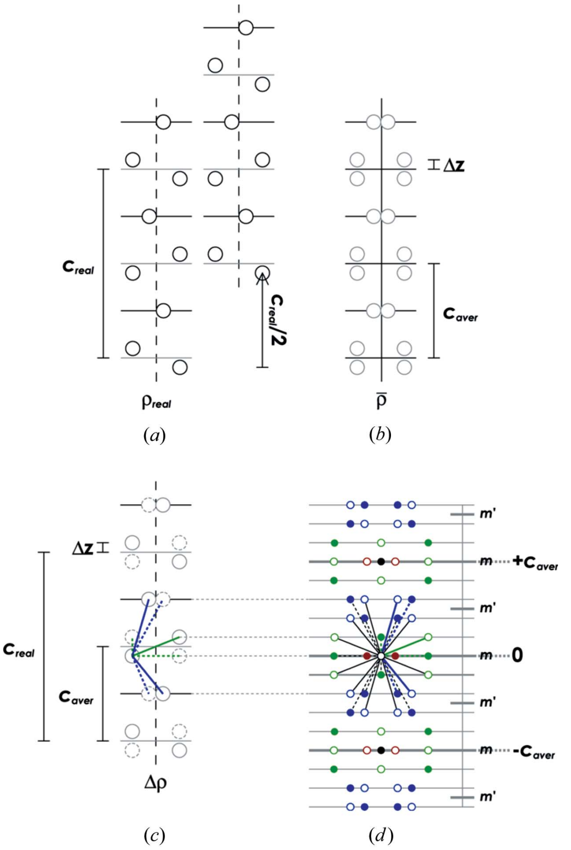

Figure 4
Schematic description of structural disorder by columnar units, as found in *d*-Al–Cu–Co. (*a*) Columnar, laterally uncorrelated, real structure motifs shifted by $c_{\rm real}/2$ relative to each other. Full circles indicate occupied atom positions. Within each column, there is an alternating sequence of puckered layers with off-plane shifts of $\pm\Delta z$, and of flat layers with in-plane shifts. Glide-plane symmetry (dashed lines) along **c** and mirror symmetry perpendicular thereto (solid black lines) in the flat layers effect a local periodicity of $c_{\rm real} = 2c_{\rm aver}$. (*b*) Average structure of the disordered structure shown in (*a*). Grey circles indicate half-occupied atomic sites. Superposition of the two shifted columns reduces the period to $c_{\rm aver}$, transforms the *c*-glide plane to a mirror plane and causes new mirror planes in the puckered layers. The symmetry of (*b*) is a supergroup of (*a*). (*c*) Difference structure of (*a*) and (*b*), *i.e.* $\Delta\rho(\mathbf{r}) = \rho_{\rm real}(\mathbf{r}) - \overline{\rho}(\mathbf{r})$. Full circles indicate positively half-occupied difference atom positions; dashed circles indicate negatively half-occupied ones. Selected interatomic vectors from one arbitrarily chosen positive difference atom in a puckered layer to atoms in the same layer (green) and adjacent flat layers (blue) are marked. Solid lines indicate positive correlation; dashed lines show negative correlation. (*d*) The ΔPDF resulting from (*c*). Positive pair correlations are marked with open circles; negative pair correlations are marked with solid circles. Green: pair correlations between atoms in puckered layers; blue: puckered–flat correlations; red: flat–flat correlations. The interatomic vectors as shown in (*c*) are marked in the same colours; their symmetric equivalents are marked in black. *m* and *m*′ indicate mirror and anti-mirror planes (see text), respectively. As the structure is long-range ordered in the **c** direction, the PDF is also periodic in this direction with period $2c_{\rm aver}$. Note that, for symmetry reasons, both in-plane and correlated off-plane shifts are required to generate a ΔPDF that contains nonzero intra- *and* interlayer densities.

Given a puckering amplitude of $\Delta z \simeq 0.4$ Å, correlations between disordered atom positions in puckered and in flat layers are expected to be found at $z_P = c_{\rm real}/4 \pm \Delta z$, as well as in symmetrically equivalent layers. This explains the presence of strong densities in the corresponding experimental ΔPDF layer at $z_P = 1.65$ Å (Fig. 3).

The influence of the experimental resolution function $r_{\rm s}(\mathbf{r})$ on the PDF density was calculated from profiles of unsaturated Bragg peaks [equation (10)]. The estimated average FWHM of the Bragg peaks, w_r, along quasiperiodic directions is about 0.006 Å^{-1}. Consequently, the attenuation of PDF densities 14.5 Å apart from the tenfold axis is about 3%, which was considered to be negligible. As the experimental diffuse layers were integrated along **c***, the experimental resolution has no effect on the ΔPDF densities in directions along **c**.

3.5. Modelling

Based on the qualitative interpretation of the experimental data and considering the analogy to ~8 Å structure models in *d*-Al–Ni–Co and approximant structures, it is concluded that the disorder has its origin in columnar clusters with a diameter of ~14.5 Å. For the sake of simplicity, the occurrence of one single prototypic cluster type is premised. Within this columnar motif, an alternating sequence of flat and puckered layers is assumed. The cluster may randomly occupy one of two possible positions separated by a shift distance of $c_{\rm aver} \simeq 4$ Å along the periodic direction. Internally, the model structure of the clusters is perfectly ordered, *i.e.* all columns incorporate an identical pair correlation distribution. Since the weak ΔPDF densities more than ~14.5 Å away from the tenfold axis are ignored, also all correlations between displacements of laterally adjoining clusters are neglected.

Furthermore, it is assumed that the clusters occupy the two possible z positions with the same probability. For such a model the diffuse scattering intensities can be easily calculated as (*cf.* Weber *et al.*, 2001)

$$I_{\rm diffuse}(\mathbf{h}) \propto \left|{\rm FT}\left[\rho_{\rm Cl}(\mathbf{r}) - \rho_{\rm Cl'}(\mathbf{r})\right]\right|^2 = \left|f_{\rm Cl}(\mathbf{h}) - f_{\rm Cl'}(\mathbf{h})\right|^2, \quad (15)$$

where $f_{\rm Cl}(\mathbf{h})$ and $f_{\rm Cl'}(\mathbf{h})$ are the Fourier transforms of the cluster electron density $\rho_{\rm Cl}(\mathbf{r})$ and its variant $\rho_{\rm Cl'}(\mathbf{r})$ shifted by $c_{\rm aver}$, respectively. Accordingly, equation (15) can be rewritten as (remember that l refers to the average structure)

$$\begin{aligned} I_{\rm diffuse}(\mathbf{h}) &\propto \left|f_{\rm Cl}(\mathbf{h}) - f_{\rm Cl}(\mathbf{h})\exp(2\pi il)\right|^2 \\ &= 2f_{\rm Cl}(\mathbf{h})f^*_{\rm Cl}(\mathbf{h})[1-\cos(2\pi l)]. \end{aligned} \quad (16)$$

Diffuse intensities from this model are extinct in all Bragg layers but the interlayers show a maximum intensity $4f_{\rm Cl}f^*_{\rm Cl}$. Note that there is only a contribution to $I_{\rm diffuse}(\mathbf{h})$ when $\rho_{\rm Cl}(\mathbf{r}) \neq \rho_{\rm Cl'}(\mathbf{r})$, *i.e.* nondisordered parts of the structure do not have to be part of the model. Note further that the diffuse intensity of this model only depends on the internal structure, but not on the spatial distribution of the clusters in the crystal. This drastically simplifies further investigations, because the spatial quasiperiodic arrangement of the clusters and the relationship between clusters do not have to be modelled or even to be known, and disorder can be characterized just by an atomic model for the disordered part of the ~14.5 Å cluster. Owing to extinctions in the diffuse interlayers, additional local c-glide planes, which are not part of the average structure, are expected to be present in the disordered structure. Their translation component is $c_{\rm real}/2 = c_{\rm aver}$, *i.e.* atoms lying exactly on such a c-glide plane are invariant with respect to the ~4 Å displacements. Such atoms do not contribute to scattering in interlayers, and they do not have any influence on the calculation of the ΔPDF maps. Diffuse scattering intensities were calculated on a grid that has the same properties as the grid representing the experimental diffuse scattering. Before Fourier transformation, the simulated diffuse intensities were multiplied with a mask function having unit weights at reciprocal space positions, where experimental diffraction data were available, and zero values elsewhere. This guarantees that truncation effects in experimental and modelled ΔPDF maps are the same.

A candidate for the demanded ~14.5 Å cluster is found in the average electron density calculated from the structure model reported by Steurer & Kuo (1990), as shown in Fig. 1. To test both the model developed so far and the applicability of this cluster model, we first tried to reproduce the ΔPDF map of the layer at z_P = 0.82 Å, *i.e.* to model disorder in the puckered layers. Because of the limitations of their average structure model, reliable information about off-plane displacements was not available from Steurer & Kuo (1990). Accordingly, the displaced atoms had to be identified from the experimental ΔPDFs. By comparison of the interatomic vectors of two tenfold rings with radii $r_{\rm pi}$ = 4.64 Å and $r_{\rm po}$ = 7.51 Å (Fig. 1*a*) with the ΔPDF map at z_P = 0.82 Å, these vectors could be associated with alternating positive and negative ΔPDF peaks (Fig. 5). Remember that positive correlations in the 0.82 Å ΔPDF layer mean that atoms connected by a corresponding vector prefer opposite off-plane displacements, while negative peaks indicate that relevant atoms tend to be on the same side of the puckered layer. Hence, the ΔPDF map may be understood by supposing that all tangentially and radially next neighbouring atoms of the two rings prefer antiparallel z displacements. The ΔPDF of this initial model was calculated as explained above, under the assumption that the puckering amplitude is 0.4 Å for all atoms. The radii of the rings from the centre of the cluster were estimated from the average structure as r_1 = 4.64 Å and r_2 = 7.51 Å. All atomic sites were decorated with Al atoms. Other atoms of the puckered layers in the surroundings were assumed to be ordered, because they all lie on c-glide planes (Fig. 1).

The resulting diffraction pattern and ΔPDF of this initial model are shown in Fig. 6. Although the model is very simple, it nicely reproduces the ΔPDF of the layer at z_P = 0.82 Å and major parts of the layer at z_P = 0.00 Å. The most obvious difference between observed and calculated densities in the 0.00 and 0.82 Å layers is that the experimental densities decay more rapidly with increasing distance from the tenfold axis than is the case in the modelled pattern. The 0.00 Å layer shows some features that are not covered by the model, because disorder of flat layers was not considered at this point. For the same reason, the layer at z_P = 1.65 Å, which reflects the correlations between puckered and flat layers, is practically featureless. From the good agreement between experimental and modelled ΔPDF layers at z_P = 0.82 Å, it can be concluded that the structural motif highlighted in Fig. 1 is most probably the disordered object of interest, and that a reasonable model for describing the puckering was found. Note that such conclusions, drawn from comparison of

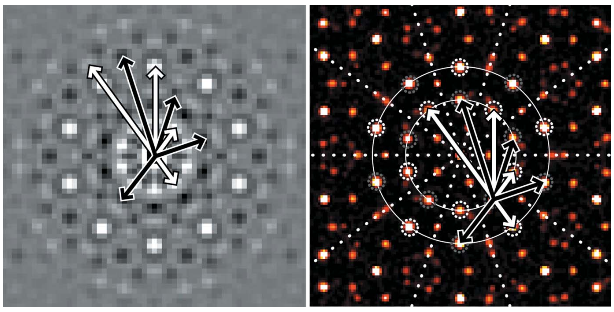

Figure 5
Comparison of the 3D-ΔPDF at z_P = 0.82 Å and the electron density of the average-structure solution on the same scale. In each image, an identical group of interatomic vectors with a vertical component $\Delta z \simeq 0.82$ Å is drawn. The colour of the arrows corresponds to the sign of the ΔPDF density linked with the respective vector, *i.e.* white coloured arrows indicate positive pair correlation and black coloured arrows negative. In the electron density map, the vectors point from an appropriate atom on the inner ten-membered ring (*cf.* Fig. 1*a*) to its neighbours on the same and on the surrounding outer ring. The sequence of alternating signs of pair correlations (as seen from the origin atom, marked with white and grey dotted circles) indicates a puckered arrangement of the respective atoms by Δz in the disordered real structure. Mirror symmetry of the average structure is replaced by local glide plane symmetry in the real structure (dotted lines, *cf.* Fig. 1*a*).

experimental and modelled ΔPDF maps, cannot be obtained facilely from corresponding diffuse scattering patterns (Fig. 6). The reciprocal space agreement between experiment and intensities from incomplete models is, generally, very low and does not allow conclusions about the quality of such partial models.

As the cluster is a three-dimensional object with one-dimensional periodicity, its symmetry can be described by a rod group. In accordance with the electron density shown in Fig. 1, the rod group of the average cluster is assumed to be $\not{p}\overline{10}2m$, while the symmetry of the real cluster has to be a subgroup thereof. Group $\not{p}\overline{10}2c$ is a proper subgroup that is consistent not only with the diffuse scattering extinction rules but also with the condition $c_{\rm real} = 2c_{\rm aver}$, as well as with the symmetry of the puckered layer model discussed above. In the following, it was therefore accepted as the symmetry of the real cluster model.

The next step was to complete the disordered structural motif by modelling the flat layers. From the average structure model, the most obvious candidates for representing disorder in flat layers are the tenfold ring of split atoms at a radius of $r_{\rm fo}$ = 6.10 Å, having unphysical short interatomic distances in the average structure, and the smaller ten-membered ring with a radius of $r_{\rm fi}$ = 3.93 Å (Fig. 1*b*). Efforts were made to reproduce at least some parts of the z_P = 1.65 Å ΔPDF pattern and of the missing features in the z_P = 0.00 Å map by correlating disorder in puckered layers with disorder in the split positions of the flat layers. The models were restrained such that (i) the atoms in the real structure were close to the positions in Fig. 1(*b*), (ii) atoms lying on *c*-glide planes in Fig. 1(*b*) were not considered and (iii) rod-group symmetry $\not{p}\overline{10}2c$ was fulfilled. The model of disorder in the puckered layers was left unchanged at this stage of modelling. None of these attempts, however, improved the agreement with the experimental ΔPDF. After several trial-and-error attempts, a convincing model was obtained by dropping constraint (i), *i.e.* split atoms were allowed to move in a distance range comparable to the shifts found in the puckered layers away from the initial positions, and by releasing restraint (ii), *i.e.* atoms lying on a *c*-glide plane were allowed to move away from the planes and thus to contribute to the diffuse scattering and to the ΔPDF maps. Atoms on the small pentagonal motif (r = 1.63 Å) in the centre of the flat rings were not allowed to move away from the *c*-glide plane, because limited space in this area would not allow a reasonable arrangement of these atoms in consideration of the given rod group. The origin of this motif is possibly phasonic disorder that is not related to superstructure disorder.

With the assumed rod-group symmetry of the real structure, off-plane disorder in the flat layers is not possible, because the

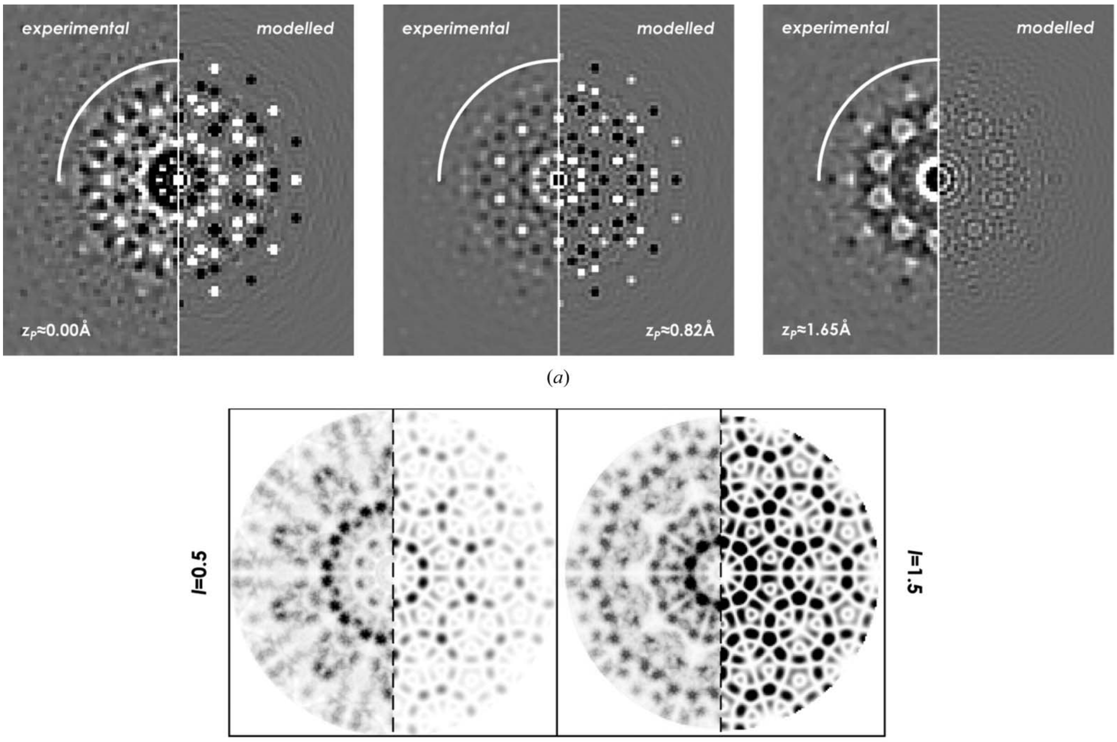

(*a*)

(*b*)

Figure 6
(*a*) Comparison of the experimental and modelled 3D-ΔPDF of *d*-$Al_{65}Cu_{20}Co_{15}$. The underlying incomplete structural ~8 Å model of disorder contains only two puckered layers, centred at z = 0 and $z = c_{\rm real}/2$. The model does not cover the ΔPDF densities at z_P = 1.65 Å; the observable weak densities in that section are due to truncation effects. The area covered by each image is ±21.27 Å along each axis. The colouring scheme is the same as in Fig. 3. (*b*) Corresponding diffuse scattering intensities in two diffuse interlayers of the partial structural model. The diffraction pattern of the model structure shows a strong variation of intensity in different layers. Image sizes are the same as in Fig. 9.

mirror plane lying in these layers would cause the interatomic distances in the real cluster to be too short. The same mirror planes are also responsible for the fact that in-plane disorder in the puckered layers is not considered in our models. Any atom having no off-plane displacement would be transformed to an equivalent atom with same x, y coordinates and $z = nc_{\rm aver}$. As a consequence, it would not be disordered with regard to the ~4 Å shifts discussed in this study.

The question about the elemental decoration of the atomic sites has not been addressed so far. As mentioned above, the average structure of quasicrystals is usually not as accurately known as is the case for periodic structures. Correlations between occupation factors of elements and displacement parameters, as well as shortcomings of the refined average model, often do not allow a precise definition of the distribution of elements in the average structure. Because of this lack of information, correct assignment of elements to atomic sites is even more complicated when modelling the real structure. On the other hand, differences in the scattering power between Al and transition metals (TMs) must be addressed in a quantitative refinement. To overcome this problem, all atomic sites were considered to be occupied by the same element (Al), but the local scattering power of a specific site was accounted for by multiplying it with a weighting factor to be refined.

The observation that ΔPDF densities in the experimental pattern decay much more quickly than those in the simulated maps (see Fig. 6) was considered by multiplying the modelled ΔPDF map by a cylindrical exponential attenuation function $t(\mathbf{r}_P) = \exp\{-[(ax_P)^2 + (ay_P)^2]^{1/2}\}$, having one refinable parameter, a. If a becomes significantly larger than zero, it must be concluded that the initial assumption of clusters having perfect internal lateral order is not correct, because intra-cluster disorder leads to a more rapid decay of atomic correlations than in the case of perfectly ordered clusters. In addition, any modelling of phononic disorder was discarded.

3.6. Refinement, results and discussion

In order to obtain a best fit between experimental and calculated ΔPDF patterns, the numerical parameter values of the model were optimized using the differential evolution method (Storn & Price, 1997). The agreement between experimental and calculated ΔPDF maps was quantified by a reliability factor comparing the ΔPDFs voxel by voxel:

$$R = \left[\frac{\sum w_i\left(\Delta P_i^{\rm obs} - s\Delta P_i^{\rm calc}\right)^2}{\sum w_i\left(\Delta P_i^{\rm obs}\right)^2}\right]^{1/2}. \qquad (17)$$

The scaling factor s was determined by a linear least-squares fit prior to computation of R. The weighting factor w_i was used to restrict the computation of the R value to the regions of interest, *i.e.* to voxels having a distance less than 16.6 Å away from the tenfold axis. Voxels within this volume were given unit weights; otherwise the weights were set to zero.

After initial refinements, it turned out that only one of the two fivefold atomic orbits of the inner ring in the flat layers deviated significantly from the c-glide planes. For the atoms on the other orbit either they stayed close to the c-glide plane or the scattering weighting factor refined to very small values. In both cases corresponding atoms would not significantly contribute to the ΔPDF maps, and therefore they were not included in further refinements.

To account for the columnar shape of the structural model, a cylindrical coordinate system (z, r, α) was used to describe the cluster's geometry. Coordinates and a scattering weighting factor were refined for each symmetrically independent atom position. For definitions of the free parameters used in model optimization see Table 1 and Fig. 7. The z coordinates of atoms in the flat layers were not refined but were constrained to the

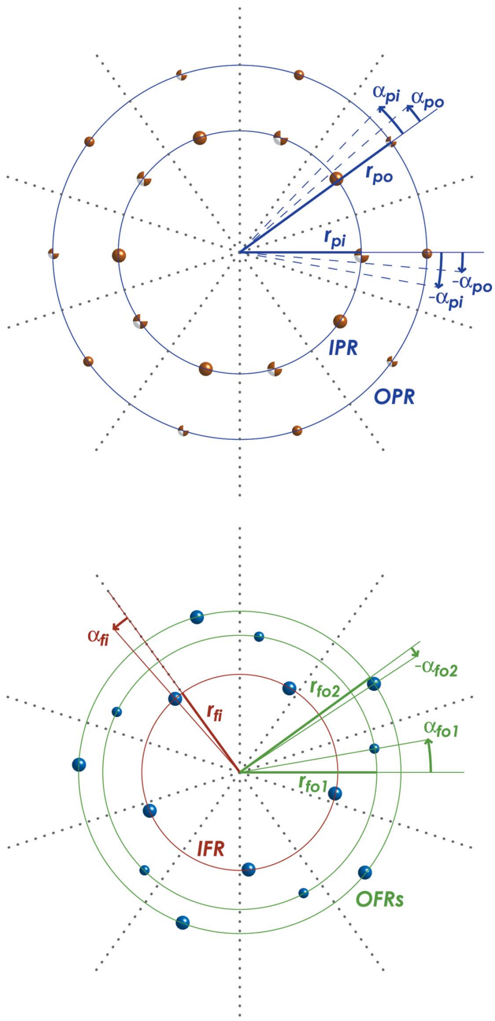

Figure 7
Single atomic layers in projection parallel to $\mathbf{c}$ of the optimized ~8 Å real-structure motif of d-Al$_{65}$Cu$_{20}$Co$_{15}$, showing definitions of the free parameters optimized in the refinement as well as a possible atomic decoration. Blue: atoms in flat layers; red: atoms in puckered layers; atoms displaced in the positive $\mathbf{c}$ direction are shown with a 'beachball' pattern; all other atoms in the puckered layers are displaced in the negative $\mathbf{c}$ direction. The proposed chemical decoration of the disordered structural motif is illustrated with small atoms on Al-dominated sites and large atoms on mixed TM/Al sites. For discussion see text. Parameter names and abbreviations are explained in Table 1.

Table 1
Free model parameters, their optimized values and value intervals used for differential evolution optimization.

IPR – inner puckered ring; OPR – outer puckered ring; IFR – inner flat ring; OFR – outer flat ring. For further definitions of the parameters see Fig. 7.

Parameter	Description	Permitted interval	Start interval	Optimized value
$r_{\rm pi}$	Radius of IPR	4.00–5.25 Å	4.50–5.00 Å	4.80 Å
$r_{\rm po}$	Radius of OPR	6.50–7.75 Å	7.00–7.50 Å	7.39 Å
$\Delta z_{\rm pi}$	Vertical out-of-plane shift (puckering amplitude) of IPR	0.082–0.457 Å	0.185–0.411 Å	0.208 Å
$\Delta z_{\rm po}$	Vertical out-of-plane shift (puckering amplitude) of OPR	0.082–0.457 Å	0.185–0.411 Å	0.368 Å
$\alpha_{\rm pi}$	Angular offset of atom positions on IPR, relative to mean positions at 18°, 54°, 90°, ...	−4.00–4.00°	−2.50–2.50°	−1.46°
$\alpha_{\rm po}$	Angular offset of atom positions on OPR, relative to mean positions at 18°, 54°, 90°, ...	−4.00–4.00°	−2.50–2.50°	−0.29°
$r_{\rm fo1}$	Radius of OFR – inward-shifted positions	4.75–6.50 Å	5.00–6.30 Å	5.41 Å
$r_{\rm fo2}$	Radius of OFR – outward-shifted positions	4.75–7.80 Å	5.10–7.30 Å	6.36 Å
$\alpha_{\rm fo1}$	Angular offset of inward-shifted atom positions on OFR, relative to mean positions at 18°, 54°, 90°, ...	0.00–12.00°	0.00–11.00°	9.86°
$\alpha_{\rm fo2}$	Angular offset of outward-shifted atom positions on OFR, relative to mean positions at 18°, 54°, 90°, ...	−12.00–12.00°	−11.00–11.00°	−2.67°
$r_{\rm fi}$	Radius of IFR	3.30–4.50 Å	3.40–4.20 Å	3.87 Å
$\alpha_{\rm fi}$	Angular offset of atom positions on IFR, relative to mean positions at 0°, 72°, 144°, ...	−8.00–8.00°	−7.00–7.00°	−5.29°
a	Exponential decay	0.000–0.237 Å^{-1}	0.012–0.119 Å^{-1}	0.059 Å^{-1}
$o_{\rm po}$	Scattering weighting factor of OPR relative to $o_{\rm fo1}$	0.000–2.500	0.050–2.000	0.712
$o_{\rm fo2}$	Scattering weighting factor of OFR (first fivefold sub-ring, outward-shifted)	0.000–2.500	0.750–1.250	1.259
$o_{\rm fo1}$	Scattering weighting factor of OFR (second fivefold sub-ring, inward-shifted) – fixed to 1	1.000	1.000	–
$o_{\rm pi}$	Scattering weighting factor of IPR relative to $o_{\rm fo1}$	0.000–2.500	0.050–2.000	1.284
$o_{\rm fi}$	Scattering weighting factor of IFR relative to $o_{\rm fo1}$	0.000–2.500	0.050–2.000	1.297

ideal position on the flat plane. To avoid correlations with the scale factor, the scattering weighting factor of one arbitrarily selected site was set to unity (see Table 1). No further constraints apart from the symmetry of the rod group $p\overline{10}2c$ were applied. Including a global scale factor, the model had 18 parameters to be optimized.

The evolutionary optimization of the final model was run with a population size of 150 individuals. The crossover and

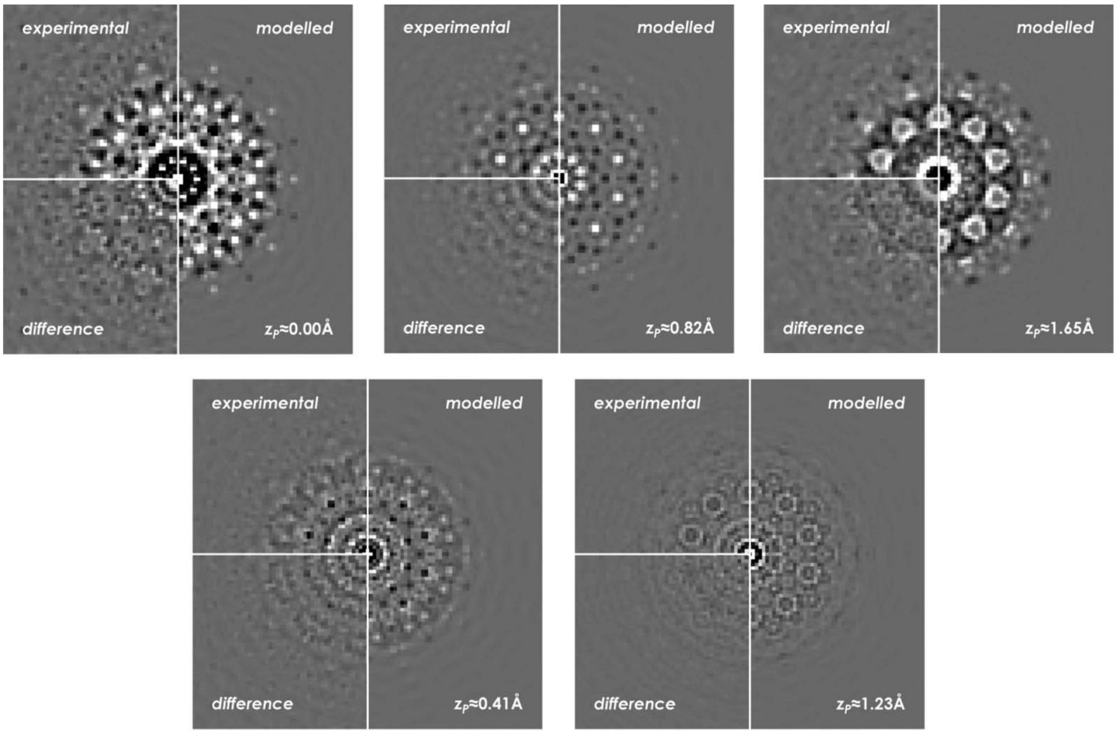

Figure 8
Comparison of the experimental and the optimized modelled 3D-ΔPDF of d-$\rm Al_{65}Cu_{20}Co_{15}$. In the lower-left quadrant of each image, the difference between the experimental and the modelled 3D-ΔPDF is shown. Positive differences ($\Delta{\rm PDF_{exp}} > \Delta{\rm PDF_{model}}$) are white; negative differences ($\Delta{\rm PDF_{exp}} < \Delta{\rm PDF_{model}}$) are black. The area covered by each image is ±21.27 Å along each axis. The colouring scheme of the experimental and modelled ΔPDF is the same as in Fig. 3.

the mutation constant were both set to 0.7 (see Weber & Bürgi, 2002, for definitions). The computations were performed on an Apple Macintosh cluster equipped with 11 1.8 GHz and 20 2.0 GHz CPUs. The best individual was found after about 1400 generations, and the whole population converged to this individual representation after about 2000 generations. The summed total computation time of all processors was about 160 d; this equals a wall time of about 5 d. The optimized parameter values are listed in Table 1. The residual value for the best individual was $R = 0.300$. Good agreements are found between the experimental and modelled ΔPDF and diffuse scattering maps (Figs. 8 and 9). The differences between the experimental and the modelled ΔPDF densities within the volume covered by the model are of the same magnitude as the correlation densities with horizontal lengths >14.5 Å. Hence, the assumption that inter-cluster correlations are significantly weaker than intra-cluster correlations could be confirmed.

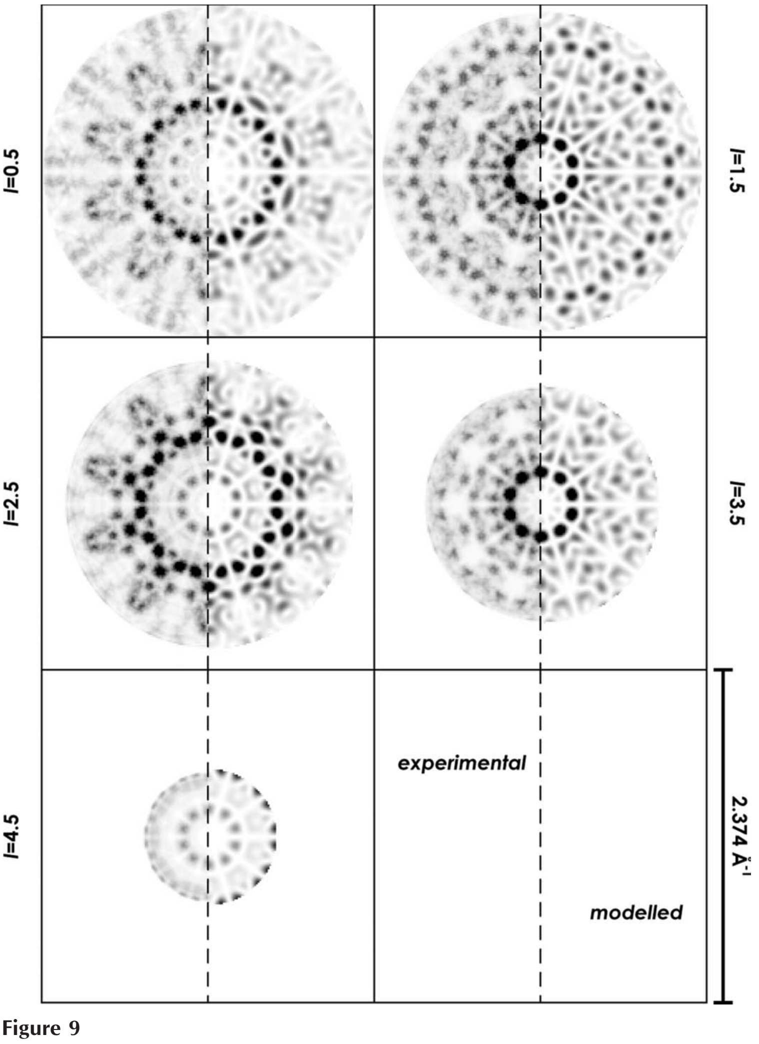

Figure 9
Comparison of experimental and modelled diffuse X-ray scattering intensities in the interlayers of d-$Al_{65}Cu_{20}Co_{15}$.

Compared to conventional average-structure least-squares refinements, the value of R of the final result seems to be rather high. This may be explained by the fact that diffuse-scattering-based refinements in general yield higher R values than Bragg-scattering-based refinements, because of an usually lower quality of the experimental data. The weaker intensity of diffuse scattering is responsible for stronger contributions of statistical errors, and furthermore, demanding data processing procedures favour introduction of systematic errors. For these reasons, diffuse-scattering-based refinements of extended reciprocal space volumes do rarely yield R values below 0.15. Such errors also propagate into the PDF and ΔPDF. Additional problems are specific to quasicrystals. The refined model presented here is in fact a simplified representation of reality. The model assumes the presence of only one prototypic real cluster and one resulting average cluster. As mentioned above, quasicrystals may, however, show a large number of variants even for the average cluster, let alone for the real clusters. Such a simplified model certainly increases the lowest possible R.

The optimized model describes a structural motif that is representative for idealized local disorder in d-Al–Cu–Co. The atomic structure of the final model is shown in Figs. 7 and 10 and Table 1. The prior model of the puckered layers developed from qualitative considerations could be confirmed. The refined values of $r_{\rm pi} = 4.80$ Å and $r_{\rm po} = 7.39$ Å are close to the distances found by Steurer & Kuo (1990) (4.64 and 7.51 Å, respectively; see Fig. 1*a*). The puckering amplitude in the outer ring ($\Delta z_{\rm po} = 0.368$ Å) is larger than that of the inner ring ($\Delta z_{\rm pi} = 0.208$ Å). Both values are comparable to maximum puckering amplitudes found in approximant structures [*e.g.* 0.299 Å in orthorhombic $Al_{13}Co_4$ (Grin *et al.*, 1994*a*), 0.345 Å in monoclinic $Al_{13}Co_4$ (Hudd & Taylor, 1962) and 0.354 Å in $Al_{13}Fe_4$ (Grin *et al.*, 1994*b*)].

Atoms in the ring of split positions in the flat layer (referred to as the outer flat ring henceforward) moved significantly away from the positions shown in Fig. 1(*b*). After refinement, the radii of the two orbits of this ring are no longer the same [5.41 and 6.36 Å, compared to 6.10 Å in the average structure of Steurer & Kuo (1990)], and the cylindrical α coordinate is somewhat different from that in the average model [9.86 and 2.67°, compared to 4.6°). The atoms in the inner flat ring refined to a radius of 3.87 Å (3.93 Å in the average structure) and a deviation from the glide plane of 5.29° (compared to 0.0°), *i.e.* 0.36 Å. The interatomic distances between the disordered atoms are reasonable (Fig. 10). Next neighbouring atoms have a separation of between 2.36 and 2.84 Å, which are typical values for Al–TM compounds. The distances between disordered and ordered atoms lying in the regime of the clusters must be estimated (*cf.* Fig. 1), since the latter were not considered in the model. Most atom positions of the average structure in the environment of the proposed structural motif have reasonable distances to the disordered positions, or, if necessary, slight shifts of the respective atom positions are sufficient to avoid conflicts.

The refined decay parameter a = 0.059 Å^{-1} dampens the model PDF densities to 43% at a radial distance of 14.5 Å, *i.e.* the clusters show a significant amount of internal disorder. The refined scattering weighting factors of the disordered rings follow a downward trend with increasing radius of the atomic rings (see Table 1). As the scattering weighting factors are proportional to the contributions of each ring to the total pair correlations contained in the ΔPDF, one could hope that the refined values would give an indication about the distribution of the elements among the atomic sites. This is, however, not the case, as the refined scattering weighting factors are not only proportional to the scattering power of the elements but may also be correlated with the strength of pair correlations. The exponential attenuation function $t(\mathbf{r}_P)$ is a very simple model for addressing intra-cluster disorder. The decrease of scattering weighting factors with increasing distance from the cluster axis may, for instance, be a consequence of a situation where atoms become more affected by intra-cluster disorder the farther away they are from the cluster axis. This kind of disorder could at least partly be compensated for by attributing a lower scattering power to such atoms. It is also expected that the scattering weighting factors compensate for other shortcomings of the model. These uncertainties could only be resolved if the average structure were precisely known, in order to allow application of reliable constraints to the atomic occupation factors.

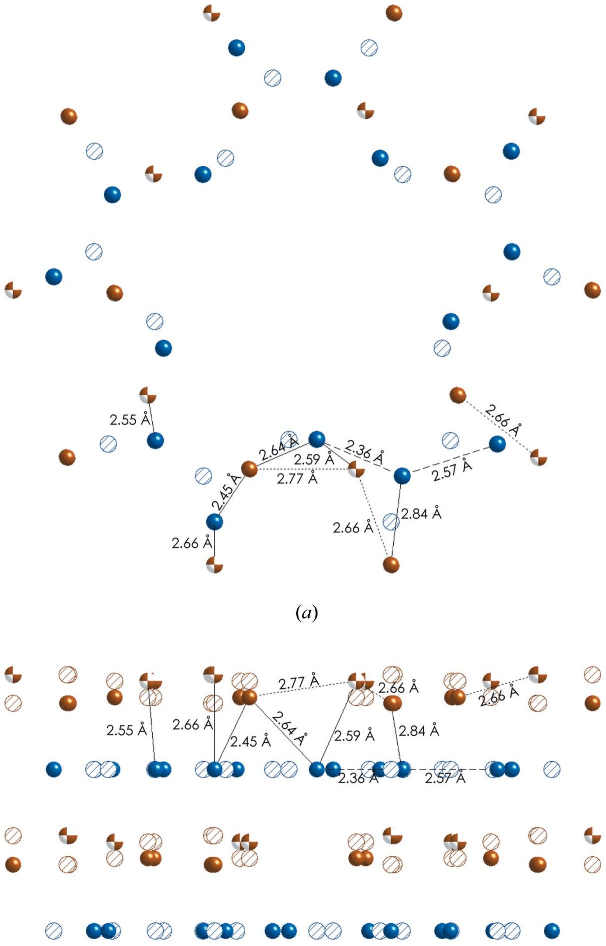

Figure 10
The optimized ~8 Å real-structure motif and the average structure resulting from superposition of two disordered motifs shifted by ~4 Å along **c**. The colours of the atoms are the same as in Fig. 7. Locally existing atoms of one real-structure representation of the disordered motif are shown as rendered balls; locally vacant atom sites of the average structure are shown as striped circles. For the ~4 Å-shifted real-structure motif, the rendered/striped representations would be inverse. Interatomic distances in the disordered structural motif shorter than 3 Å are labelled. Dashed lines: intralayer distances in flat layers; dotted lines: intralayer distances in puckered layers; solid lines: interlayer distances. (*a*) Projection parallel to **c**. In the topmost puckered layer, the locally vacant atoms sites are not shown, in order not to hide the downwards-shifted occupied ones. (*b*) View perpendicular to **c** onto an ~8 Å unit of the same cluster as shown in (*a*).

As the refined scattering weighting factors cannot be directly used to determine the distribution of the elements, analysis of interatomic distances may give a more precise picture. Based on the experience that the smallest Al—Al distances are typically 0.2–0.3 Å longer than the smallest Al—TM or TM—TM distances, it may be assumed that the outer puckered ring and the inward-shifted positions of the outer flat ring are preferably occupied by Al and the others by TMs (Fig. 7). The shortest Al—Al distance of this model would be 2.84 Å, and the composition of this motif is Al_3TM_4, provided that there is a strict separation into Al and TM sites. However, the interatomic distances allow facilely inserting more Al into the hitherto pure TM sites. Also by comparison to average structure models from the literature (see below, as well as Fig. 11) a wide scope of mixed occupations is found. Thus, the composition of the disordered motif may be close to the average bulk composition $Al_{6.5}TM_{3.5}$. Although of limited decisive power, the refined scattering power factors fit well to this proposed decoration, as the factors of the two Al-dominated rings are clearly smaller than those of the TM-dominated ones.

The presented structural motif is chiral. By applying an inversion transformation, a second enantiomorphic representation of the structural motif can be obtained. The two ΔPDFs are identical. Hence, from ΔPDF analysis, as well as from the uncertain average structure solution, it cannot be determined how the two chiral forms of the motif are distributed in the real quasicrystal structure.

The structural models of *d*-Al–Cu–Co published so far do not consider the ~8 Å superstructure, but only the ~4 Å average structure. It is beyond the scope of this study to reinterpret the structure and structural models of *d*-Al–Cu–Co. The presented structural motif covers only a part of the complete structure, thus neither is it congruent with the structural clusters found in the literature nor has it the character of a structural tile. However, its average representation can be localized in other atomic structures, as was exemplarily shown in the structure solution of Steurer & Kuo (1990). A localization of the disordered structural motif in the super-cluster of Deloudi (2008) is shown in Fig. 11. This model, which is based on experimental data, is the most recent description available of the *d*-Al–Cu–Co structure. The model of disorder proposed here is consistent with the average-structure model of Deloudi (2008). However, it becomes obvious that there are a wide range of variations in decorating the atom positions with the elements.

4. Summary and conclusions

The 3D-ΔPDF method was shown to be a powerful tool for understanding disorder in complex structures. Unlike reciprocal space, PDF space is isometric to real space, *i.e.* PDF densities may be directly linked to structural features. This allows a direct interpretation of interatomic correlations and selective modelling of structural features. The power of the ΔPDF approach was clearly demonstrated on the example of analysing puckering in clusters of *d*-$Al_{65}Cu_{20}Co_{15}$. The possibility of selective modelling in PDF space allowed a straightforward development of a puckered layer model without including any knowledge about the flat layers. By employing this special feature of PDF modelling, the complexity of modelling could be reduced significantly. After the model for the puckered layers was identified, parts of the ΔPDF that were not covered by the model could be clearly recognized and addressed in the next steps. This finally resulted in a satisfying model taking into account flat and puckered layers. In reciprocal space, on the other hand, the agreement between experimental diffuse scattering and intensities calculated from the first intermediate model was too poor (Fig. 6) to allow differentiation between well fitting, partially fitting and missing features of the intermediate model. In particular, in the case of quasicrystals, it is advantageous to accomplish modelling of local disorder independently of the long-range-ordered properties of clusters. In the present case, it was not even necessary to know about the existence of an underlying quasiperiodic lattice when modelling the atomic structure of the clusters.

A prerequisite for using the ΔPDF approach is that the average structure must be known. A precise knowledge helps to explain the ΔPDF map as it provides useful constraints for the real structure. In the case of unreliable average structure models, as in the case of the present study, the ΔPDF method may still be applied, but shortcomings in the analysis of Bragg scattering will also limit the information attainable through the ΔPDF method.

Optimizing the ΔPDF model with the differential evolution method is a practicable method for fitting a disorder model to the experimental ΔPDF. In the process of model optimization, only constraints on the symmetry and geometry of the cluster were applied that were directly obtained from analysis of the average structure, the diffraction pattern and the PDF. There were no physical constraints, such as optimizing bond lengths or free-energy minimization. Though successful in finding a satisfying solution, differential evolution turned out to be a slow optimization method, since it covers a large volume in parameter space to search for the best solution and therefore requires many recalculations of the model. Further, it is difficult to derive estimated standard deviations of refined parameters when using this method (Weber *et al.*, 2008). A promising alternative may be least-squares refinements, whose potential for optimizing 3D-PDF models will be examined in future applications.

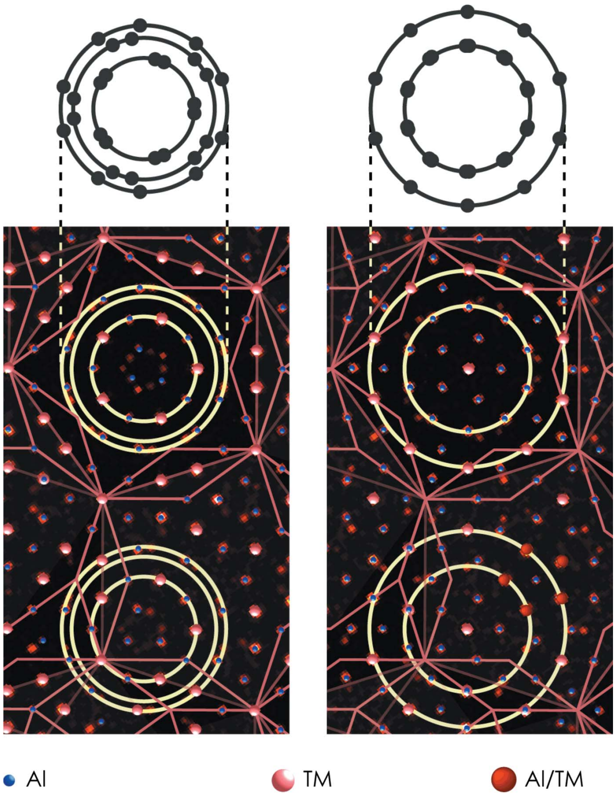

Figure 11
The disordered structural motif embedded in the *d*-Al–Cu–Co super-cluster reported by Deloudi (2008). Borders of decagonal clusters (red lines) and the atom decoration are shown as proposed by Deloudi (2008). Sections of the two layers of the ~4 Å structure are shown. Yellow circles mark possible locations of the disordered structural motif. The left image features flat rings of the structural motif, whereas the right one shows the puckered rings perpendicularly beneath or above. For comparison, the atom positions of the averaged disordered structural motif are shown at the top. The disordered motif may occur at the centres of single clusters of Deloudi's model, as well as at intersections of clusters. In the background, electron density maps after Steurer & Kuo (1990) are shown. The vertical edge length of each image is about 38.2 Å.

The present study of disorder in *d*-$Al_{65}Cu_{20}Co_{15}$ is the first quantitative refinement of superstructure disorder in quasicrystals using an atomic model. The refined model is consistent with the experimental diffraction pattern, it is reasonable from a chemical point of view, and in major parts it is compatible with structure motifs previously described in *d*-Al–Cu–Co or closely related quasicrystal or approximant structures. Different to most other models is the arrangement of the atom sites on the outer ring in the flat layer. However, inconsistencies in the structures proposed in the literature do not allow a clear decision about the reliability of this structural feature. Open questions include the distribution of the elements among atomic sites, details about intra-cluster disorder and the positions of ordered atoms within the regime of a cluster. All these uncertainties could most probably be resolved if the average structure were known more precisely. It may further be argued that the rod-group symmetry of the real cluster might be lower than $p\overline{10}2c$. This was not tested, because modelling would have become far more complicated as a result of the increasing number of parameters and because of the many time-consuming trial-and-error cycles required for finding the symmetry element of the real cluster to be dropped. Further, there are no indications for lower rod-group symmetry apart from very weak violations of the diffuse *c*-glide plane extinction rules. Despite some shortcomings of the model, major aspects of the real structure, such as the atomic model of puckered layers, the identification and size of the disordered cluster, as well as spatial correlation between clusters, could, however, be determined reliably. The results therefore provide a solid basis for a deeper understanding of order and disorder in *d*-Al–Cu–Co and closely related compounds.

The intention of this paper was to prove the principles of 3D-PDF modelling techniques. It mainly addressed experimental and theoretical aspects that are specific to the problems tackled in this work. More general discussions will be given in future contributions. A computer program that allows 3D-PDF and 3D-ΔPDF refinements in a broader context is currently under development.

The authors thank the Swiss National Science Foundation for financial support (project Nos. 200020-105158 and 200020-113291).

References

Billinge, S. J. L. (2008). *J. Solid State Chem.* **181**, 1695–1700.

Black, P. J. (1955*a*). *Acta Cryst.* **8**, 43–48.

Black, P. J. (1955*b*). *Acta Cryst.* **8**, 175–182.

Brühne, S., Sterzel, R., Uhrig, E., Gross, C. & Assmus, W. (2004). *Z. Kristallogr.* **219**, 245–258.

Brühne, S., Uhrig, E., Gross, C. & Assmus, W. (2003). *Cryst. Res. Technol.* **38**, 1023–1036.

Brühne, S., Uhrig, E., Gross, C., Assmus, W., Masadeh, A. S. & Billinge, S. J. L. (2005). *J. Phys. Condens. Matter*, **17**, 1561–1572.

Brühne, S., Uhrig, E., Kreiner, G. & Assmus, W. (2006). *Philos. Mag.* **86**, 463–468.

Brühne, S., Uhrig, E., Luther, K. D., Assmus, W., Brunelli, M., Masadeh, A. S. & Billinge, S. J. L. (2005). *Z. Kristallogr.* **220**, 962–967.

Bürgi, H. B., Hostettler, M., Birkedal, H. & Schwarzenbach, D. (2005). *Z. Kristallogr.* **220**, 1066–1075.

Cervellino, A., Haibach, T. & Steurer, W. (2002). *Acta Cryst.* B**58**, 8–33.

Cowley, J. M. (1995). *Diffraction Physics*, 3rd revised ed. Amsterdam: Elsevier.

De Boissieu, M. (2008). *Philos. Mag.* **88**, 2295–2309.

Deloudi, S. (2008). PhD thesis, ETH Zürich, Switzerland.

Dubois, J. M. & Janot, C. (1988). *Europhys. Lett.* **5**, 235–240.

Egami, T. & Billinge, S. J. L. (2003). *Underneath the Bragg Peaks: Structural Analysis of Complex Materials.* New York: Pergamon.

Estermann, M. A. & Steurer, W. (1998). *Phase Transitions*, **67**, 165–195.

Fleischer, F., Weber, T., Jung, D. Y. & Steurer, W. (2010). *J. Alloys Compd.* **500**, 153–160.

Frey, F. (2003). *Lect. Notes Phys.* **610**, 133–166.

Frey, F. & Steurer, W. (1993). *J. Non-Cryst. Solids*, **153**, 600–605.

Frey, F., Weidner, E., Hradil, K., De Boissieu, M., Currat, R., Shibata, K., Tsai, A. P. & Sato, T. J. (2000). *Philos. Mag. A*, **80**, 2375–2391.

Frey, F., Weidner, E., Hradil, K., de Boissieu, M., Letoublon, A., McIntyre, G., Currat, R. & Tsai, A. P. (2002). *J. Alloys Compd.* **342**, 57–64.

Frigo, M. & Johnson, S. G. (2005). *Proc. IEEE*, **93**, 216–231.

Grin, J., Burkhardt, U., Ellner, M. & Peters, K. (1994*a*). *J. Alloys Compd.* **206**, 243–247.

Grin, J., Burkhardt, U., Ellner, M. & Peters, K. (1994*b*). *Z. Kristallogr.* **209**, 479–487.

He, L. X., Zhang, Z., Wu, Y. K. & Kuo, K. H. (1988). *Inst. Phys. Conf. Ser.* **93**, 501–502.

He, Y., Hu, R. Z., Egami, T., Poon, S. J. & Shiflet, G. J. (1993). *Phys. Rev. Lett.* **70**, 2411–2414.

Hu, R. Z., Egami, T., Tsai, A. P., Inoue, A. & Masumoto, T. (1992). *Phys. Rev. B Condens. Matter*, **46**, 6105–6114.

Hudd, R. C. & Taylor, W. H. (1962). *Acta Cryst.* **15**, 441–442.

Kabsch, W. (1993). *J. Appl. Cryst.* **26**, 795–800.

Katrych, S. & Steurer, W. (2004). *Z. Kristallogr.* **219**, 606–613.

Kobas, M., Weber, T. & Steurer, W. (2004). *Ferroelectrics*, **305**, 185–188.

Kobas, M., Weber, T. & Steurer, W. (2005*a*). *Phys. Rev. B Condens. Matter*, **71**, 224205.

Kobas, M., Weber, T. & Steurer, W. (2005*b*). *Phys. Rev. B Condens. Matter*, **71**, 224206.

Neder, R. B. & Korsunskiy, V. I. (2005). *J. Phys. Condens. Matter*, **17**, S125–S134.

Proffen, T., Billinge, S. J. L., Egami, T. & Louca, D. (2003). *Z. Kristallogr.* **218**, 132–143.

Proffen, T. & Kim, H. (2009). *J. Mater. Chem.* **19**, 5078–5088.

Qiu, X., Božin, E. S., Juhas, P., Proffen, T. & Billinge, S. J. L. (2004). *J. Appl. Cryst.* **37**, 110–116.

Saitoh, K., Tsuda, K., Tanara, M., Tsai, A. P., Inoue, A. & Masumoto, T. (1996). *Philos. Mag. A*, **73**, 387–398.

Schaub, P., Weber, T. & Steurer, W. (2007). *Philos. Mag.* **87**, 2781–2787.

Scholpp, T. (2001). PhD thesis, ETH Zürich, Switzerland.

Steurer, W. (2004). *Z. Kristallogr.* **219**, 391–446.

Steurer, W., Cervellino, A., Lemster, K., Ortelli, S. & Estermann, M. A. (2001). *Chimia*, **55**, 528–533.

Steurer, W. & Deloudi, S. (2009). *Crystallography of Quasicrystals: Concepts, Methods and Structures.* Berlin: Springer.

Steurer, W. & Frey, F. (1998). *Phase Transitions*, **67**, 319–361.

Steurer, W. & Kuo, K. H. (1990). *Acta Cryst.* B**46**, 703–712.

Storn, R. & Price, K. (1997). *J. Glob. Optim.* **11**, 341–359.

Toby, B. H. & Egami, T. (1992). *Acta Cryst.* A**48**, 336–346.

Weber, T. & Bürgi, H.-B. (2002). *Acta Cryst.* A**58**, 526–540.

Weber, T., Estermann, M. A. & Bürgi, H.-B. (2001). *Acta Cryst.* B**57**, 579–590.

Weber, T., Kobas, M. & Steurer, W. (2004). *Ferroelectrics*, **305**, 213–216.

Weber, T., Kobas, M. & Steurer, W. (2007). *Philos. Mag.* **87**, 2799–2805.

Weber, T., Simon, A., Mattausch, H., Kienle, L. & Oeckler, O. (2008). *Acta Cryst.* A**64**, 641–653.

Weber, T. & Steurer, W. (2009). *Diffuse Scattering and the Fundamental Properties of Materials*, edited by R. I. Barabash, G. E. Ice & P. E. A. Turchi, pp. 239–258. New York: Momentum.

Welberry, T. R. (2004). *Diffuse X-ray Scattering and Models of Disorder.* Oxford University Press.

Welberry, T. R. & Butler, B. D. (1995). *Chem. Rev.* **95**, 2369–2403.

Appendix 4.A: Decagonal rod groups

Decagonal rod groups were used to characterise the columnar building units of the average and real structure of *d*-Al–Cu–Co in section 4.3.5. However, decagonal rod groups have not been published as yet. The decagonal groups and their symbols herein used before were deduced in analogy to the system of rod groups of periodic symmetries in *International Tables for Crystallography, Vol. E* (Kopský & Litvin, 2010). Fig. 4.12 shows the symmetry elements of the mentioned two decagonal rod groups. Group $\mathscr{p}\overline{10}2m$, identified in the average structure of *d*-Al–Cu–Co, is a supergroup of $\mathscr{p}\overline{10}2c$, which characterises the structural motifs in the real structure: averaging of $\mathscr{p}\overline{10}2c$ symmetry with itself shifted by half of its period along the rod axis yields $\mathscr{p}\overline{10}2m$ symmetry.

Appendix 4.B: Burkov's model

In section 4.3.6 possibilities of localisation of the identified disordered structural motif within the average-structure supercluster of Deloudi (2008) were demonstrated (*cf.* Fig. 4.11). In addition, a comparison to the average-structure model of Burkov (1993) is presented here (Fig. 4.13). Burkov's model was the first atomic structural model published for *d*-Al–Cu–Co. It is a theoretical structure model and was developed without backing by experimental data. The disordered structural motif could be localised in Burkov's average structure model. It can be seen from Fig. 4.13 that, in contrast to the structures of Steurer & Kuo (1990) and Deloudi (2008), the variation of the radial distance in the outer flat ring of the disordered structural motif is covered by Burkov's model, even though the match of positions is not exact for some single atom positions.

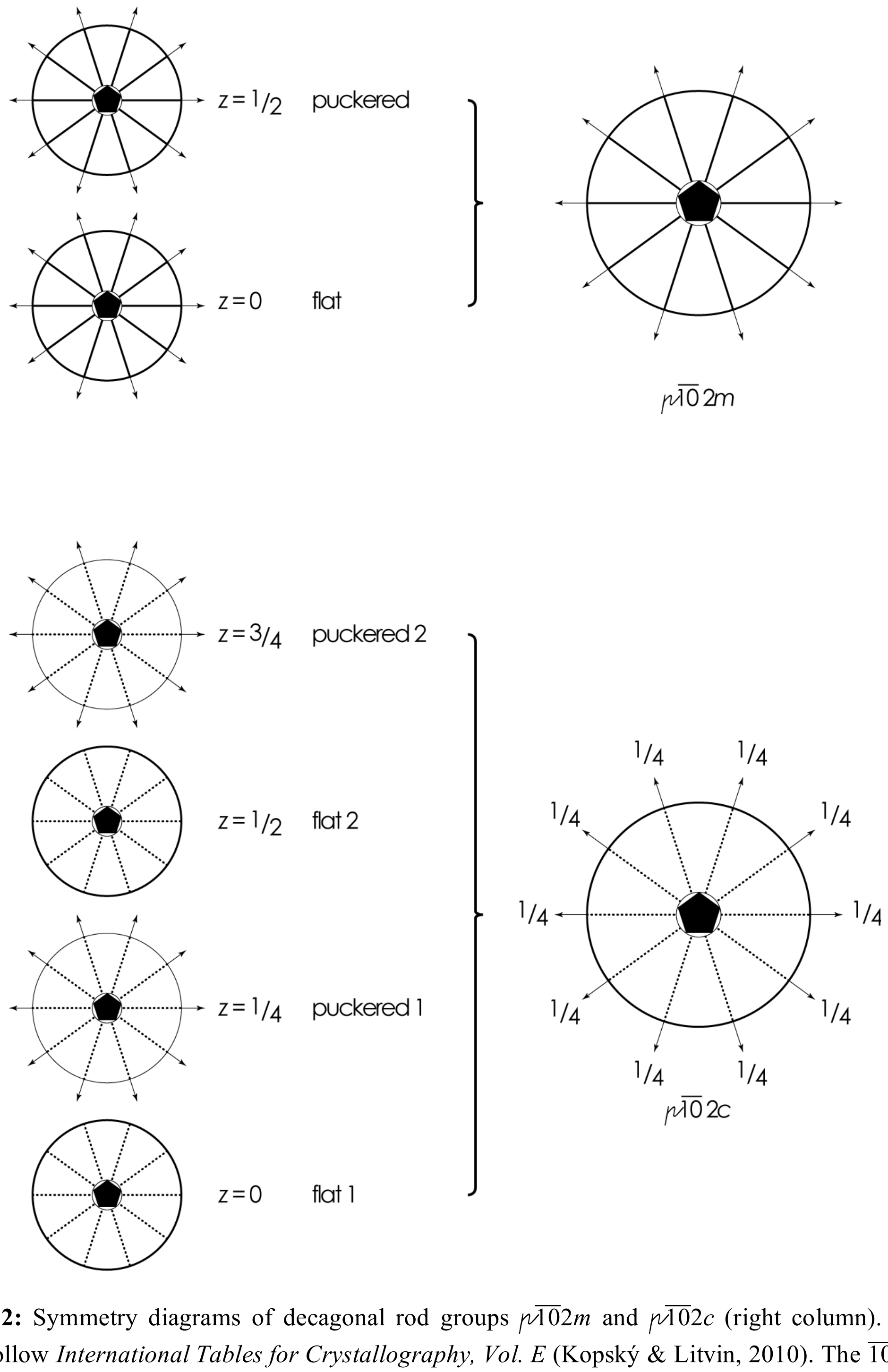

Figure 4.12: Symmetry diagrams of decagonal rod groups $p\overline{10}2m$ and $p\overline{10}2c$ (right column). Graphical symbols follow *International Tables for Crystallography, Vol. E* (Kopský & Litvin, 2010). The $\overline{10}$ inversion axis is in the centre of each diagram. Thick solid lines: mirror planes; dotted lines: glide planes with glide vectors of half-length of the lattice vector parallel to the projection plane; arrows: twofold rotation axes parallel to the plane. Small fractions indicate the height (as fractions z of the translation vector along the projection axis) of the rotation axes above the plane of the diagram, unless the value is zero. In the left column the local symmetry elements in the flat and puckered layers of the disordered structural motif of *d*-Al–Cu–Co are shown, *i.e.* two different layer types in the ~4 Å average structure ($p\overline{10}2m$), and four different layer types in the ~8 Å local structure ($p\overline{10}2c$). In the $p\overline{10}2c$ structure the two flat and the two puckered layers are symmetry equivalent each to another.

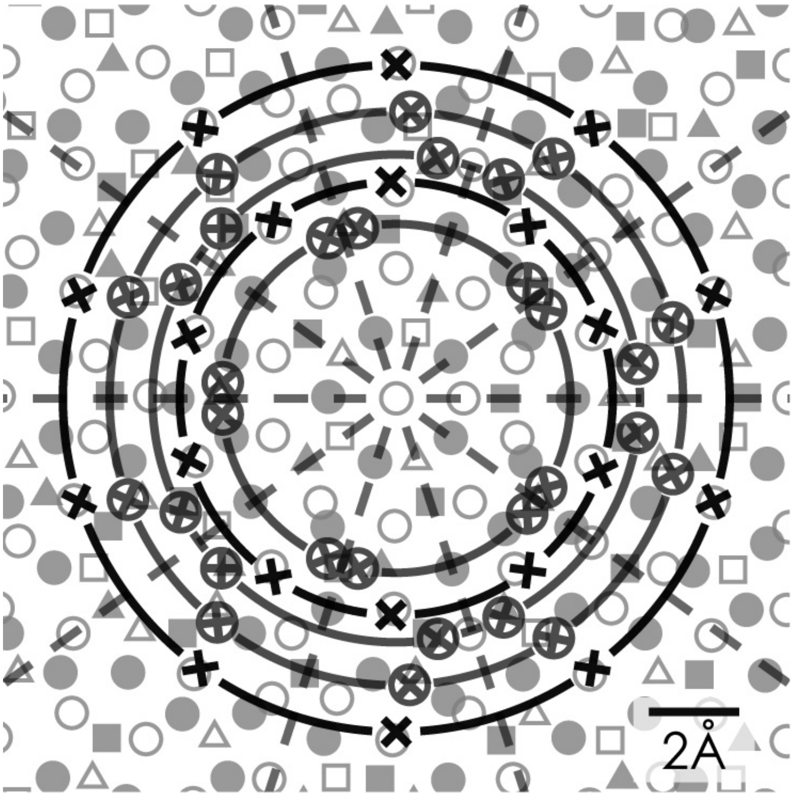

Figure 4.13: The disordered structural motif localised in the tiling of the structural model (grey background) by Burkov (1993) in projection along **c**. Empty symbols mark atoms at $z = 0$, full ones at $z = 0.5$ in respect to the ~4 Å structure. ○: Al, △: Cu, □: Co. Black and dark grey circles mark the puckered and flat rings of the superposed disordered structural motif, respectively. Positions of the atoms of the disordered structural motif are marked by crosses (puckered layers) and crossed circles (flat layers). Note that atom positions of the averaged motif are shown that cannot be occupied all at the same time. Straight dashed grey lines indicate mirror symmetry of the averaged disordered structural motif, which is partially fulfilled in Burkov's model.

5. Practical Aspects of 3D-PDF and 3D-ΔPDF Analysis

5. PRACTICAL ASPECTS OF 3D-PDF AND 3D-ΔPDF ANALYSIS

When incoherent and multiple scattering contributions are ignored, the observed scattering intensity I_{obs} of a diffraction experiment can be expressed as

$$I_{obs}(\mathbf{h}) = \left\{ \left[\left(I_{Bragg}(\mathbf{h}) + I_{diffuse}(\mathbf{h}) \right) \otimes r_s(\mathbf{h}) \right] + I_{Backgr}(\mathbf{h}) \right\} d(\mathbf{h}), \tag{5.1}$$

wherein $r_s(\mathbf{h})$ is the reciprocal space resolution function and $d(\mathbf{h})$ the envelope function of the reciprocal space volume covered by the experiment (for a definition see section 4.2.3). Convolution with an invariant function $r_s(\mathbf{h})$ is a strong simplification in the above expression, as $r_s(\mathbf{h})$ can vary notably within a measured diffraction pattern. The PDF calculated by Fourier Transform of I_{obs} is

$$P_{obs}(\mathbf{r}) = \left\{ \left[\left(P_{hkl}(\mathbf{r}) + \Delta P(\mathbf{r}) \right) R_s(\mathbf{r}) \right] + \mathrm{FT}\left(I_{Backgr}(\mathbf{r}) \right) \right\} \otimes D(\mathbf{r}). \tag{5.2}$$

$R_s(\mathbf{h})$ and $D(\mathbf{h})$ are the respective Fourier transforms of $r_s(\mathbf{h})$ and $d(\mathbf{h})$. These factors, as well as the background intensities $I_{Backgr}(\mathbf{h})$ have a notable influence on data quality of P_{obs}.

In this chapter, some practical aspects of 3D-PDF, and particularly 3D-ΔPDF analysis are outlined, in order to put the idea of the capabilities and requirements of these methods across. These issues may vary by the problem examined case by case. Practical implementations are exemplified on *N,N′,N″*-tris-*t*-butyl-1,3,5-benzene tricarboxamide and *d*-Al–Cu–Co, which were discussed in chapters 3 and 4.

5.1. Experimental impacts

Due to several experimental factors, such as beam incoherence, divergence or bandwidth of its wavelength, the finite size or the mosaicity of the sample, the point spread function of the detector, just to mention a few, scattering intensities are broadened by an experimental reciprocal resolution function $r_s(\mathbf{h})$. These factors are not specific to PDF investigations, but are a common challenge in diffraction experiments. A detailed discussion of the influence of the resolution function and the detector envelope function on the PDF was given in section 4.2.3. For a real-world application on *d*-Al–Cu–Co see section 4.3.4.

5.2. Data quality enhancement

Experimental single crystal scattering data sets, reconstructed into undistorted reciprocal space coordinates, typically form an irregularly shaped data volume of voxels containing scattering intensities. The shape of this data volume, $d(\mathbf{h})$, depends on the type of detector used, the oscillation range covered by the experiment, beam stop shadows, etc. These factors all effect spurious and complex termination ripples in a 3D-PDF or 3D-ΔPDF when the data is Fourier transformed. This effect can be minimised by using a data set with preferably homogeneously shaped $d(\mathbf{h})$, spanning to large diffraction angles, as it is also practised in measurements for powder PDF analyses. Experimental setup and realisation should be designed to comply with these conditions.

Additionally, by suitable data processing, the data quality can be significantly enhanced. In the process of symmetry equivalent averaging, data are averaged with all of their experimentally available symmetry equivalent orientations given by the crystal's Laue group. The envelope of reciprocal space covered by the experiment becomes larger that way, and voids become filled. The signal-to-noise ratio is improved where multiple data points overlap (see Fig. 5.1). The symmetry equivalent averaged diffraction patterns of *N,N',N''*-tris-*t*-butyl-1,3,5-benzene tricarboxamide and *d*-Al–Cu–Co are shown in Figs. 5.2 and 5.3.

A further factor disturbing the primary data is static background intensities, originating *e.g.* from air scattering and experimental equipment extending into the beam. A discussion of the treatment of background intensities in 1D powder based PDF analysis is found in Toby & Egami (1992). In case of Bragg scattering based single-crystal investigations, the influence of background noise is usually easy to estimate or to correct for, as Bragg peaks are narrow and sparsely distributed, and thus interpolation of background noise is straightforward. However, diffuse scattering intensities are continuous and may be in the same order of magnitude as the background signal, and thus a careful treatment of background intensities is necessary.

If, for simplicity, a uniformly flat or a broad Gaussian-like humped background signal is assumed in reciprocal space (*i.e.* no "powder ring"-like features originating from the sample environment or similar are present), this leads to an addition of a Dirac δ-function or a narrow Gaussian-like peak in the origin of PDF space. However, due to the clipping of $I_{Backgr}(\mathbf{h})$ by $d(\mathbf{h})$ this narrow peak may be accompanied by strong truncation ripples. Exclusion of the background signal is therefore beneficial.

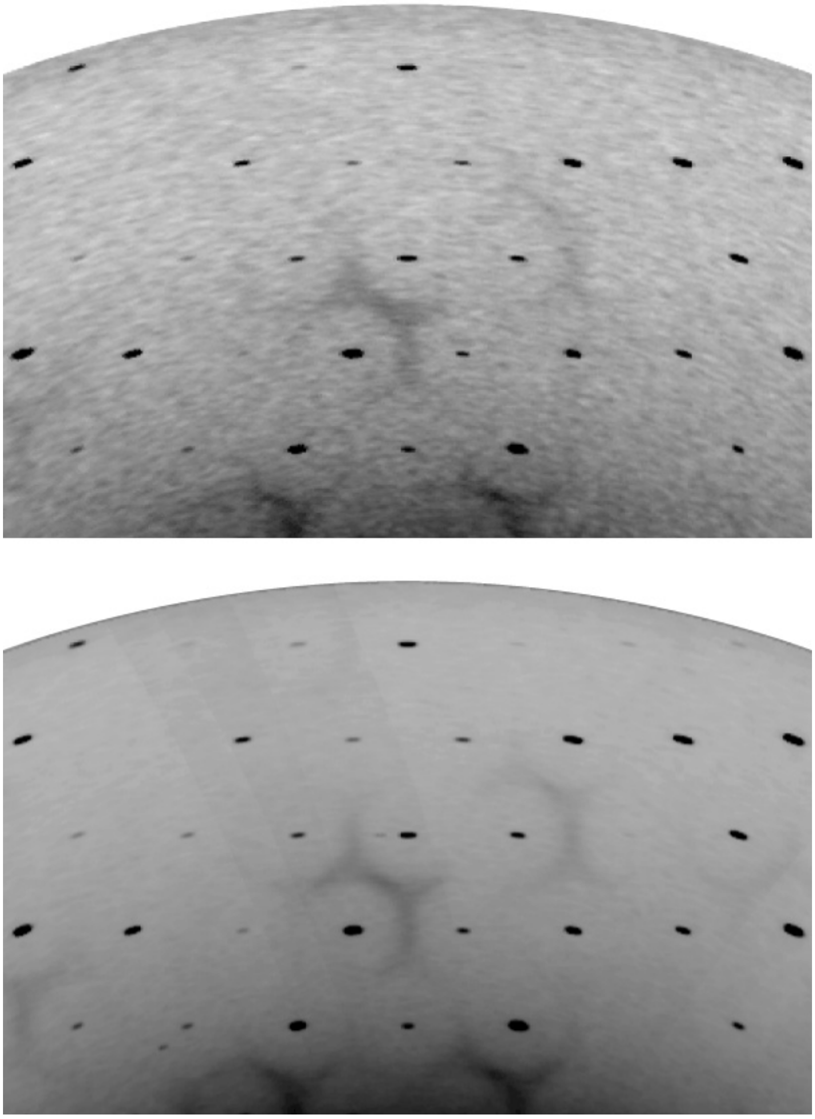

Figure 5.1: Comparison of an enlarged section of the *hk*1-layer of *N,N',N''*-tris-*t*-butyl-1,3,5-benzene tricarboxamide before (top) and after symmetry equivalent averaging (bottom; cf. Fig. 5.2). Note the improved signal to noise ratio achieved by averaging. The size of each image is 0.6 × 0.4 Å.

Background intensities can be estimated from a reference measurement without a sample, or, more favourable, directly from regions in the scattering pattern, where no scattering intensities, Bragg or diffuse, occur. The possibility and plainness of removing static background noise depends on the complexity of diffuse scattering, thus. In patterns that show merely clear and narrow domains of diffuse scattering in one or two dimensions, such as streaks or planes, it is fairly effectual to reconstruct background intensities by interpolation over ranges where they are hidden by structural scattering. These background intensities can be easily subtracted from the experimental data. In case of complex 3D networks of diffuse scattering, more intricate models of background intensities have to be set up.

Removal of background intensities always involves the risk that along with the effective static background noise also parts of the unstructured monotonic scattering intensities (see section 2.1.3) are subtracted. Fortunately this procedure has no serious impact on subsequent PDF analysis, as these intensities just incorporate information on random disorder, but no information about correlated disorder. Diffuse scattering intensities can be interpreted as a Fourier series (*cf.* section 2.1.3). By removal of monotonic contributions from the total diffuse intensities, a certain number of non-interfering Fourier coefficients is subtracted from the summation, but the remaining term still comprises all information about non-random pair correlations. As a consequence of unintended removal of unstructured broad scattering components, the resulting PDF shows a difference in and very close to its origin, but there is no strong implication on the distribution of distant correlation densities. Accordingly, this effect has to be considered in case the PDF density of the origin peak is quantitatively evaluated. All the same, the interpretation of a PDF does not permit doubtlessly recognising random disorder, irrespective whether monotonic scattering intensities were subtracted along with the background or not. However, presence of random disorder can be deduced from atomic displacement parameters in the average structure, provided that an average structure solution of sufficient accuracy is available.

In both investigated datasets, *N,N',N''*-tris-*t*-butyl-1,3,5-benzene tricarboxamide and *d*-Al–Cu–Co, diffuse scattering intensities were restricted to sharp layers perpendicular to the **c*** axis. Background intensities underneath the diffuse intensities were therefore determined by interpolation from intensities slightly above and below these layers (see sections 3.4 and 4.3.3). For that reason, layers containing background intensities were reconstructed likewise the diffraction layers in all possible symmetry equivalent orientations. In case of the tricarboxamide the offset was ±0.007 Å, and ±0.022 $Å^{-1}$ in case of *d*-Al–Cu–Co. Subsequently the layers were averaged, and the background intensities between two adjacent layers were interpolated and subtracted from the measured scattering intensities. The background corrected scattering intensities are shown in Figs. 5.2 and 5.3.

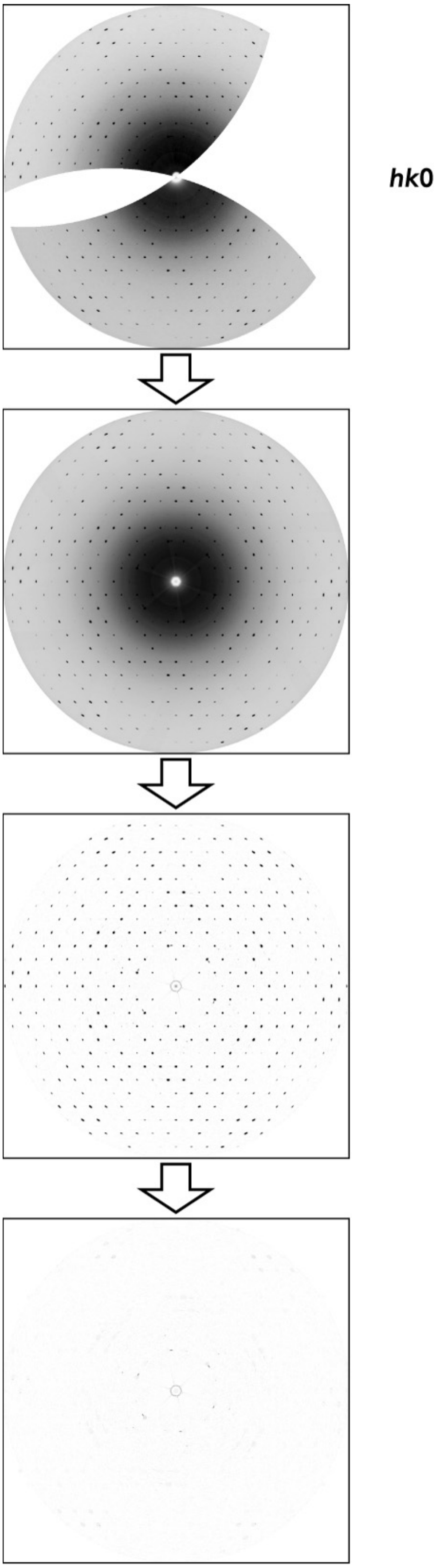

Figure 5.2 (pp. 60-63): Steps of data processing of the experimental single-crystal X-ray diffraction pattern of *N,N',N''*-tris-*t*-butyl-1,3,5-benzene tricarboxamide. Diffraction layers *hkl* with $l = 0$ to 6 are shown. From top to bottom: reconstructed diffraction pattern — after symmetry equivalent averaging — after removal of static background intensities — after elimination of Bragg peaks via a *"punch-and-fill"* filter. The edges of each box cover a range of ±0.91 Å^{-1}. To increase the visibility of weak diffuse scattering, the intensities of the images with $l \geq 4$ were scaled by factor 2.

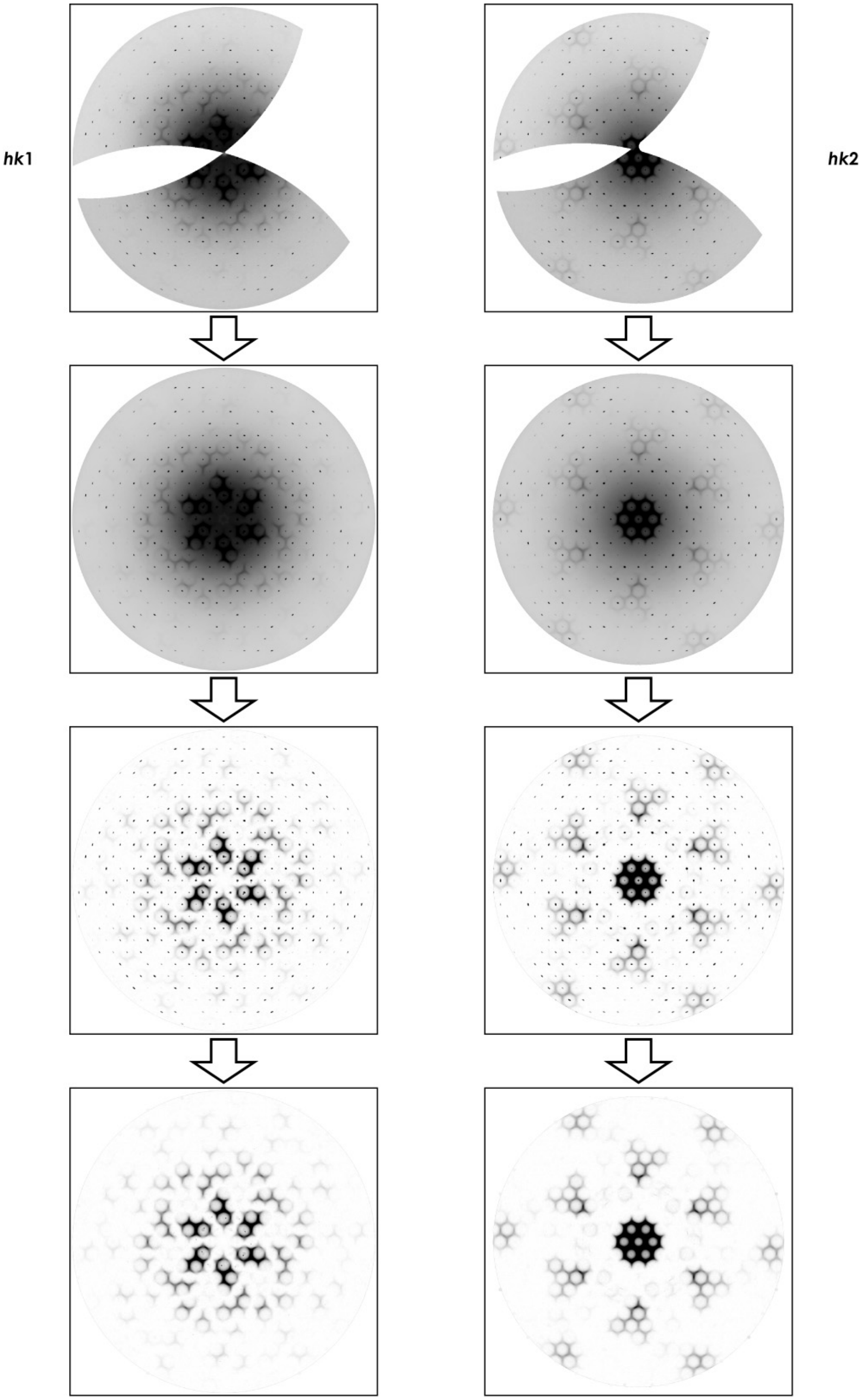
*hk*1
*hk*2

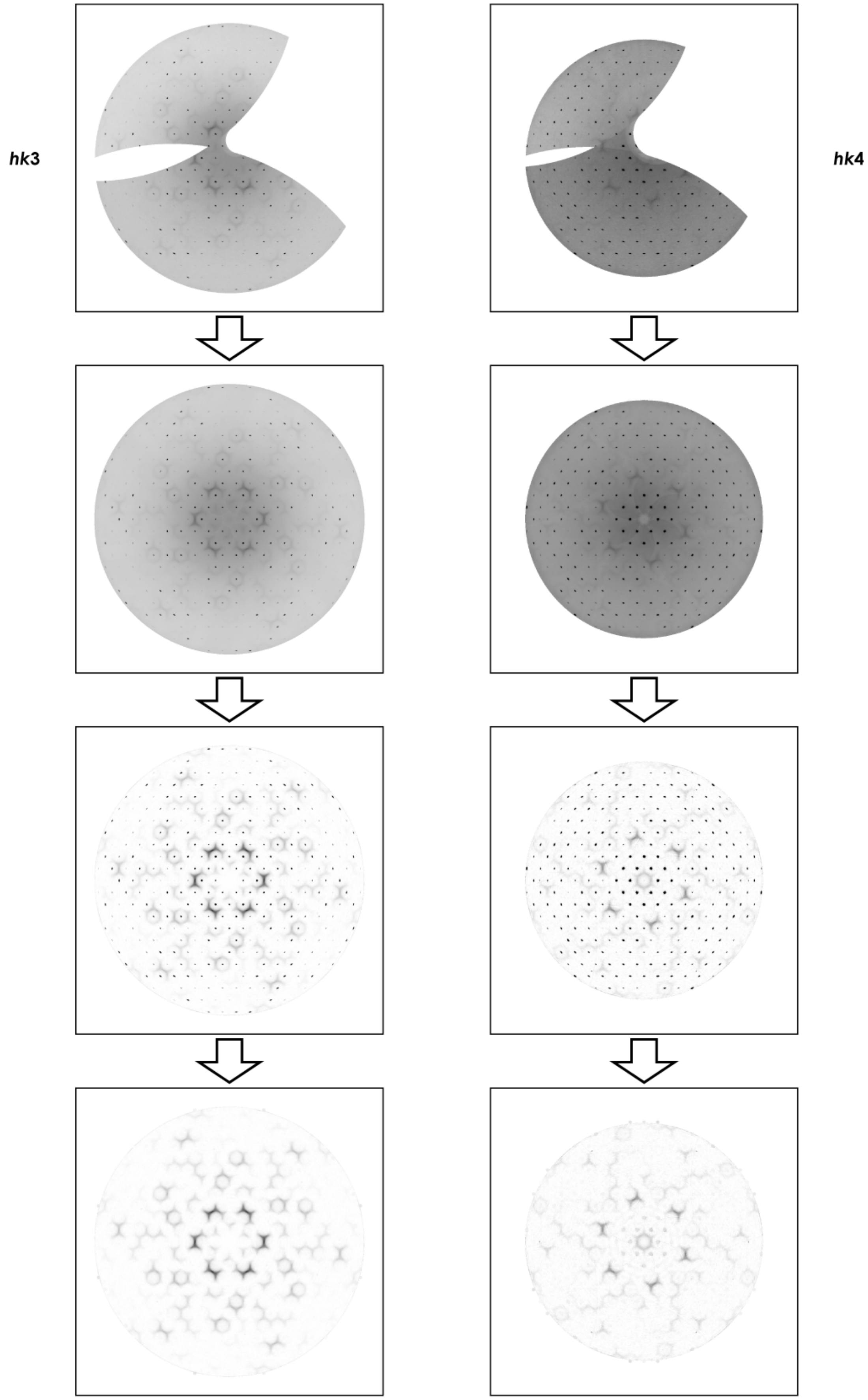
hk3
hk4

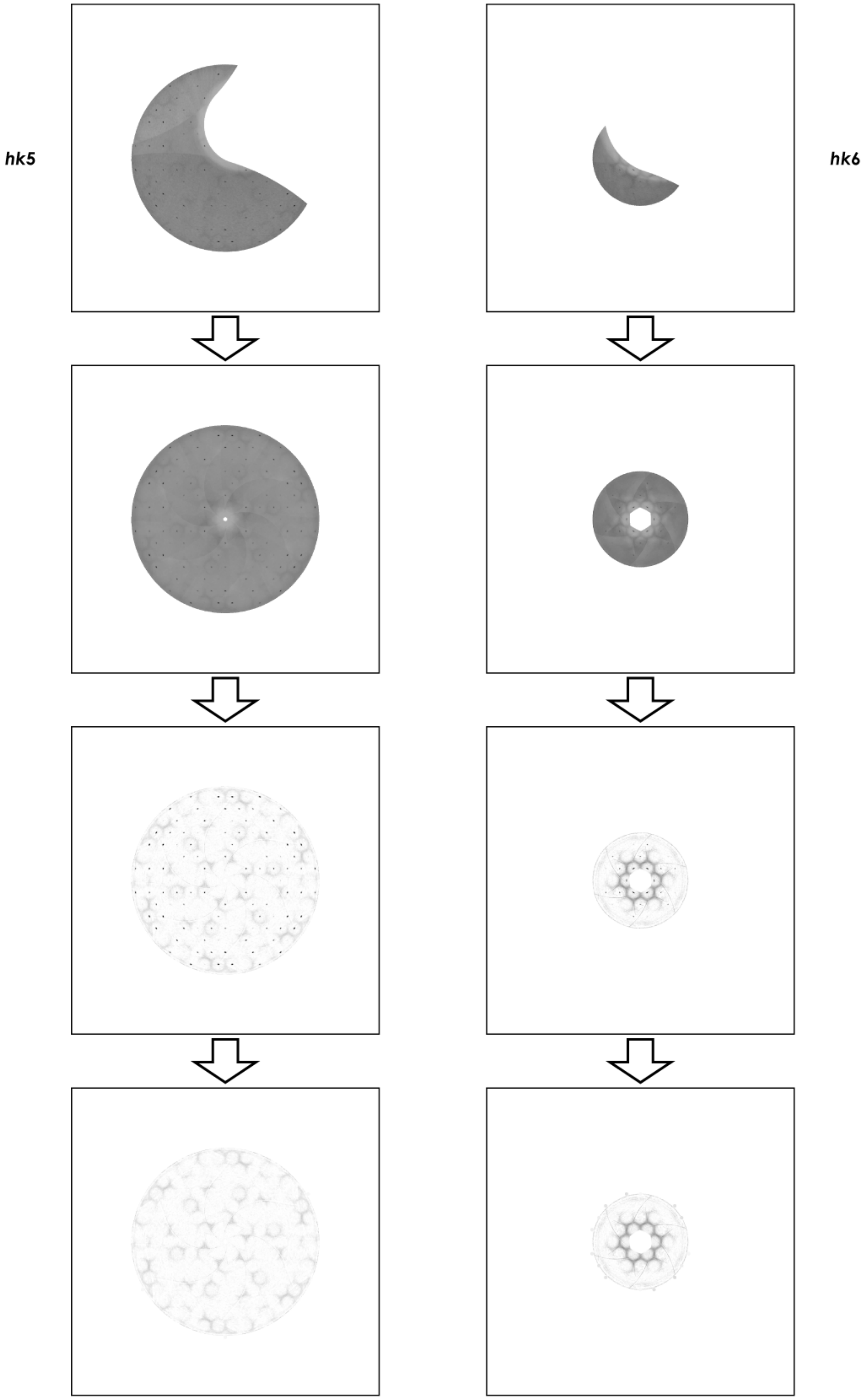
hk5
hk6

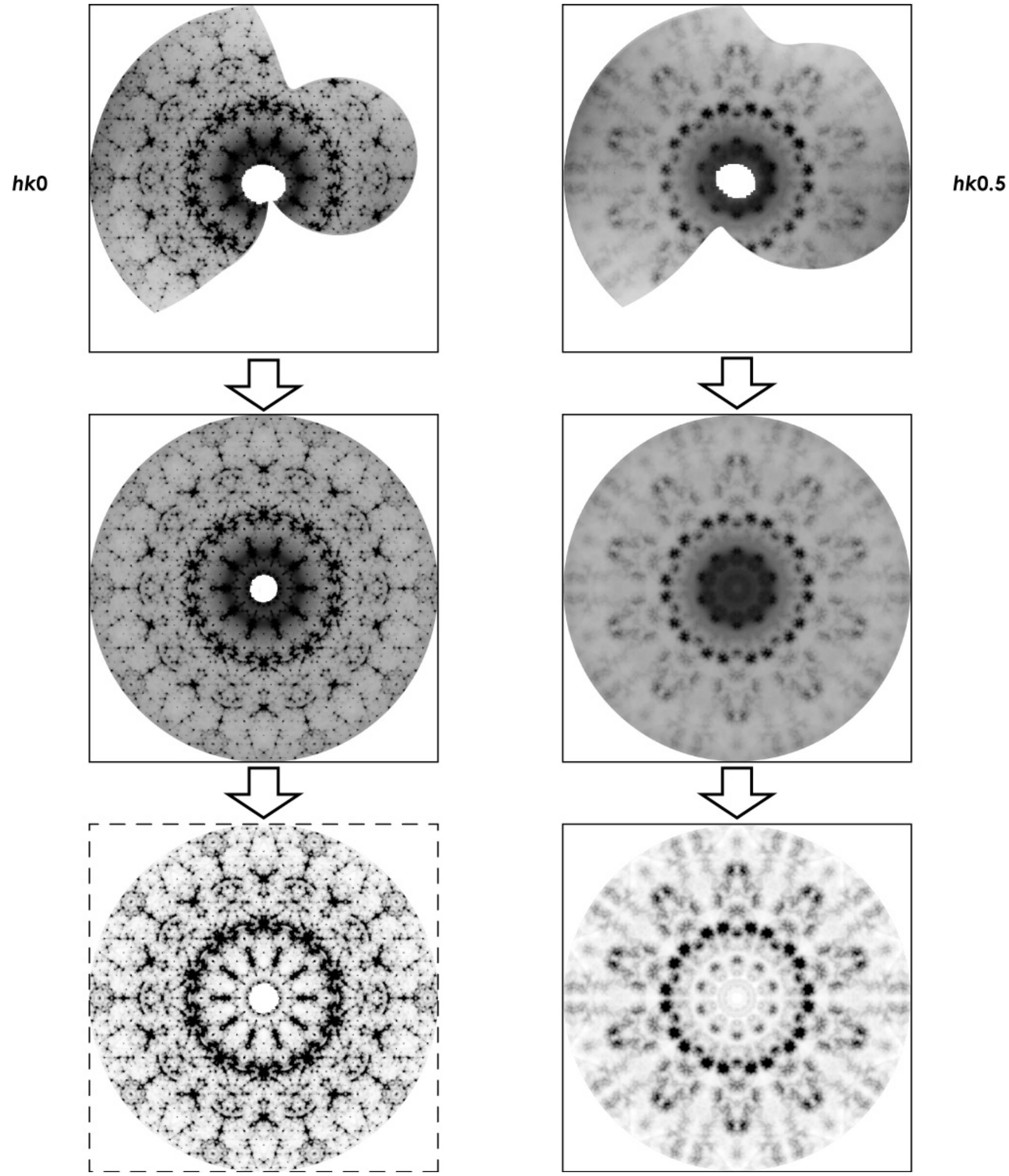

Figure 5.3 (pp. 64-68): Steps of data processing of the experimental single-crystal X-ray diffraction pattern of *d*-Al–Cu–Co. Main layers and diffuse interlayers from $l = 0$ to 4.5 are shown. From top to bottom: reconstructed diffraction pattern — after symmetry equivalent averaging — after removal of static background. Main scattering layers are presented for the sake of completeness and were not used in ΔPDF analysis. The edges of each box cover a range of ± 1.187 Å^{-1}. In the layers *hk*0 and *hk*0.5 the beam-stop shadow was masked. In layer *hk*0.5, the resulting gap was filled in the averaging process with measured intensities from layer *hk*-0.5.

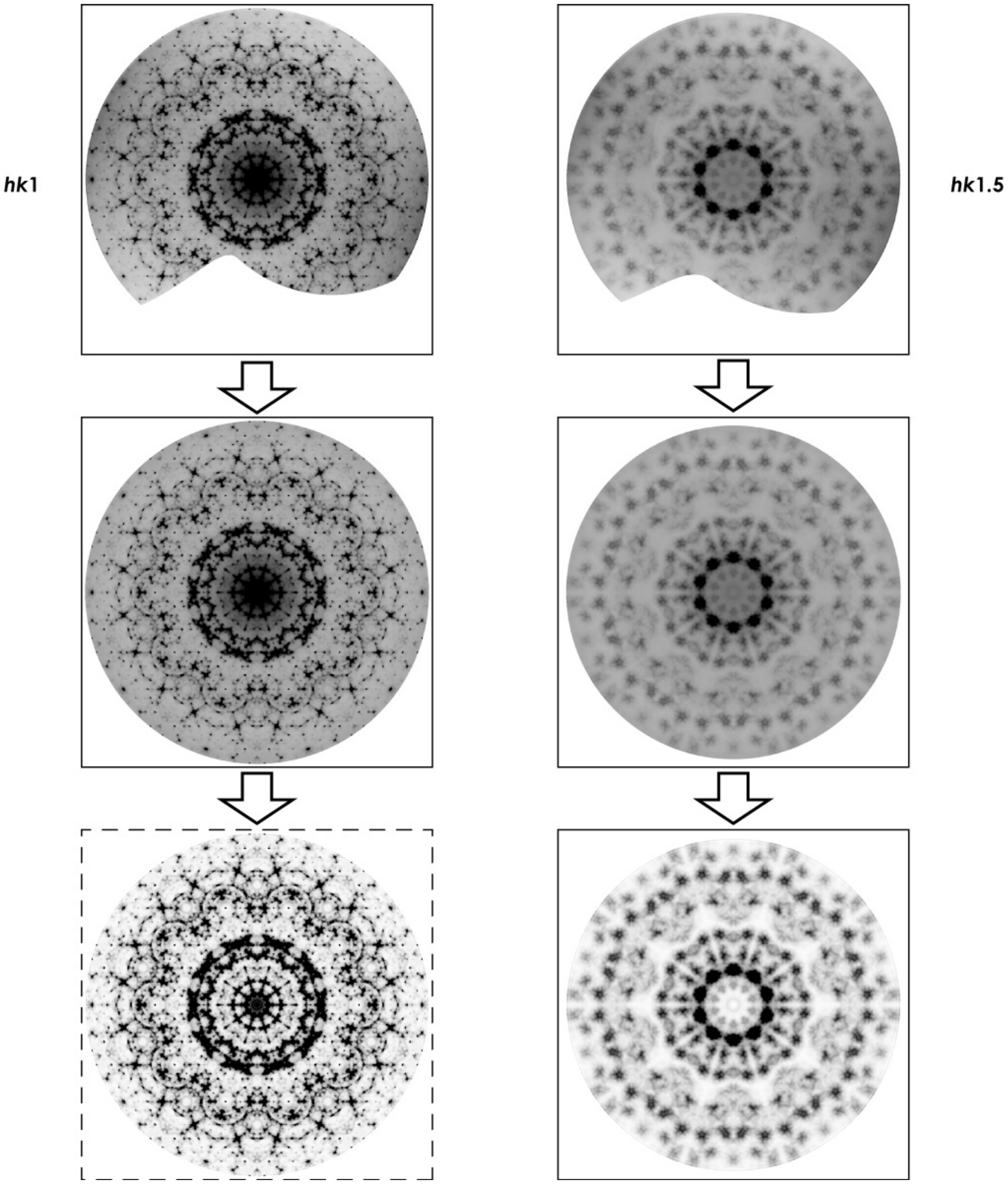
hk1
hk1.5

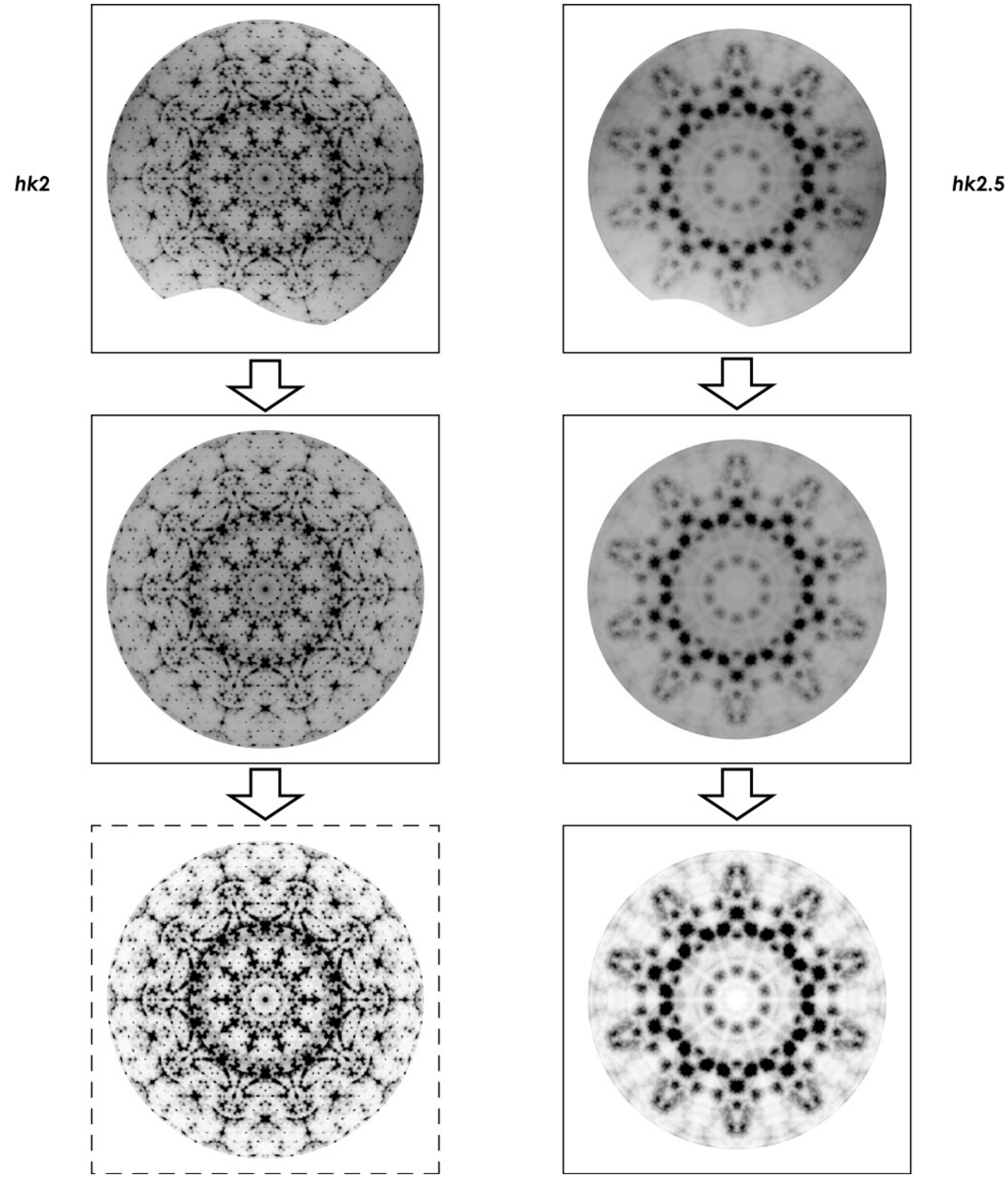
*hk*2
*hk*2.5

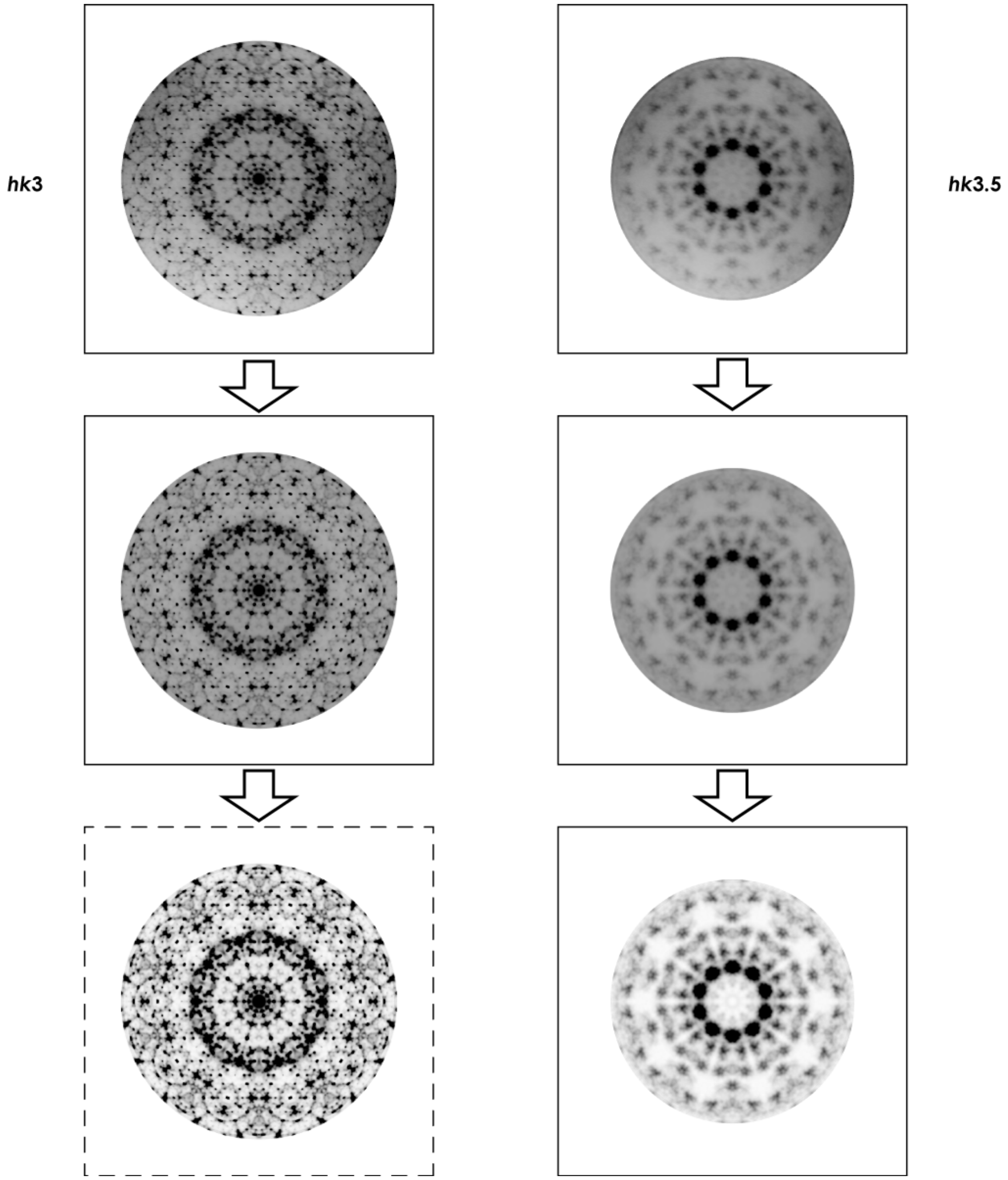
*hk*3
*hk*3.5

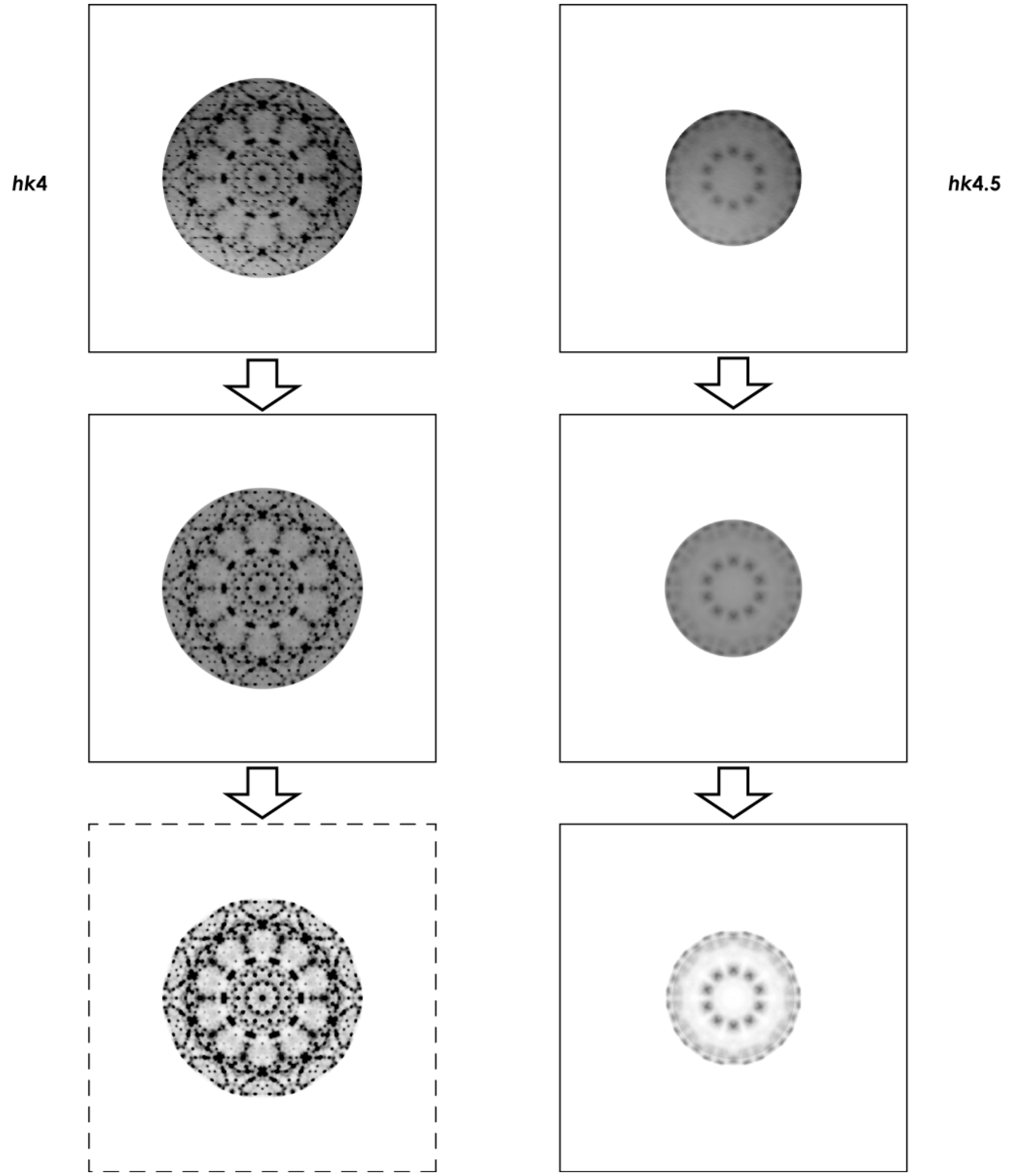
hk4
hk4.5

5.3. Bragg peak elimination

As pointed out in section 2.1.7, analysis of the ΔPDF is preferred over the total scattering PDF. Information on difference structure correlations has to be separated from average structure contributions therefore. In reciprocal space, these contributions of long-range ordered lattice vectors are confined to the well-defined nodes of the reciprocal lattice. In PDF space on the other hand, the correlation lengths of locally disordered structural motifs are on the same length scale as short interatomic distances of the average structure, and so they could just hardly be distinguished in the total scattering PDF. Hence, diffuse scattering intensities have to be separated from Bragg intensities *before* the PDF is calculated. In most parts of reciprocal space $|F_{hkl}(\mathbf{h})|^2 = 0$, and the term $I(\mathbf{h}) - |F_{hkl}(\mathbf{h})|^2$ can be easily calculated to obtain the ΔPDF. Special care has only to be taken at the Bragg peak positions.

A straightforward way to filter the data is the *"punch-and-fill"* method (Kobas *et al.*, 2005). At reciprocal lattice points, *i.e.* at the positions of Bragg peaks, the scattering intensities are firstly cleared (*punch*), and thereafter, restored to probable values estimated from the surrounding area (*fill*). The extent of the punched and afterwards filled volume is specified via a window function $w_{p\&f}(\mathbf{h})$, with $w_{p\&f}(\mathbf{h}) = 1$ within the range to be punched and $w_{p\&f}(\mathbf{h}) = 0$ elsewhere. $f_{p\&f}(\mathbf{h})$ is the estimated fill function, thus the PDF calculated from a "*punched-and-filled*" data set is (for the derivation see Kobas *et al.* (2005))

$$P_{p\&f}(\mathbf{r}) = P_{tot}(\mathbf{r}) - \left[\left(P_{tot}(\mathbf{r}) + F_{p\&f}(\mathbf{r})\right) \otimes \left(G(\mathbf{r})\, W_{p\&f}(\mathbf{r})\right)\right] \approx \Delta P \tag{5.3}$$

Here, $G(\mathbf{r})$ is the Fourier transform of the reciprocal lattice function, corresponding to the translation function of the unit cell; $F_{p\&f}(\mathbf{r})$ and $W_{p\&f}(\mathbf{r})$ are the transforms of $f_{p\&f}(\mathbf{h})$ and $w_{p\&f}(\mathbf{h})$, respectively. As $w_{p\&f}(\mathbf{h})$ is usually a narrow box function, $W_{p\&f}(\mathbf{r})$ is a broad shaped function, which does not bias the PDF at short correlation lengths. For ideally chosen $f_{p\&f}(\mathbf{h})$, the term $((P_{tot}(\mathbf{r}) + F_{p\&f}(\mathbf{r})) \otimes (G(\mathbf{r}) \cdot W_{p\&f}(\mathbf{r})))$ comprises the complete periodic fraction of the PDF. Consequently, $P_{p\&f}(\mathbf{r})$ represents the non-periodic correlations, equal to $\Delta P(\mathbf{r})$. For further details on the "*punch-and-fill*" method see Kobas *et al.* (2005).

To ensure that the "*punch-and-fill*" filter yields an optimal result, the size of the window function has to be chosen as narrow as possible, but still large enough to fully cover the boundaries of all Bragg peaks.

In practice two differing methods to separate diffuse scattering from Bragg scattering intensities by means of a "*punch-and-fill*" filter were tested on *N,N',N''*-tris-*t*-butyl-1,3,5-benzene tricarboxamide. In the first approach, the "*punch-and-fill*" process was directly applied on the raw data as they were available from measurement. Removal of Bragg peaks in this early stage has the advantage that these unwanted intensities will not bias the further process of data processing. Additionally, inadequatenesses of the "*punch-and-fill*" filter will be diminished in the forthcoming averaging process, *e.g.*, if some marginal intensities of a wide Bragg peak persist, or if the fill process includes erroneous data in the surroundings of the eliminated peak.

The positions of all expected Bragg peaks within the data volume were calculated using the Ewald construction. The required parameters of experimental setup, such as the orientation matrix of the crystal's coordinate system relative to the laboratory coordinates, the sample–detector distance, and the horizontal and vertical offset of the detector from the ideal origin, were determined using the software package *XDS* (Kabsch, 1993). Coordinates of Bragg peaks were calculated in the detector coordinate system (x_d, y_d, ϕ), in which the oscillation angle ϕ is proportional to the frame number in the sequence of recorded 2D sections of reciprocal space. At each coordinate of a Bragg peak an ellipsoid with half axes $1.35\ \text{mm} \times 1.35\ \text{mm} \times 1.50°$ was punched out (Fig. 5.4). The size of the equatorial circular section of such an ellipsoid corresponds to an opening angle $2\theta = 0.05°$ in the centre of a data frame at the sample–detector distance of 179.77 mm. Subsequently the punched volume was filled with a constant average value, which was calculated from the remaining pixel values in a cuboidal box enclosing the ellipsoid. After the "*punch-and-fill*" filter was applied, the data were transformed into undistorted reciprocal space coordinates as specified in section 3.4.

In a second approach, diffuse scattering intensities were separated from Bragg scattering after symmetry equivalent averaging and subtraction of the background signal in the reconstructed reciprocal space data, as described in section 3.4. As Bragg peaks lie on a regular lattice (Fig. 5.2), they are much simpler to localise at this stage. A 2D circular window function with diameter $0.02\ \text{Å}^{-1}$ was used to punch Bragg peaks. The fill function was similar to the example above, except that a 2D square box function was used now to calculate the fill values. A drawback of this method is that the fill function produces uniformly flat plateaus within the diffuse intensities that may simulate a non-existing long-range periodicity. Further, remaining strong intensities of improperly punched Bragg peaks will produce spurious fill levels.

However, the obtained diffuse scattering intensities of *N,N',N''*-tris-*t*-butyl-1,3,5-benzene tricarboxamide did not significantly differ after all steps of data enhancement, irrespective in which of the two ways the "*punch-and-fill*" method was implemented. The segregative distribution of Bragg and diffuse intensities was evidently too clear in this simple example to be decisive between the two variants.

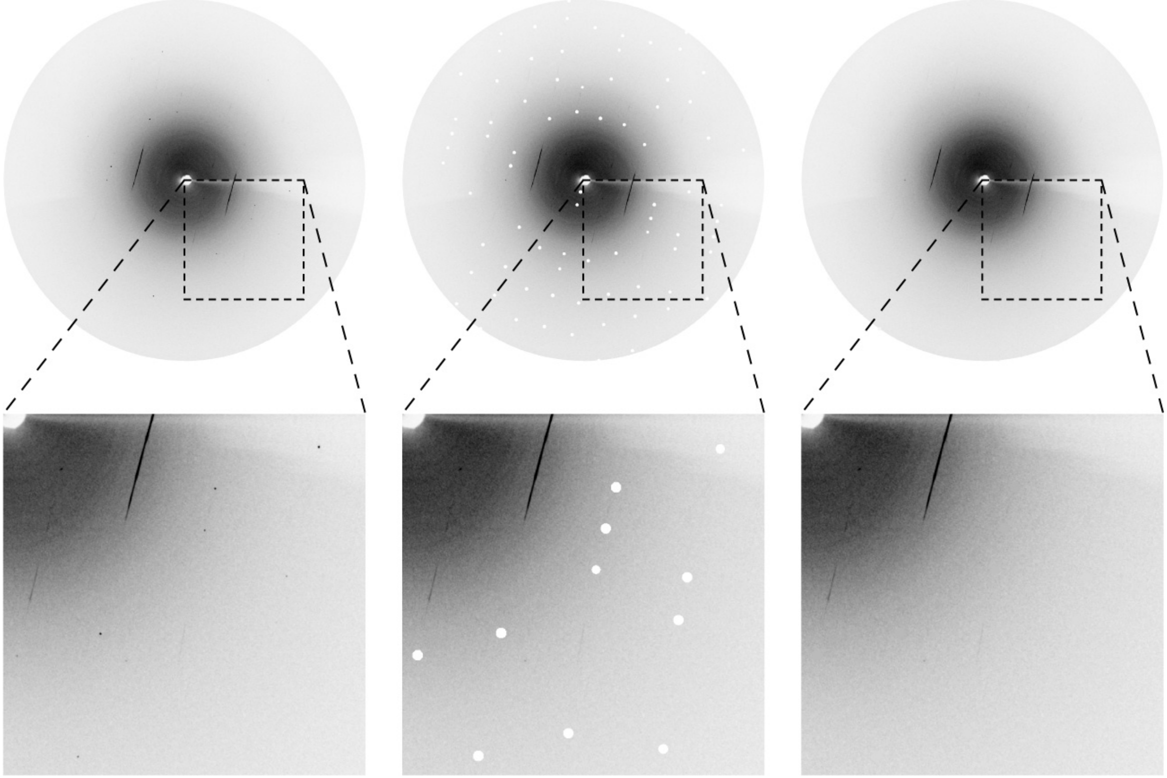

Figure 5.4: The *"punch-and-fill"* method applied directly on the raw data of the X-ray diffraction experiment. The three steps shown are from left to right: before application of the *"punch-and-fill"* filter, after the *punch* process, and after the *fill* process. The top row shows a full data frame of the *Marresearch mar345* image plate detector, the lower row shows enlarged sections.

In the study of *d*-Al–Cu–Co, on the other hand, no "*punch-and-fill*" of single Bragg peaks was necessary. For analysis of disorder in the twofold superstructure only the diffuse interlayers were of interest, and the main scattering layers could be ignored (see section 4.3.4). For this reason, only the intensities of the diffuse interlayers at l = -4.5 …4.5 were included in the further analysis, whereas the layers at integral l coordinates were set to zero. No supplementary data filtering was necessary. This procedure is equal to applying a "*punch-and-fill*" filter with a window function covering the whole Bragg layers ($w_{p\&f}(\mathbf{h}) = w_{p\&f}(h,k,l) = 0$ with l = -4, - 3, …, 3, 4 and $w_{p\&f}(\mathbf{h}) = 1$ elsewhere) and a fill function $f_{p\&f}(\mathbf{h}) = 0$.

5.4. Fourier transform

Experimentally collected scattering intensities are sampled in a limited reciprocal-space volume at a given voxel resolution. The PDF is computed by *discrete Fourier Transform* (DFT), hence:

$$P(\mathbf{r}_j) = \frac{1}{\sqrt{N}} \sum_{n=0}^{N-1} I(\mathbf{h}_n)\left(\cos(2\pi \mathbf{r}_j \mathbf{h}_n) + i \sin(2\pi \mathbf{r}_j \mathbf{h}_n)\right) \tag{5.4}$$

For a given 3D scattering data set with edge lengths H, K, and L in reciprocal orthogonal voxel space, the voxel sizes of the computed PDF become H^{-1}, K^{-1}, and L^{-1}, respectively. Depending on the maximum measured diffraction angle and oscillation range, as well as the wavelength used, H, K, and L amount to a few Å^{-1} for typical area detectors in a single-crystal experiment. Consequently, the voxel sizes are in a range of several 0.1 Å. The number of sampled voxels per each edge, n_H, n_K, and n_L, typically amounts to several hundreds or thousands, thus the ranges covered by the 3D-PDF become $X_P = \pm 0.5\ n_H/H$, $Y_P = \pm 0.5\ n_K/K$ and $Z_P = \pm 0.5\ n_L/L$, which is usually considerably larger than the range of interest for local disorder phenomena. Thus the pixel size of common area detectors is not a critically influencing factor in 3D-PDF analysis.

After the symmetry equivalent averaging process, the experimental data are a truly real-even, centrosymmetric function, *i.e.* $I(\boldsymbol{h}) = I(-\boldsymbol{h})$. Consequently the term $\sum(I(\mathbf{h})\ i \sin(2\pi\ \mathbf{r}\ \mathbf{h}))$ sums up to zero, and the Fourier Transform of $N = n_H \cdot n_K \cdot n_L$ discrete data values reduces to a real-valued discrete cosine transform (DCT), so that

$$P(\mathbf{r}_j) = \frac{2}{\sqrt{N}} \sum_{n}^{\substack{half\\volume}} I(\mathbf{h}_n) \cos(2\pi \mathbf{r}_j \mathbf{h}_n). \tag{5.5}$$

wherein the summation runs over a non-redundant half of the data volume. Both, memory requirements and time consumption of the computation can be reduced appreciably.

5.5. Implementation note on Fourier Transforms

For convenience, instead of using a DCT a *discrete Hartley transform* (DHT; Bracewell, 1983) was computed in the software implementation developed for this work. Computation of the PDF via DHT instead of DCT was chosen because of the easy to use interface of the available software libraries (*FFTW3*; Frigo & Johnson, 2005), and the easy to implement data post-processing routine (see below). The PDF calculated by DHT is

$$P(\mathbf{r}_j) = \frac{1}{\sqrt{N}} \sum_{n=0}^{N-1} I(\mathbf{h}_n)\left(\cos(2\pi \mathbf{r}_j \mathbf{h}_n) + \sin(2\pi \mathbf{r}_j \mathbf{h}_n)\right). \tag{5.6}$$

As an inversion centre is always present in a PDF, the sine terms will sum up to zero and the transform is equivalent to a DCT.

The scattering intensities were first Hartley transformed separately in all three space dimensions. *Fast DHT* (Bracewell, 1984) routines of the *FFTW3* software library were used. The worst-case complexity of these transformations of a data set consisting of N voxels is $O(N \log N)$. In order to obtain the true 3D DHT, the data were post-processed using the method by Hao & Bracewell (1987) thereafter. The complexity of this data processing step is $O(N)$, so it is negligible compared to the DHT process. There is no gain in speed using a DHT instead of a DCT. A drawback of the implementation by DHT is, however, that the input data cannot be reduced to a non-redundant half-space volume, and so memory consumption is higher than by DCT.

6. Practical Aspects of 3D-ΔPDF Modelling

6. PRACTICAL ASPECTS OF 3D-ΔPDF MODELLING

In the following, additional aspects of 3D-ΔPDF modelling are presented as an extension to the results shown in chapter 4. Again, the twofold superstructure of *d*-Al–Cu–Co serves as basis for all following investigations.

In this chapter, two different definitions of the reliability index *R* will be used and compared. On one hand, these are the *R* values calculated from ΔPDF densities as they were defined by eq. 4.17 and used in for the refinement presented in section 4.3.6 to evaluate the agreement between experimental and modelled PDFs. On the other hand, collateral *R* values are likewise calculated directly from diffuse scattering intensities in the following (for a definition see section 6.4.1). In order to differentiate between the *R* values refined against the PDF densities, or against the diffuse scattering intensities respectively, the symbols R_P and R_I will be used hereinafter.

6.1. Analysis of the sensitivity of ΔPDF models to PDF space resolution

6.1.1. Objective and method

In section 4.3.6, a 3D-ΔPDF computed from diffuse X-ray scattering of a modelled structural unit was successfully compared to experimental PDF data. The size of the model 3D-ΔPDF was determined by intrinsic properties of the sample, *i.e.* in x_P and y_P direction by the maximum correlation length found in the experimental data, and in z_P direction by the periodicity of the twofold superstructure in **c** direction. The PDF voxel size, however, was constrained to be identical in the experimental and the modelled data set, and was predetermined by the extent of reciprocal space covered by the experiment, *i.e.* it was a consequence of experimental design. Factors that have an effect on the PDF voxel size are, thus, the wavelength used in experiment, the maximum diffraction angle measured, the size of the area detector, and the choice of an oscillation angle that covers at least one full asymmetric unit of the experimentally accessible reciprocal space volume.

As in the PDF neighbouring voxel values are statistically dependent on their neighbours, PDF densities are expected to be sensitive to variations of interatomic distances that are much smaller than the voxel size. In order to estimate the sensitivity of PDF models in dependence of the PDF voxel size, a qualitative study of synthetic 3D-ΔPDF data, comparable to the results presented in chapter 4, computed at different voxel sizes was carried out.

For this test, ΔPDFs of a single Al atom pair separated by an interatomic vector **d** (*i.e.* an interatomic distance $d = |\mathbf{d}|$) were computed. An average structure with an occupation factor of 0.5 on each of both atom sites was assumed. Relative to this, a real structure representation was defined via a difference structure, with a relative occupation of +0.5 on one atom site, and -0.5 on the other one, simulating one fully occupied Al site and one vacancy. A reference 3D-ΔPDF was computed at different voxel sizes (see below) for this structure with the two atom coordinates (1.331 Å, 0.433 Å, 0.000 Å) and (-1.331 Å, -0.433 Å, 0.000 Å), respectively. The interatomic distance d_{ref} was 2.800 Å. The position of the two atom sites was chosen in a general orientation, so that their connecting vector did not coincide with the symmetry elements of the orthogonal PDF voxel grid, except the (x_P,y_P)-plane. In this way highly symmetric PDF peak shapes were avoided.

A series of test 3D-ΔPDFs was computed then, with varying interatomic distances d, The orientation of **d** and the relative occupation factors of +0.5 -0.5 were kept constant. R_P values were calculated, comparing each of these PDFs with the reference PDF. The fitness function R_P was the same as described in section 4.3.6. No masking or weighting of PDF voxels was applied. Generally speaking, the ΔPDF of such an atom pair shows, additionally to a central positive density from self-correlations in the origin, a negative peak at each, **d** and **-d**. With variation of d, these peak positions move relatively to the origin. The integrated peak densities remain constant, but the peak shapes of the moving peaks slightly vary, depending on their intersection with the voxel grid.

Series for $d = 0.000$ Å until 5.600 Å were computed at different voxel sizes. The total number of voxels in the diffraction patterns was left unchanged in all cases, namely 200×200×20 (the same as used for the structural model presented in chapter 4), but the voxel size was varied, simulating an experiment with a constant detector at different wavelengths or sample–detector distances. The procedure of calculation was the same as for the ΔPDFs of the *d*-Al–Cu–Co model. In a first step, diffraction patterns of the atomic pair were computed, and subsequently ΔPDFs were calculated. A spherical mask simulating the detector envelope function was applied to the diffraction data, each with a radius equal to half of the respective length of the edges in h and k direction. R_P values were calculated for each series as a function of d, using a scaling factor determined by linear least squares fitting.

The ΔPDFs showed, as expected, only significant densities in the layers at $z_P \approx 0.000$ Å (Fig. 6.1). ΔPDF series with voxel sizes of 1.000, 0.562, 0.421 (equal as in the *d*-Al–Cu–Co model), 0.211, and 0.100 Å in x_P and y_P directions were generated. The voxel size in z_P direction was 0.411 Å in all cases. The stated voxel sizes correspond to edge lengths in orthogonal h and k directions of the respective diffuse diffraction patterns of ±0.500, ±0.890, ±1.187, ±2.374, and 5.000 $\mathrm{Å}^{-1}$ (see Fig. 6.1).

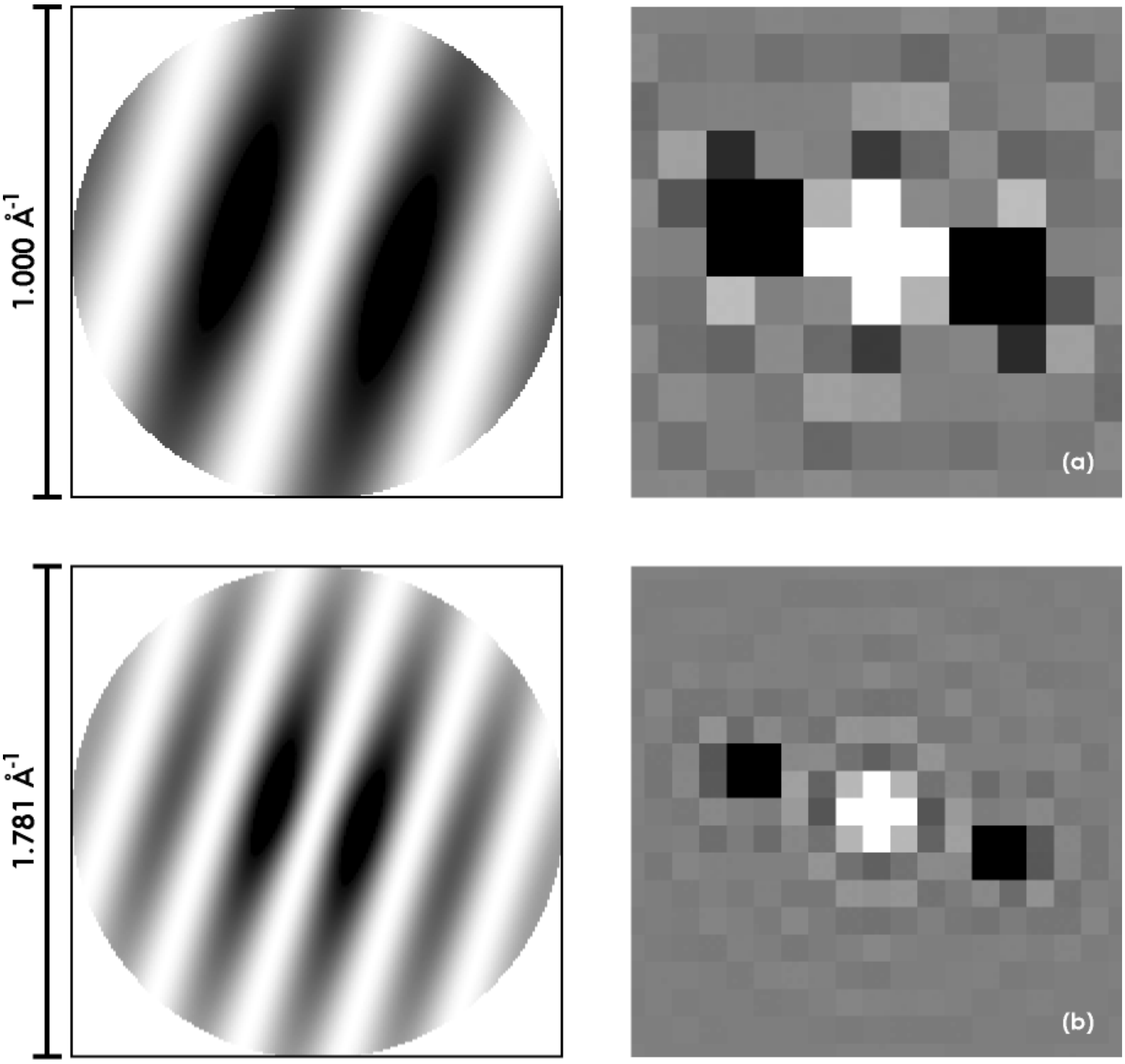

Figure 6.1 (pp. 78-79): Diffraction patterns (*hk*0.5 layer) and 2D sections through 3D-ΔPDFs ($z_P \approx 0.00$ Å) of the difference structure of an isolated Al–Al pair separated by a distance $|\mathbf{d}| = d_{ref} = 2.800$ Å (for further details see text). The diffraction patterns, having 200×200 pixels each, cover different ranges of reciprocal space (as indicated in the figure). The resulting voxel sizes of the ΔPDFs in x_P and y_P directions are (a) 1.000 Å, (b) 0.562 Å, (c) 0.421 Å, (d) 0.211 Å, (e) 0.100 Å. The range shown by each section of a ΔPDF is ±5.05 Å in x_P and y_P directions.

In an additional series, the ΔPDF of a pair of Cu atoms was computed in order to measure the effect of incorrectly assigned atom types. The PDF voxel size was 0.421 Å in x_P and y_P directions. The further setup and procedure was identical as for the Al pairs. These ΔPDFs were also compared to the reference structure occupied with Al atoms.

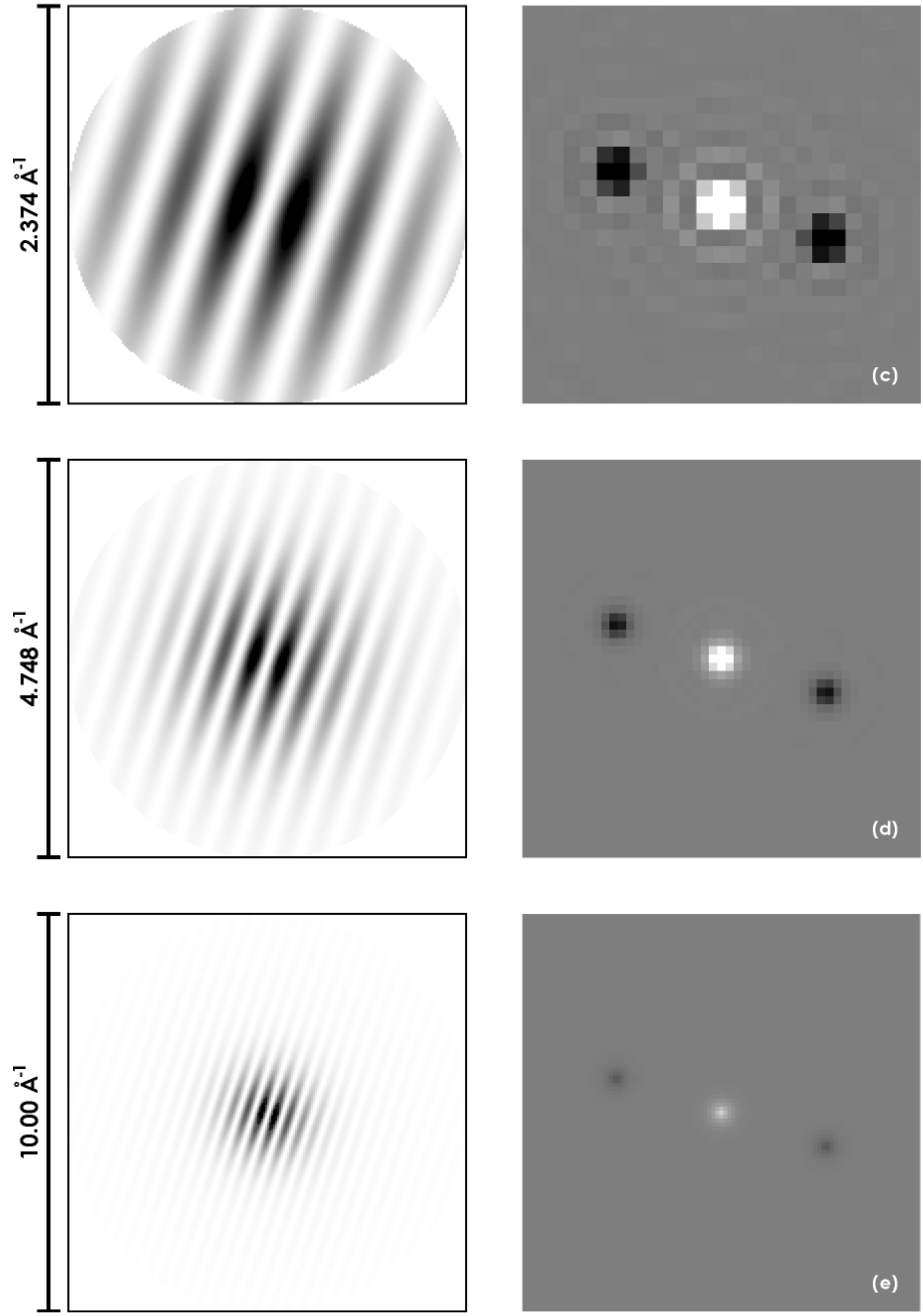
2.374 Å⁻¹
(c)
4.748 Å⁻¹
(d)
10.00 Å⁻¹
(e)

6.1.2. Results and discussion

The R_P values as a function of displacement off the ideal distance, $\Delta d = d - d_{ref}$, are shown in Fig. 6.2. It can be seen that, irrespective of the voxel size, the values of R_P stagnate over a wide range of Δd, and then suddenly get trapped if the displacement goes below a certain limit. The fluctuation of R_P is nearly the same for all voxel sizes, except for the largest voxels with size 1.000 Å. Below a difference distance of about 0.8 Å to d_{ref}, R_P declines steeply towards zero. The position of the inflexion point corresponds roughly to the width of the ΔPDF peaks at about 10% of their maximum density. If Δd is longer than this threshold value, the peaks do not overlap significantly and R_P is constantly high, governed only by the agreement of the two origin peaks. In the examples shown here, this level is at about 0.75. At a (unphysically short) distance d near zero, the electron densities of the atomic pair overlap in the difference structure, and R_P increases again. Within the $|\Delta d|$ <~ 0.8 Å range however, the negative ΔPDF peaks overlap. The less their central positions are shifted relative to each other, the smaller R becomes. From the inset of Fig. 6.2, it can be seen that R_P values are sensitive in the range of a few percent even for small offsets in the order of several 10^{-3} Å. R_P values computed for the largest investigated voxel size 1.000 Å do not show an accentuated curve as they do for smaller voxel sizes. This is not a drawback in modelling a single atomic pair, but might result in a nondistinctive surface of R_P in a larger-scaled real-world application. Thus for a single atomic pair, ΔPDF modelling at an appropriate voxel size offers theoretically a very high accuracy, provided that there is no noise present, and the peak profiles of the experimental and the modelled peaks are identical. In practice however, this will hardly be the case. Additionally, when bigger structural units with a large number of atoms are modelled, ΔPDF peaks will overlap, introducing numerical correlations. For these reasons, R_P values will hardly ever drop to 0.0, and the comparatively high values encountered in the model of *d*-Al–Cu–Co in section 4.3.6 are consistent with this result. Nevertheless, it can be concluded that for standard experimental data ΔPDF modelling allows determining interatomic distances with an accuracy of at least 10^{-2} Å. For reliable results, the voxel size is required to be significantly less than the typical width of ΔPDF peaks. In the example shown here, this critical voxel size turned out to be approximately 0.8 Å. This result implies that specifically in case of the structural model of *d*-Al–Cu–Co, the voxel sizes of 0.421 Å and 0.411 Å determined by experimental factors were sufficiently small enough.

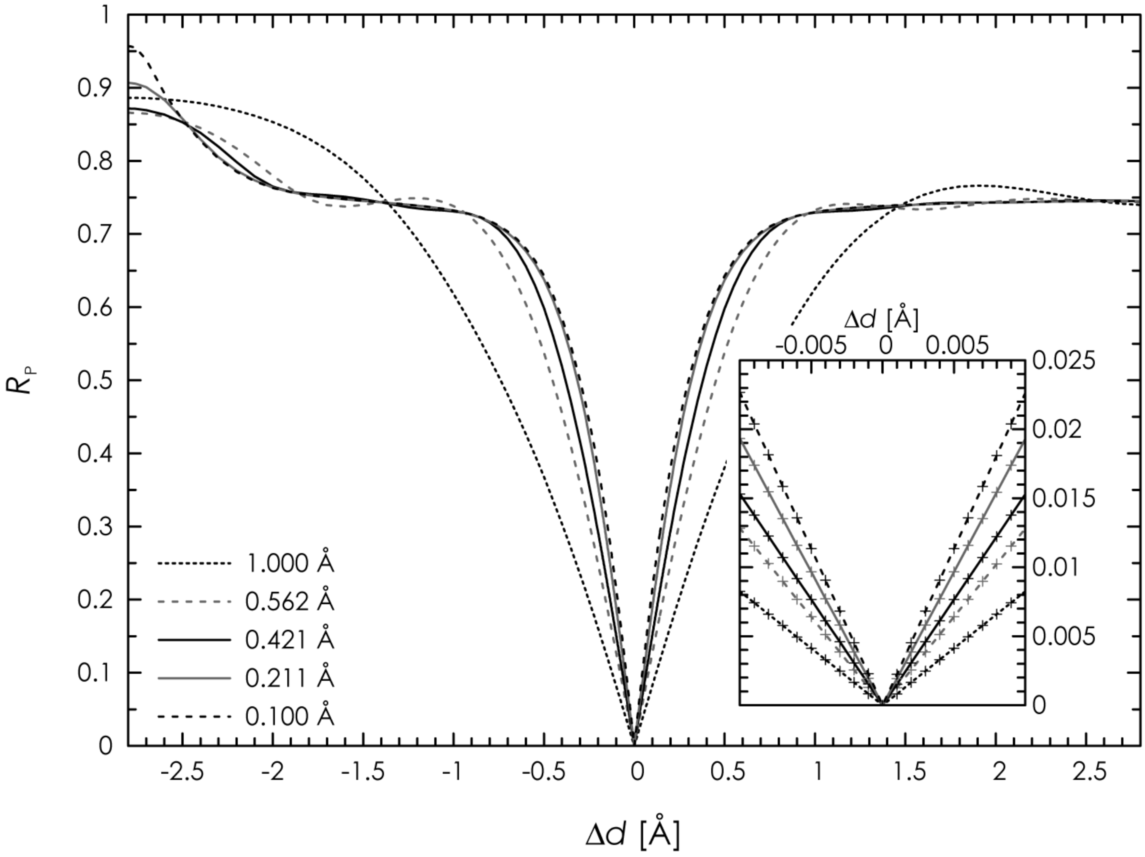

Figure 6.2: R_P values of ΔPDFs with different voxel sizes of an Al–Al pair as a function of displacement Δd apart from the reference position at a distance of $|\mathbf{d}| = d_{ref} = 2.800$ Å. The inset shows the highly enlarged interval $\Delta d = \pm 0.01$ Å. Crosses on the line indicate distances at which R_P was sampled. For further details and a discussion see text.

The R_P values Å of the "incorrect" model occupied with a Cu pair calculated at a voxel size of 0.421 Å are very similar to the values of the Al pair at the same voxel size (Fig. 6.3). Just within a range of $|\Delta d| <\sim 0.2$ Å they differ clearly. This means that in the process of model optimisation, the scaling factor applied to the data in the calculation of R_P buffers the difference originating from inadequately occupied atoms over a wide range of possible d, and not until the correct positions are closely approached, the difference in the peak profiles becomes significant. The minimum R_P found for the Cu pair at $\Delta d = 0$ Å is about 0.048. This residual corresponds to a displacement of $|\Delta d| \approx 0.03$ Å of a pair of correctly occupied Al atoms. Solely in terms of R_P it is, hence, not possible to distinguish between a slightly mispositioned, but correctly occupied Al pair, and an accurately positioned pair of atomic sites that is occupied with Cu instead of Al. However, the kind of mismatch can be determined by inspection of the differences of the exact peak positions and profiles in the ΔPDF. Although the effect is expected to be less substantial in larger atomic structures where each atomic site is dependent on multiple pair correlations, this observation is a possible evidence for the scattering weighting factors converging slower than positional parameters in the optimisation process of the *d*-Al–Cu–Co model (see section 6.3).

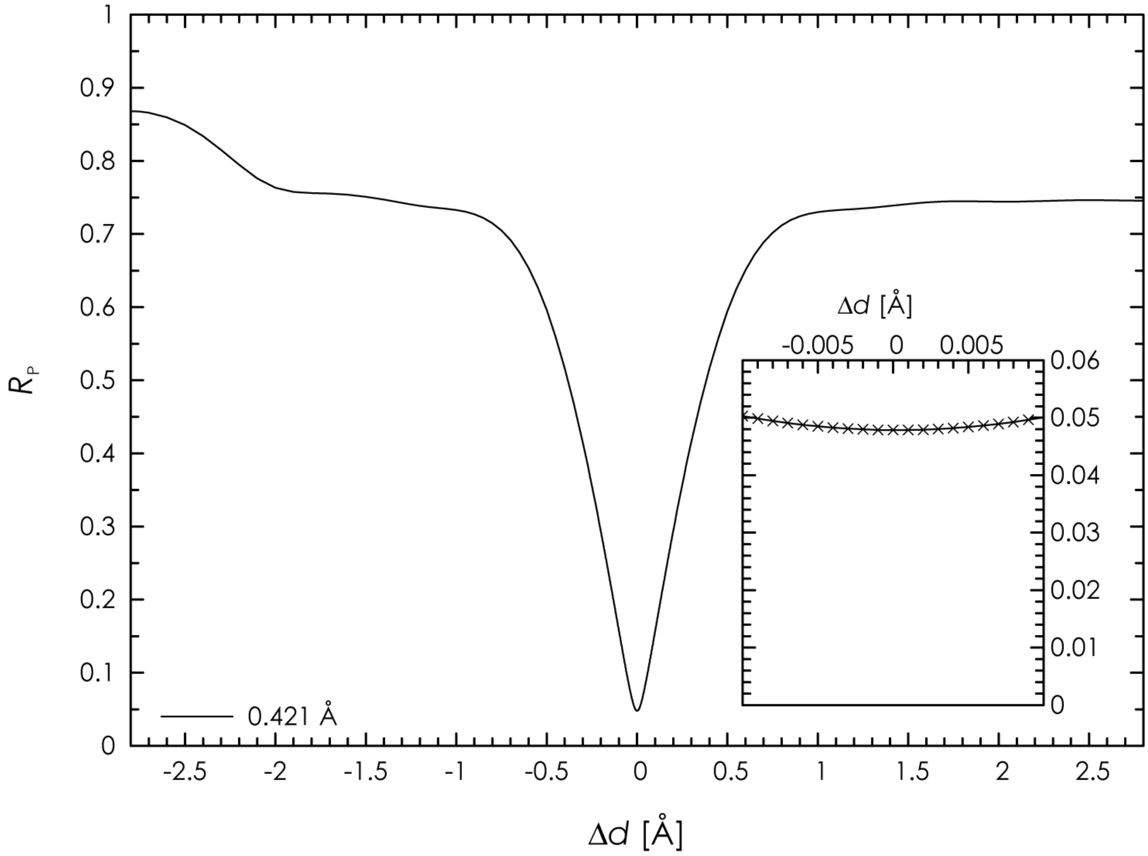

Figure 6.3: R_P values of the ΔPDF with voxel size 0.421 Å of a Cu–Cu pair as a function of displacement Δ*d* apart from the reference positions (occupied with Al–Al) at a distance of $|\mathbf{d}| = d_{ref} = 2.800$ Å. The inset shows the highly enlarged interval Δ*d* = ±0.01 Å. Crosses on the line indicate distances at which R_P was sampled. Note that the scale of the vertical R_P axis of the inset is larger than in Fig. 6.2. For further details and a discussion see text.

6.2. Comparative study of different partial models

6.2.1. Investigated models

As it was pointed out above, 3D-ΔPDF analysis allows studying partial structural models. This useful quality will be illustrated on different partial realisations of the disordered structural motif found in *d*-Al–Cu–Co. The following four models were compared:

(i) The "complete" structural model is the variant discussed in chapter 4. It serves as a basis for all other variants listed below.

(ii) The first partial model tested was identical to the "complete" model (i), except that the model parameter a (see section 4.3.5) was fixed to 0.000, *i.e.* no cylindrical exponential attenuation was applied. In this way, a qualitative impression of the necessity to allow for internal instability of the disordered structural motif is obtained. Further, this model variant will be useful in pointing the benefits of PDF modelling compared to reciprocal-space modelling out (see below).

(iii) In the second partial model, the inner flat ring was dropped. In the initial trial-and-error stage of model evolution, it had turned out that the inner flat ring was the most unstable and fluctuating feature in the disordered structural motif. The model parameters associated with the inner flat ring converged slow and inconclusive. This observation also led to the omission of one fivefold atomic orbit of the initially tenfold inner flat ring in the "complete" model: The respective atoms positions did not move away from their original positions on the *c*-glide planes during refinement (*cf.* section 4.3.6). Hence, the inner flat ring consisted only of five atomic positions in the real-structure representation. Here, the influence of omitting also this five-ring of atoms on the ΔPDF is tested.

(iv) The last partial model comprises only puckered layers. This model conforms to the optimised version of the qualitative intermediate model presented in section 4.3.5.

Models (i) to (iv) were refined using differential evolution in the same way as it was done for model (i) (see section 4.3.6). All dimensions and voxel sizes of the computed data sets were also identical thereto. The free model parameters and their initial values were, unless affected by one of the constraints mentioned above, defined as in Table 4.1. The four new structural models were optimised in an independent run each.

6.2.2. *Results and discussion*

The results of the refinements are listed in Table 6.1. ΔPDF maps and the underlying diffuse diffraction patterns are shown in Figs. 6.4 and 6.5, respectively. It turned out that all models converged to solutions that describe equivalent structures. The partial models nicely reproduce their covered parts of the "complete" model (i). Variation of the parameter values is small, only with a few appreciable exceptions. Generally, it can be seen that the geometrical parameters are more consistent, whereas the occupational parameters show more, slight variations, indicating that the shortcomings of the partial models are primarily compensated by atomic occupation rather than by geometrical rearrangements.

Table 6.1: Comparison of the refined model parameters of different models of disorder of *d*-Al–Cu–Co. For a description of the model variants see text. For all refined models both reliability indexes, R_P and R_I, are listed. The index that was actually used to refine the respective model is printed in bold. For definitions of the model parameters see Fig. 4.7 and Table 4.1.

	Model				
	(i)	(i, diffuse)	(ii)	(iii)	(iv)
parameter					
r_{pi}	4.802 Å	4.785 Å	4.796 Å	4.670 Å	4.783 Å
r_{po}	7.395 Å	7.400 Å	7.403 Å	7.379 Å	7.334 Å
Δz_{pi}	0.208 Å	0.228 Å	0.219 Å	0.283 Å	0.255 Å
Δz_{po}	0.368 Å	0.391 Å	0.385 Å	0.361 Å	0.457 Å
α_{pi}	-1.46°	-1.62°	-1.69°	-1.53°	1.34°
α_{po}	-0.29°	-0.26°	-0.29°	1.62°	2.34°
r_{fo1}	5.407 Å	5.410 Å	5.408 Å	5.457 Å	—
r_{fo2}	6.360 Å	6.317 Å	6.325 Å	6.408 Å	—
α_{fo1}	9.86°	9.93°	9.97°	9.61°	—
α_{fo2}	-2.67°	-2.65°	-2.64°	-3.33°	—
r_{fi}	3.866 Å	3.894 Å	3.877 Å	—	—
α_{fi}	-5.29°	-5.54°	-5.32°	—	—
a	0.059 Å^{-1}	*n/a*	*0.000* [1]	0.066 Å^{-1}	0.081 Å^{-1}
o_{po}	0.712	0.602	0.613	0.627	*1.000* [1]
o_{fo2}	1.259	1.263	1.324	0.956	—
o_{fo1}	*1.000* [1]	*1.000* [1]	*1.000* [1]	*1.000* [1]	—
o_{pi}	1.284	1.255	1.310	0.899	1.036
o_{fi}	1.297	1.321	1.380	—	—
R_P [2]	**0.300**	0.327 [3] / 0.387 [4]	**0.365**	**0.423**	**0.647**
R_I [5]	0.368	**0.366**	0.363	0.486	0.680
Best individual 1st time found in generation					
	1401	1694	1407	1052	206
population size					
	150	140	140	130	80

[1] fixed value

[2] calculated with use of a cylindrical mask with radius 16.6 Å

[3] with a = 0.059 Å^{-1}

[4] with a = 0.000 Å^{-1}

[5] calculated with use of a spherical mask with radius 1.187 Å^{-1}

At first, the partial model (iii), missing the inner flat ring, is compared to model (i). As a main difference, the inner puckered ring has a decreased diameter, but a slightly increased puckering height. In this way, the inner puckered ring, which is, regarding its diameter, the next smallest feature to the missing inner flat ring, compensates part of the shortest pair correlations. Although the allowed ranges of the positional model parameters were fairly wide, the displacements are small. Keeping the puckered ring close to the original arrangement seems to be favourable over compensating the missing correlation densities. Another remarkable difference to model (i) is the change of the angular displacement of the atoms on the outer puckered ring. This behaviour is also observed in the partial model (iv), which contains only puckered layers, thus the outer puckered ring tends to compensate missing pair correlations in both cases. The shortcomings of model (iii) are mainly at short correlation lengths (see Fig. 6.4). The difference in R_P to the reference model (i) is about 0.12. This manifests that, even the role of the inner flat ring in the global model was not clear, it contributes notably to the ΔPDF.

Model (iv), without flat layer contributions, converged to an R_P value of about 0.65, *i.e.* about 0.35 more than the R_P value of the complete model. Nevertheless, the configuration of the puckered rings is still similar to the "complete" model (i). However, puckering amplitudes are increased. Δz_{po} gets trapped at the upper limit of the allowed value range (*cf.* Table 4.1). Higher puckering amplitudes can be explained by a tendency to cover weak PDF densities in the layer at $z_P \approx 1.23$ Å, which are actually due to intra-layer correlations between flat and puckered layers. The scattering weighting factors of the inner and outer puckered ring are almost equal here, whereas in the other models the weighting factors of the outer puckered ring are generally less. When the ΔPDF of model (iv) is compared to the experimental ΔPDF (Fig. 6.4) as well as the ΔPDF of the model (i) (*cf.* Fig. 4.8), differences are found that are of the same kind as in the case of the intermediate flat-layer model in section 4.3.5 (*cf.* Fig. 4.6*a*).

The results of model (ii) with exclusion of exponential radial decay in the quasiperiodic directions are in good approximation equivalent to the "complete" model (i) (see Fig. 6.4, *cf.* Fig. 4.8). There are no remarkable changes in cluster geometry. The scattering weighting factor of the outmost feature, the outer puckered ring, has slightly decreased. On the other hand, the inner puckered and flat rings have slightly increased weighting factors. This observation shows that in absence of radial attenuation the too high level of distant ΔPDF densities is countervailed by weakening the longest pair correlations. However, this reduction may not be too strong, as the short ring-internal neighbour-to-neighbour correlations are also affected. Accordingly, the model converged to $R_P = 0.365$, which is significantly higher than for the same model with radial attenuation function taken into account. This indicates that in the real structure, disorder is prominent at short correlation lengths, and thus, intra-cluster disorder is present.

To summarise, by comparison of different stages of completeness of the model structure, it could be demonstrated that ΔPDF modelling yields stable and interpretable results even for partial models. Even if R_P values of incomplete models are significantly higher, the elementary characteristics of the disordered structure could be derived. Small deviations from the ideal values of the model parameters indicate a trend to compensate missing structural features, but nonetheless the structures did not drift away towards unreasonable solutions. In the examined models, parameters describing the geometry generally refine more stably than occupational parameters (see also below).

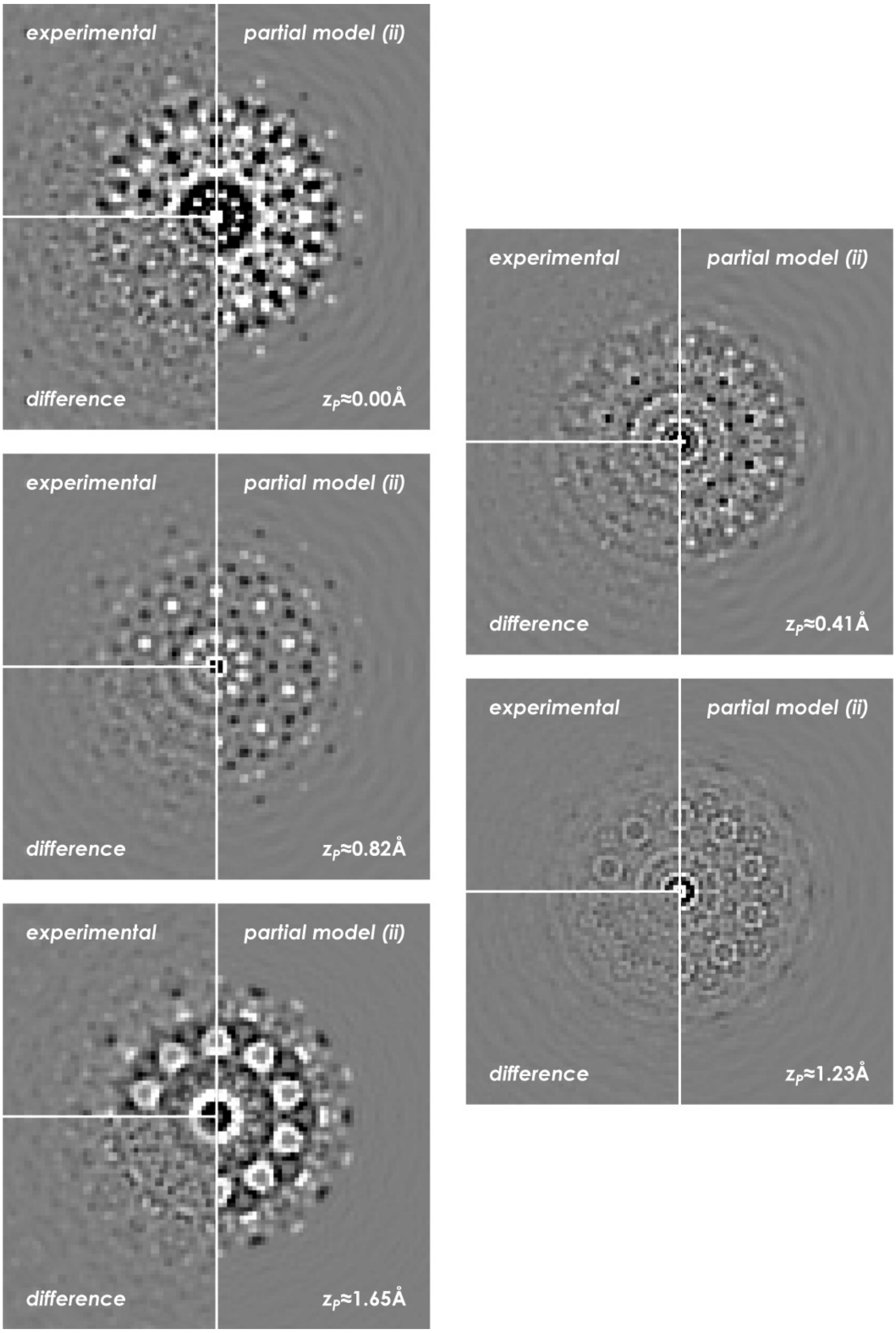

Figure 6.4 (pp. 87-89): Comparison of 2D (x_P,y_P)-sections through the experimental and the optimised modelled 3D-ΔPDF of partial models (ii) to (iv) of *d*-Al–Cu–Co. In the lower left quadrant of each image, the difference between the experimental and the modelled 3D-ΔPDF is shown. Positive differences ($\Delta\mathrm{PDF}_{\mathrm{exp}} > \Delta\mathrm{PDF}_{\mathrm{model}}$) are whitish, negative differences ($\Delta\mathrm{PDF}_{\mathrm{exp}} < \Delta\mathrm{PDF}_{\mathrm{model}}$) are blackish. The area covered by each image is ±21.27 Å along each axis. The colouring scheme of the experimental and modelled ΔPDF is the same as in Fig. 4.3.

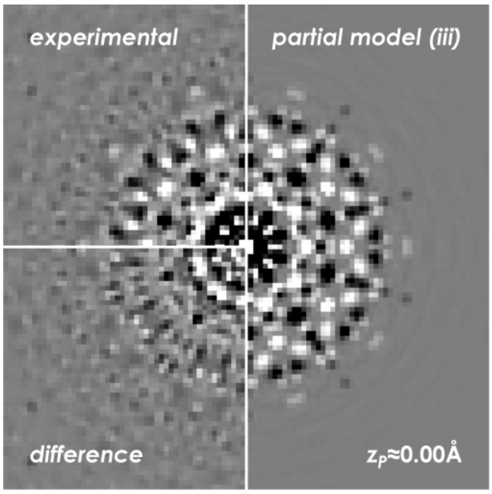
experimental
partial model (iii)
difference
z_P≈0.00Å

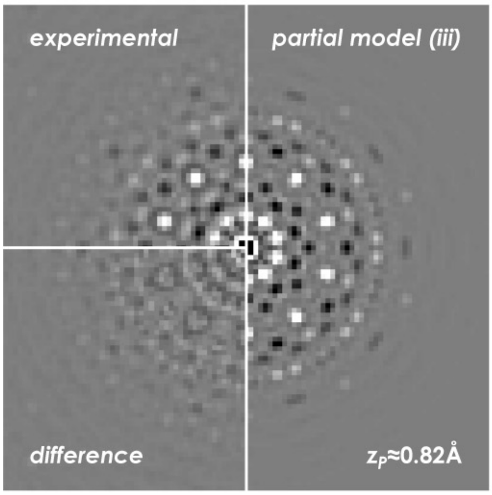
experimental
partial model (iii)
difference
z_P≈0.82Å

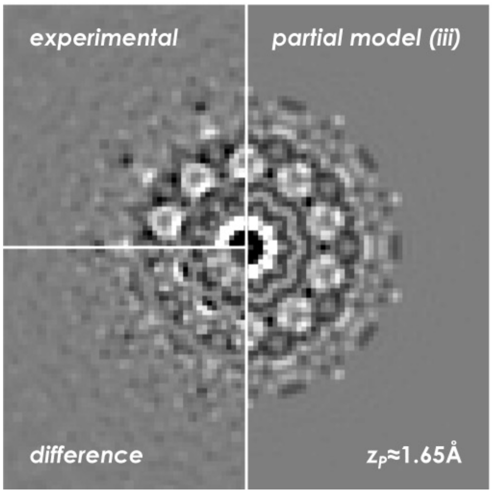
experimental
partial model (iii)
difference
z_P≈1.65Å

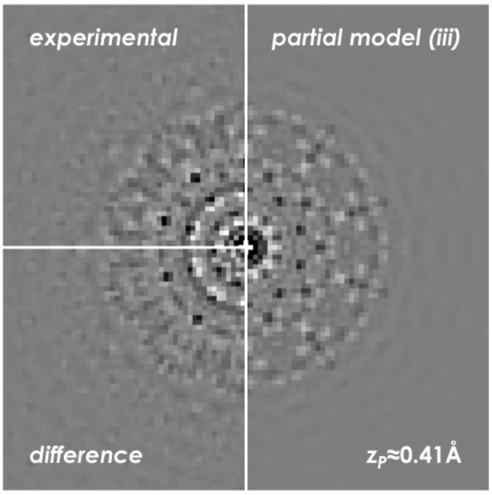
experimental
partial model (iii)
difference
z_P≈0.41Å

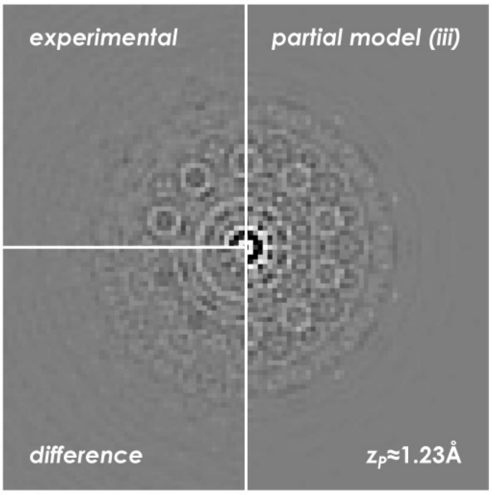
experimental
partial model (iii)
difference
z_P≈1.23Å

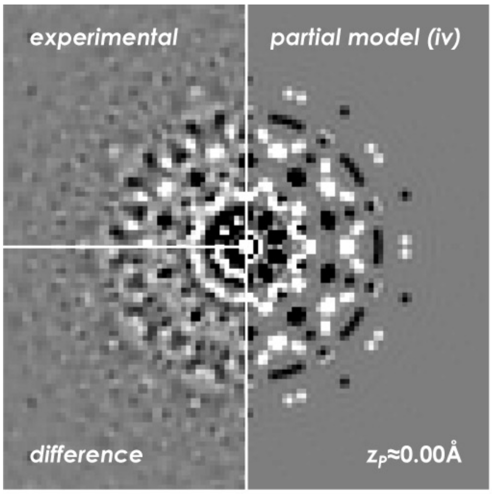
experimental
partial model (iv)
difference
z_P≈0.00Å

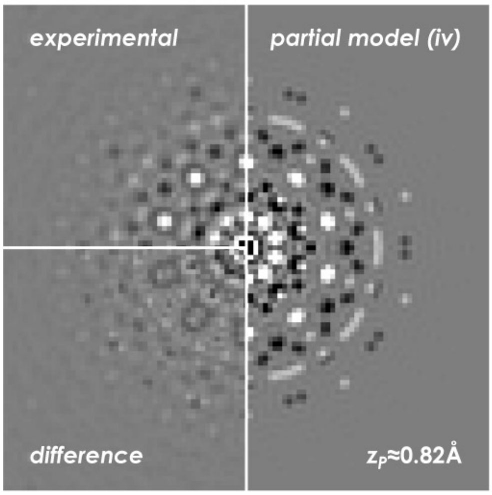
experimental
partial model (iv)
difference
z_P≈0.82Å

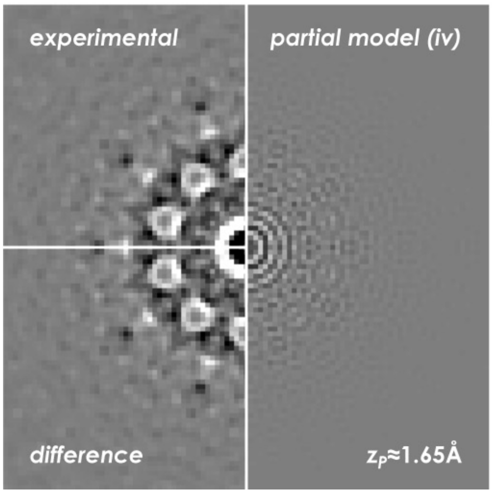
experimental
partial model (iv)
difference
z_P≈1.65Å

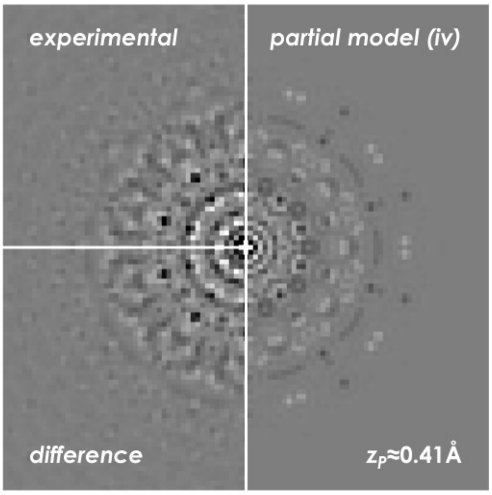
experimental
partial model (iv)
difference
z_P≈0.41Å

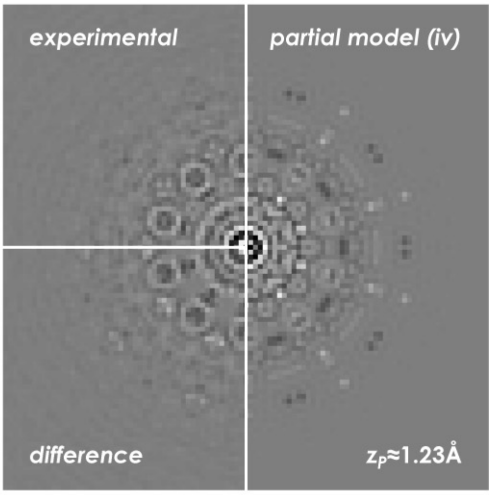
experimental
partial model (iv)
difference
z_P≈1.23Å

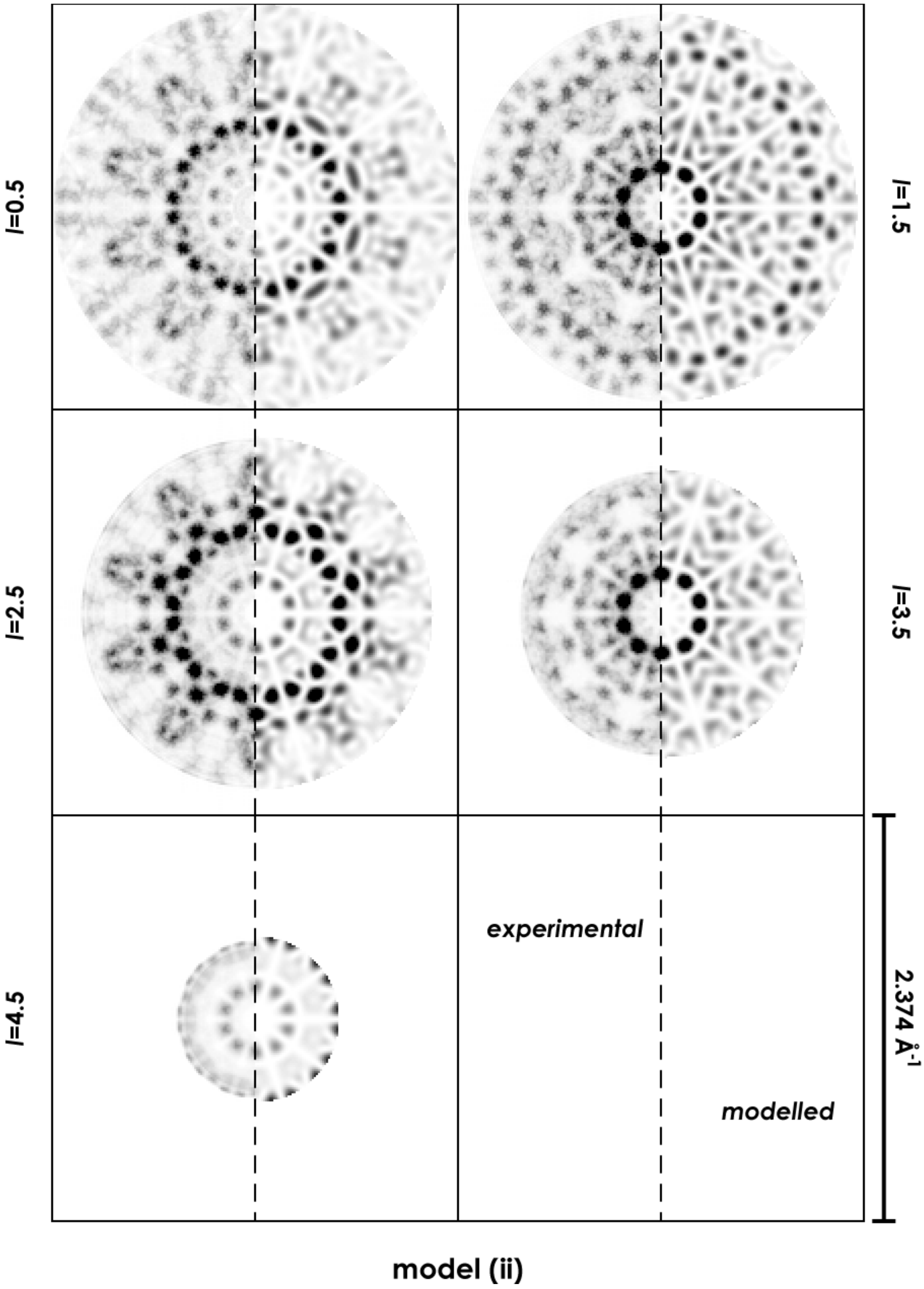
l=0.5
l=1.5
l=2.5
l=3.5
l=4.5
experimental
modelled
2.374 Å⁻¹
model (ii)

Figure 6.5 (pp. 90-92): Comparison of experimental and modelled diffuse X-ray scattering intensities in the interlayers of models (ii) to (iv) of *d*-Al–Cu–Co (*cf.* Fig. 4.6*b* and 4.9).

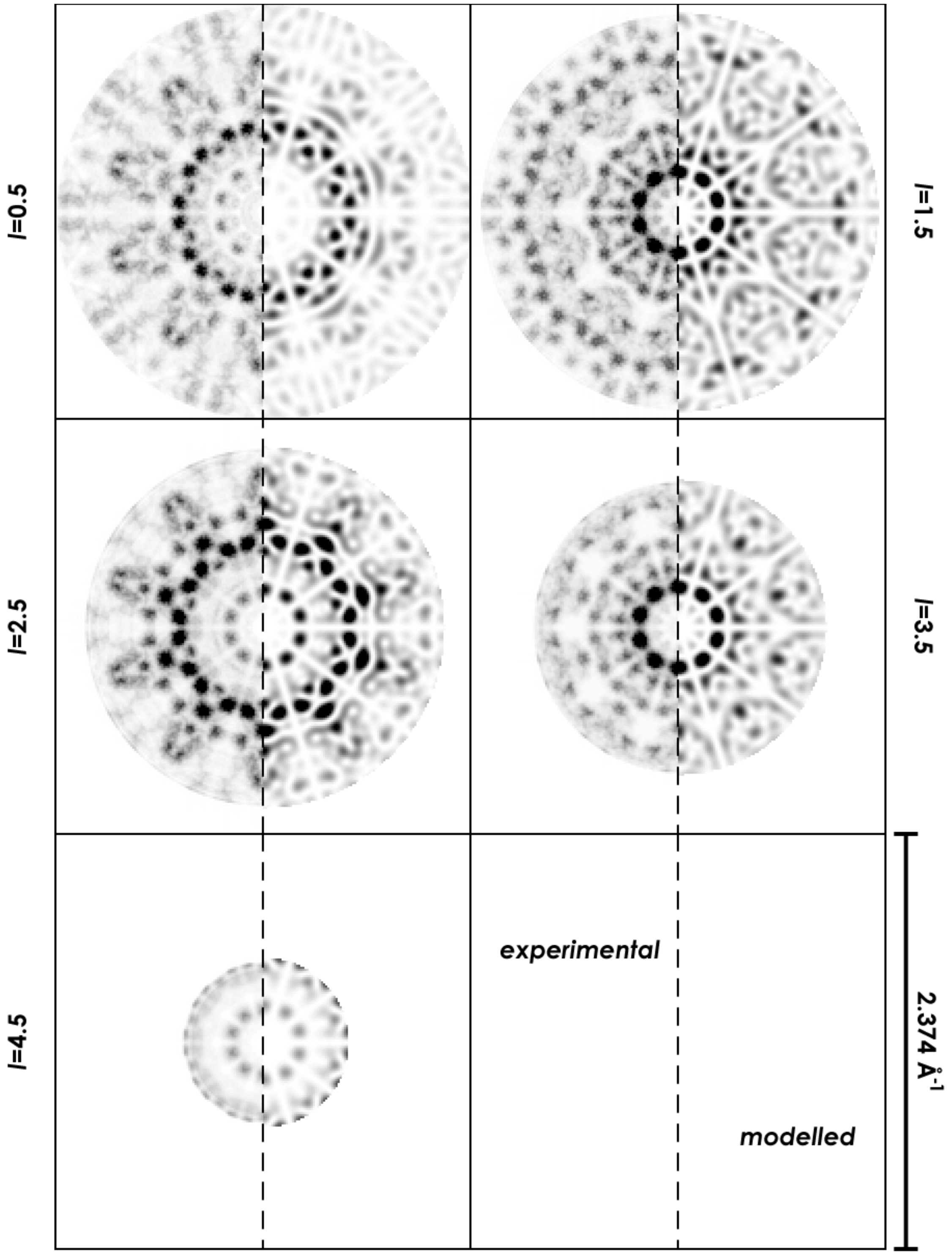

model (iii)

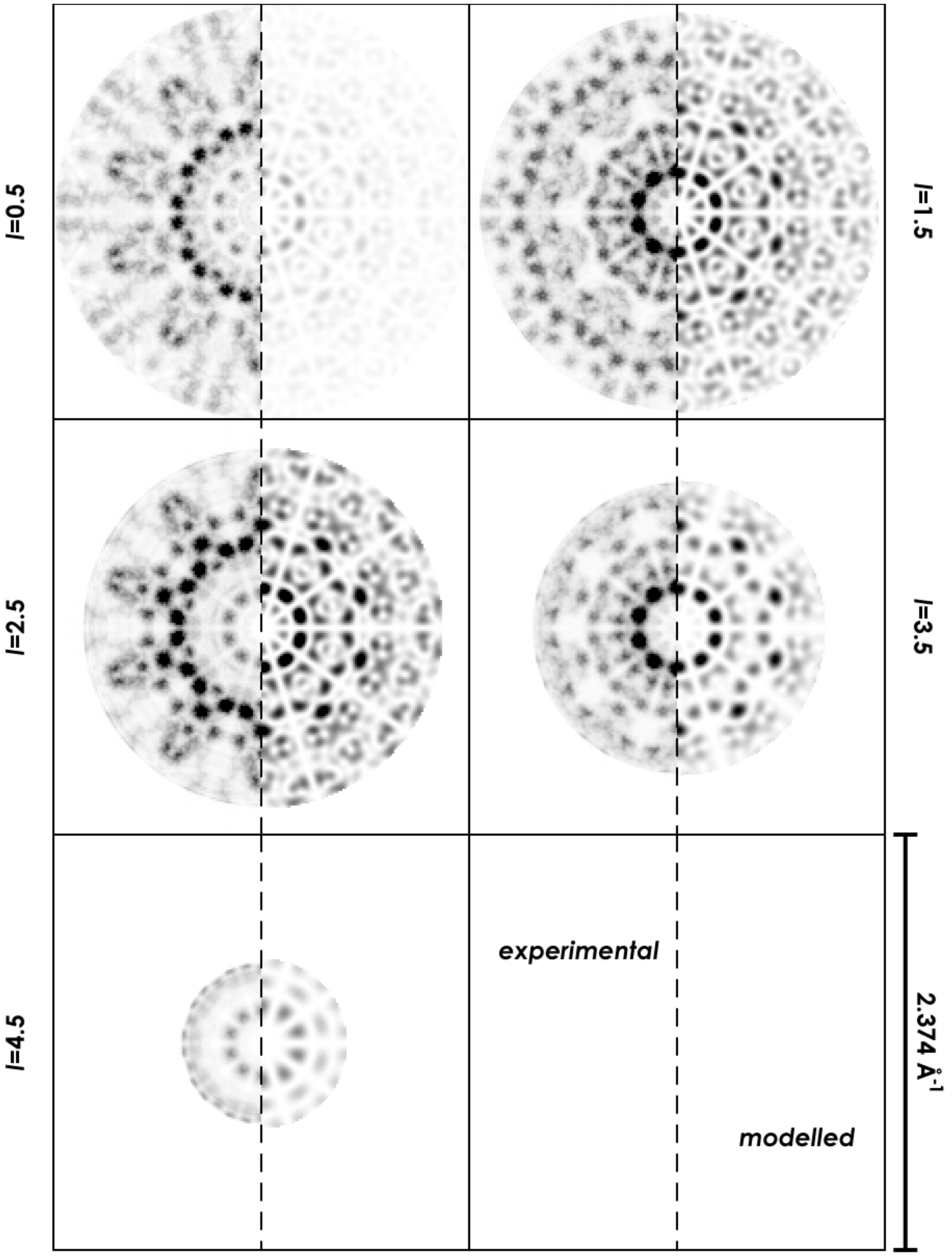
l=0.5
l=1.5
l=2.5
l=3.5
l=4.5
experimental
modelled
2.374 Å^{-1}

model (iv)

6.3. Analysis of the evolution of residual values and free model parameters during optimisation process

From Monte Carlo optimisation, it was reported that differential evolution technique is able to quickly confine the global minimum in a wide parameter search space. But in an advanced stage of refinement the performance becomes poor, because the probability of finding new better individuals decreases successively (Weber & Bürgi, 2002; Weber, 2005). This trend could also be confirmed in PDF optimisation.

The evolution of the averaged R_P values of the populations of the different partial model runs discussed above is shown in Fig. 6.6. In the initial population, the averaged R_P values were relatively high in all model runs (typically between 0.45 and 0.65), reflecting the wide range of allowed initial parameter values. At this initial stage, the variance of the population is high, and the averaged R_P of the whole population is considerably larger than R_P of the best individual found. With increasing number of generations, the mean R_P values decreased quickly in all model runs. The rate of decline depends on the number of free parameters refined and on the population size, but in all model runs R_P levels off after about 500 to 600 generations at the latest. The mean R_P values of the populations differed at this stage already less than 0.005 from the R_P values of the best individuals. Both, the R_P values of the best individuals and of the whole populations, decreased only slowly thenceforward. For instance in the "complete" model run (i), R_P of the best individual improved from 0.301 at generation 594 to 0.300 at generation 1401. In the same period, the mean R_P of the whole population sank from 0.303 to 0.300.

Refinements were stopped when the mean R_P did not improve for several hundred generations. Usually, this was the case after about 2000 generations. At this stage, all model parameters and R_P of the individuals of a population had converged, within experimental resolution, to the values of the best fit found.

During refinement, different groups of model parameters showed varying pathways of evolution (Fig. 6.7). The radial distances converged fastest towards the optimum value. In the refinement of model (i) these parameter levelled off after about 200-300 generations and converged completely before 1000 generations (Fig. 6.7*a*). The angular parameters as well as the attenuation parameter *a* needed about 200 additional generations to reach this stage, showing also slightly more fluctuating curves of their mean values (Figs. 6.7*b*,*d*). The latest convergence was found for the puckering heights (Fig. 6.7*c*) and the scattering weighting factors (Fig. 6.7*e*), the latter needed about 1500 generations to approach their final values. The late convergence and the remarkable oscillations of the mean values of the weighting factors during the refinement are in agreement with the observation that occupations cannot be assigned correctly unless the position of the respective atom sites is known at a high accuracy (see section 6.1).

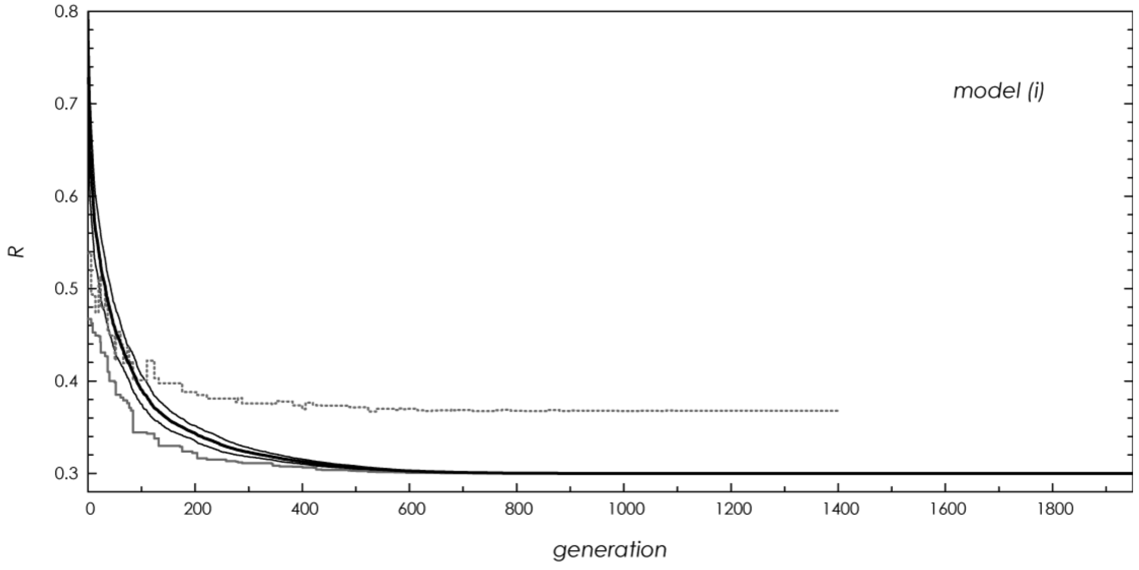

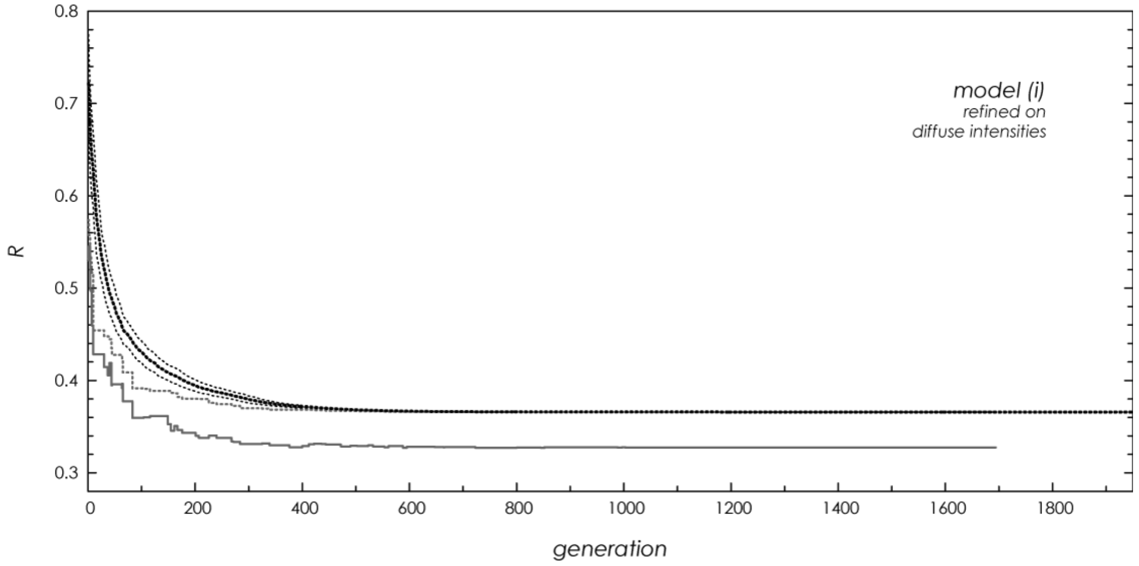

Figure 6.6 (pp. 94-95): Evolution of the reliability indices R_P and R_I in different model refinements as a function of the number of generations of the run. Thick black curves: mean R_P value (model (i) to (iv)) or R_I value (model optimised on diffuse intensities) of the whole population; thin black curves: standard deviation of R_P or R_I of the population; grey curves: R_P and R_I value of the current best individual found, the solid curve shows the R values which were used for the respective optimisation (R_P *or* R_I), the dashed curve shows the supplemental, unused variant. The end point of the grey curves indicates the generation in which the final best fit was found.

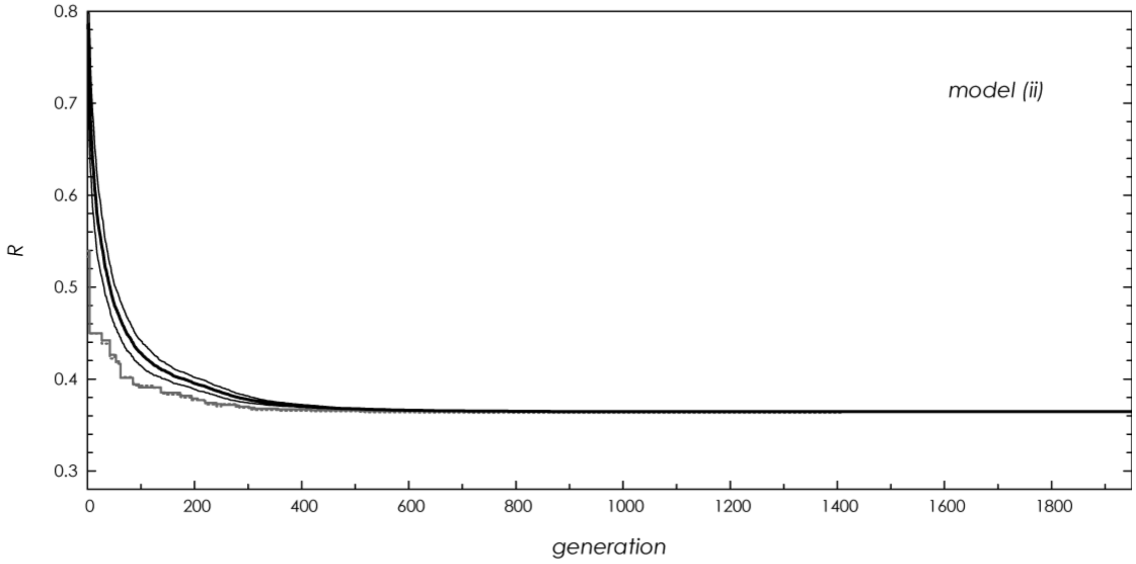
model (ii)
R
0.8
0.7
0.6
0.5
0.4
0.3
0
200
400
600
800
1000
1200
1400
1600
1800
generation

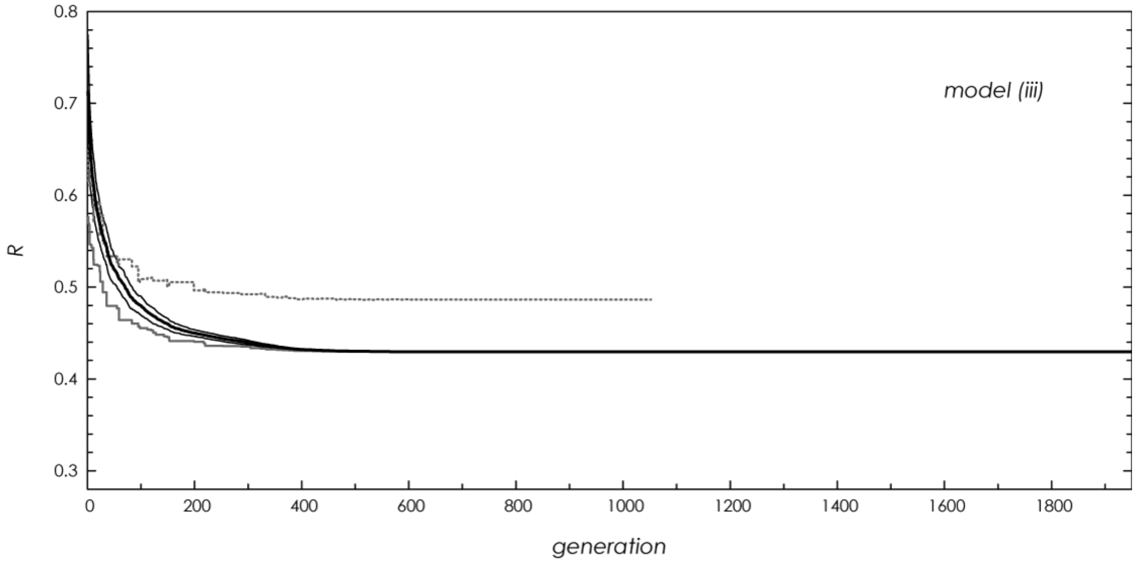
model (iii)
R
0.8
0.7
0.6
0.5
0.4
0.3
0
200
400
600
800
1000
1200
1400
1600
1800
generation

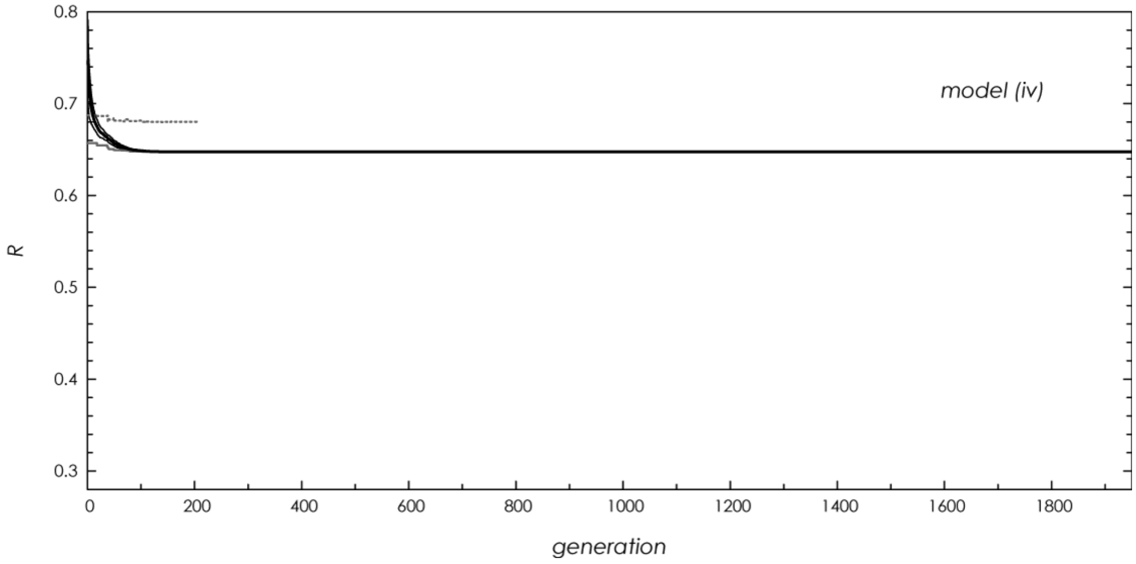
model (iv)
R
0.8
0.7
0.6
0.5
0.4
0.3
0
200
400
600
800
1000
1200
1400
1600
1800
generation

Differential evolution is a practicable method for optimising structural models in PDF space. Its strength is the fast but rough approximation of the optimum. For more efficiently finding the final solution, a combination of differential evolution with other optimisation methods may be favourable, *e.g.* with least-squares technique, which is more efficient in finding a minimum configuration in narrow, confined search spaces.

6.4. Model optimisation in reciprocal space

6.4.1. Objective and method

In the following, the results of optimisation based on PDF densities is compared to the also possible optimisation on diffuse scattering intensities, and the consequences on the obtained PDFs are discussed. For that reason, another independent model run of the "complete" model was performed (with identical setup and definitions of model parameters and parameter ranges), but instead of minimising the fitness of the ΔPDFs by R_P, the fitness was directly evaluated in reciprocal space using the scattering intensities of the diffuse interlayers.

Following eq. 4.17, the reliability indexes R_I and R_P are defined by

$$R_\mathrm{I} = R(I_{diffuse}(\mathbf{h})) = \sqrt{\frac{\sum\left(I^{obs}_{diffuse}(\mathbf{h}) - I^{calc}_{diffuse}(\mathbf{h})\right)^2}{\sum\left(I^{obs}_{diffuse}\right)^2}}, \tag{6.1}$$

and

$$R_\mathrm{P} = R(\Delta P(\mathbf{r})) = \sqrt{\frac{\sum\left(\Delta P^{obs}(\mathbf{r}) - \Delta P^{calc}(\mathbf{r})\right)^2}{\sum\left(\Delta P^{obs}\right)^2}}. \tag{6.2}$$

For the sake of simplicity, weighting and scaling factors of eq. 4.17 were skipped in the expressions above (nonetheless, they were included in calculations).

With Plancherel's theorem,

$$\int |f(\mathbf{h})|^2 d\mathbf{h} = \int |F(\mathbf{r})|^2 d\mathbf{r} \tag{6.3}$$

(here $F(\mathbf{r})$ is the Fourier transforms of $f(\mathbf{h})$), one obtains for the real-valued scattering intensities and PDF densities

$$\int I_{diffuse}(\mathbf{h})^2 d\mathbf{h} = \int \Delta P(\mathbf{r})^2 d\mathbf{r}. \tag{6.4}$$

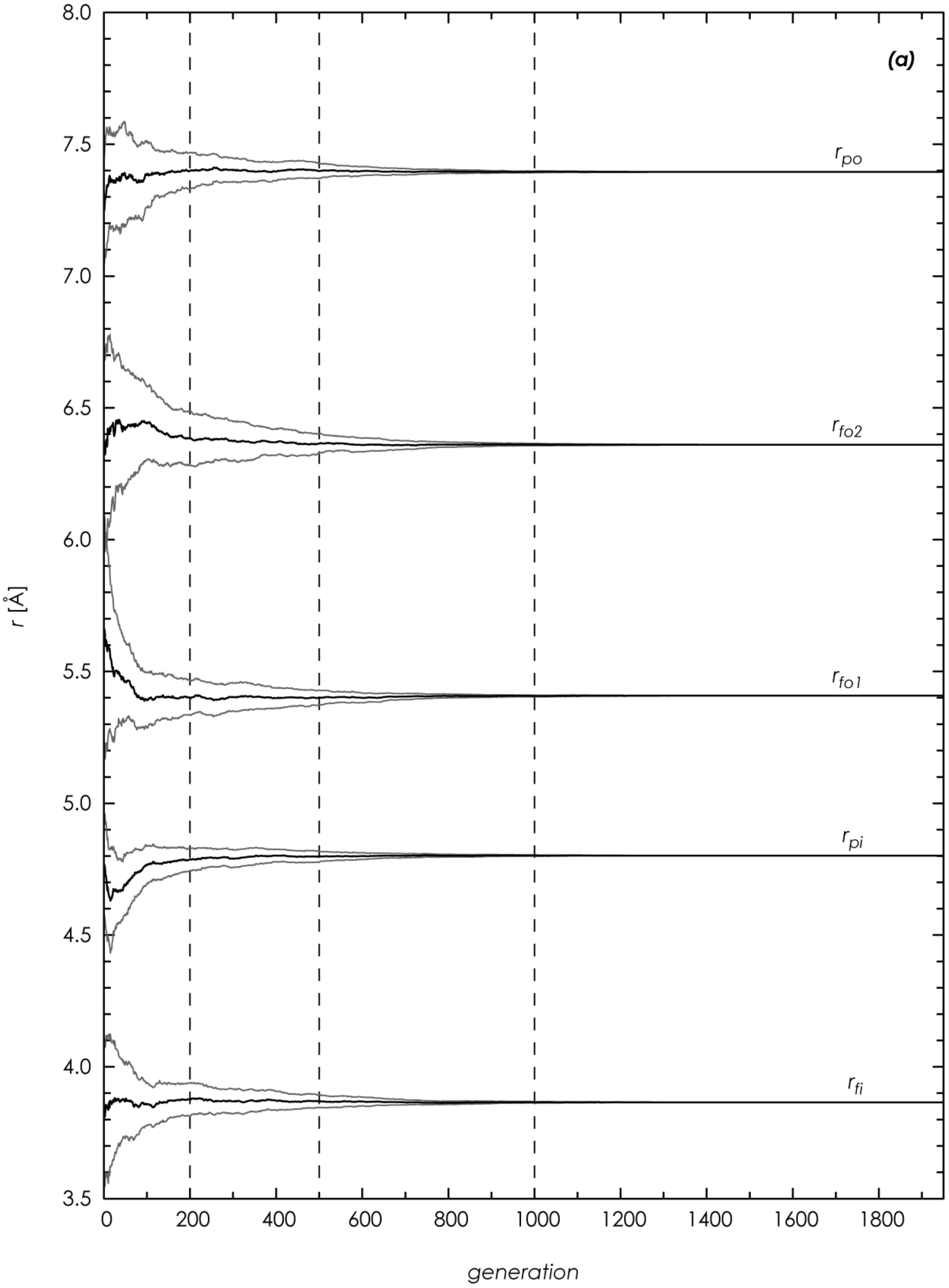

Figure 6.7 (pp. 97-100): Evolution of free model parameters as a function of the number of generations in the run of refinement of model (i). Black curves show the mean parameter values of the population, grey curves indicate their standard deviation of the population. (a) radial distances; (b) angles; (c) puckering heights; (d) exponential decay parameter; (e) scattering weighting factors. Vertical dashed lines at generation 200, 500, and 1000 help to facilitate the comparison between the curves.

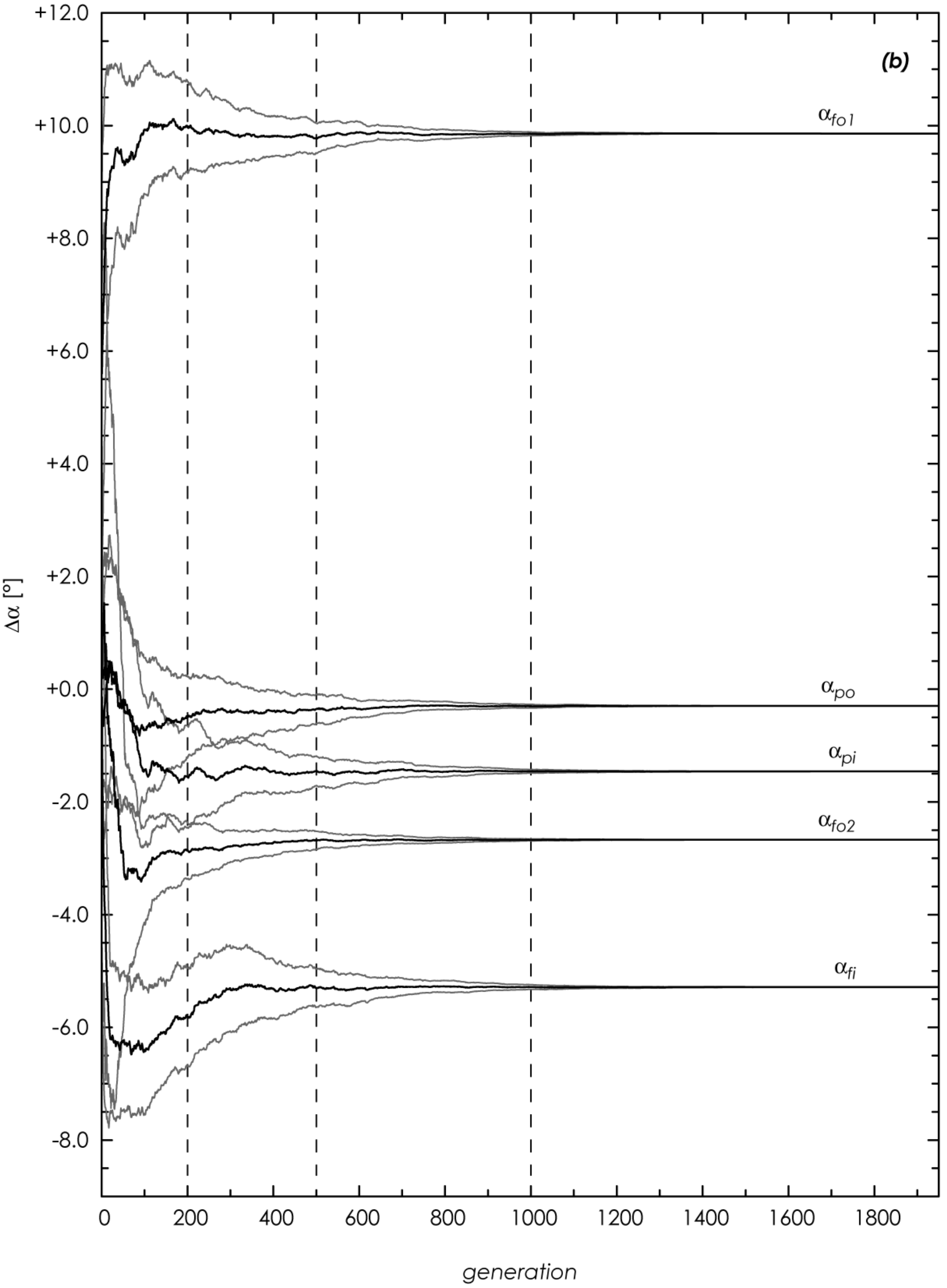
(b)
+12.0
+10.0
+8.0
+6.0
+4.0
+2.0
+0.0
-2.0
-4.0
-6.0
-8.0
Δα [°]
α_{fo1}
α_{po}
α_{pi}
α_{fo2}
α_{fi}
0
200
400
600
800
1000
1200
1400
1600
1800
generation

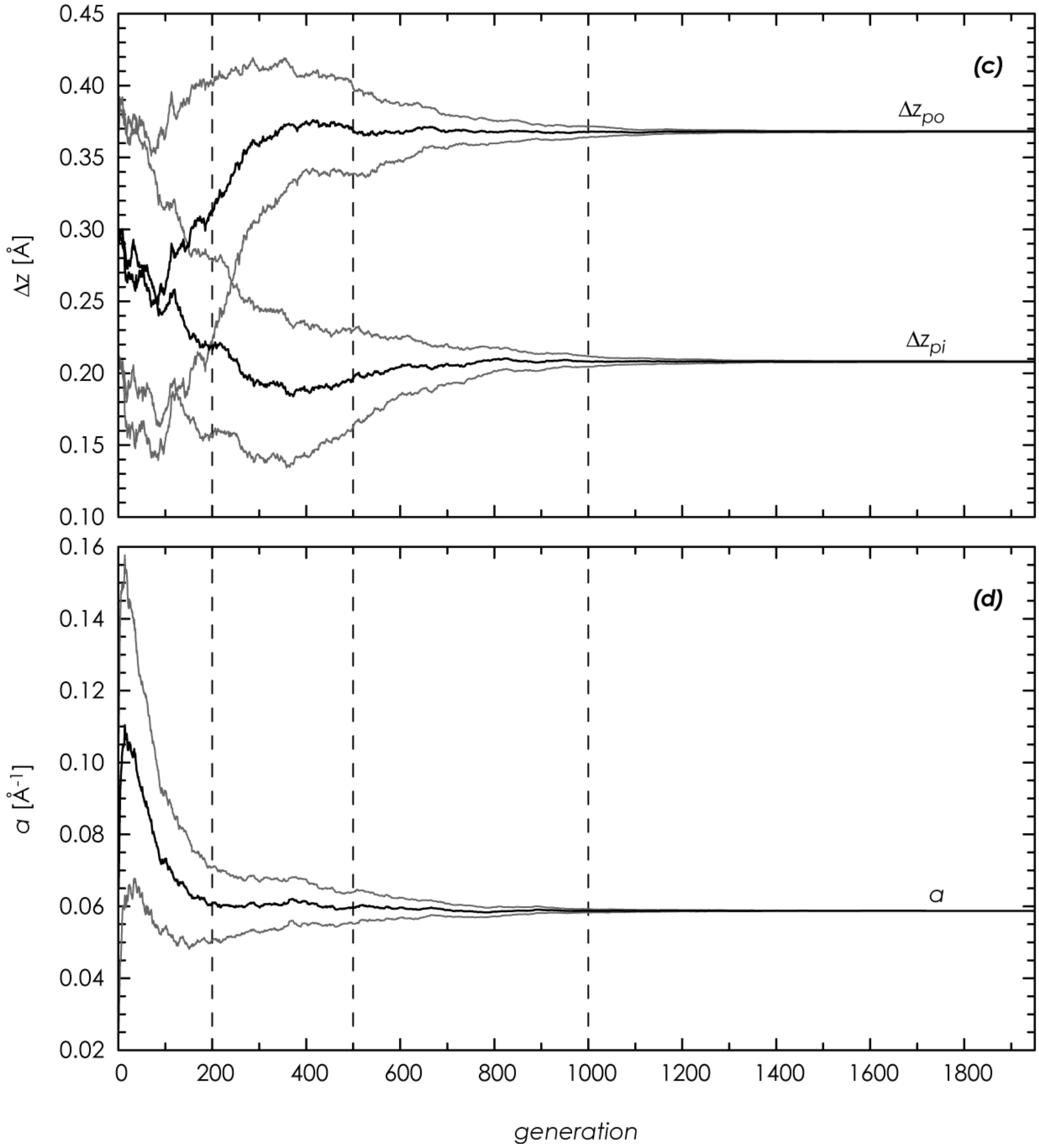
(c)
Δz [Å]
0.45
0.40
0.35
0.30
0.25
0.20
0.15
0.10
Δz_{po}
Δz_{pi}
(d)
a [Å^{-1}]
0.16
0.14
0.12
0.10
0.08
0.06
0.04
0.02
a
0
200
400
600
800
1000
1200
1400
1600
1800
generation

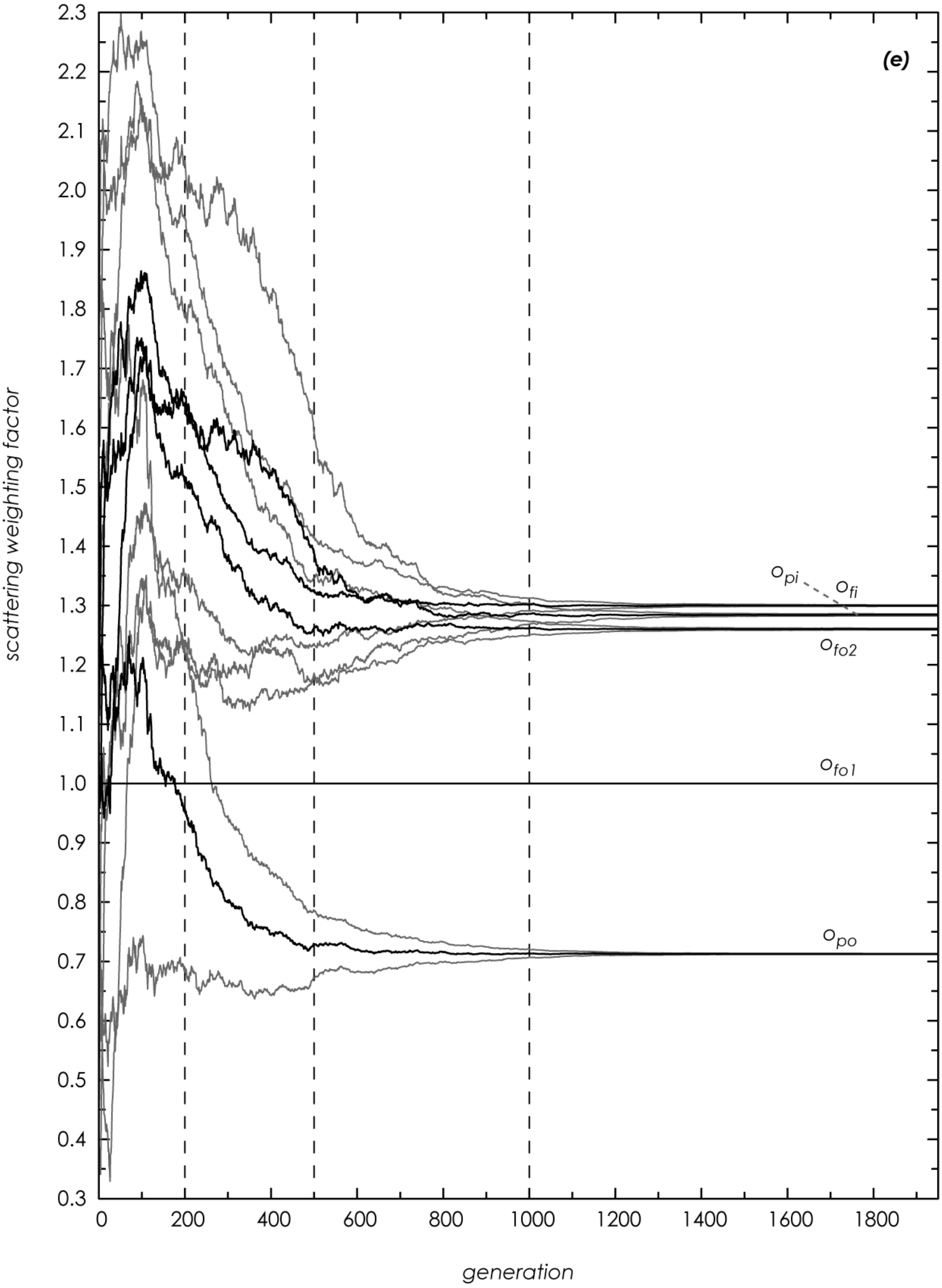
(e)
scattering weighting factor
generation
2.3
2.2
2.1
2.0
1.9
1.8
1.7
1.6
1.5
1.4
1.3
1.2
1.1
1.0
0.9
0.8
0.7
0.6
0.5
0.4
0.3
0
200
400
600
800
1000
1200
1400
1600
1800
o_{pi}
o_{fi}
o_{fo2}
o_{fo1}
o_{po}

For a discrete data representation eq. 6.4 simplifies to

$$\sum_n \left(I_{diffuse,n}^{obs}\right)^2 = \sum_n \left(\Delta P_n^{obs}\right)^2, \tag{6.5}$$

and

$$\sum_n \left(I_{diffuse,n}^{obs} - I_{diffuse,n}^{calc}\right)^2 = \sum_n \left(\Delta P_n^{obs} - \Delta P_n^{calc}\right)^2, \tag{6.6}$$

and as a consequence

$$R(I_{diffuse}(\mathbf{h}))=R(\Delta P(\mathbf{r})). \tag{6.7}$$

This means that for identical data, R_I and R_P are equal. Therefore also the global minima of R_I and R_P are identical, and any unbiased optimisation is expected to converge to the same parameter configuration for both types of refinement.

The calculation of R_I was carried out on the scattering intensities of the diffuse interlayers after the spherical mask was applied that simulated the detector envelope function (see section 4.3.5). In contrast to the calculation of R_P, the cylindrical attenuation function was not included, as this filter was applied directly on ΔPDF densities. Therefore, the results of the refinement optimised in reciprocal space should be compared to the PDF-optimised model (ii), which was optimised without inclusion of the exponential decay function (see section 6.2). Additionally, in the evaluation of R_P, the maximum considered correlation length within the quasiperiodic directions was limited by a cylindrical mask function of radius 16.6 Å (defined by means of the weighting factor w_i, see eq. 4.17).

6.4.2. Results and discussion

The model refinement against diffuse scattering intensities yielded a R_I value of 0.366. As expected, this value of R_I is nearly the same as the R_I values of model (i) ($R_\mathrm{I} = 0.368$) and of model (ii) ($R_\mathrm{I} = 0.363$) (see Table 6.1, Fig. 6.8), which were both optimised against R_P. In principle one could conclude that these three model solutions are all equivalent, thus. However, their R_P values differ significantly. (The differences between model (i) and model (ii), both refined against ΔPDF densities, were discussed above.) For the model optimised on diffuse scattering, two values of R_P were calculated, one without the exponential decay function, and one with $a = 0.059$ Å^{-1}, taken from the optimised model (i). When these two values are compared to the R_P values of the appropriate ΔPDF-optimised models, one finds in both cases a difference of more than 0.02. This means that, although the structural solutions have similar R_I values, optimising against the PDF yields better results in PDF space. This cannot be a general consequence of a better adaptation to model space, because the contrary is not the case, *i.e.* the model refined in reciprocal space does not show better R_I values than the model refined in PDF space. The reason for the advantage of PDF-space modelling may be found in the additional data weighting that was applied in PDF space. The cylindrical mask and, if applied, the cylindrical attenuation function focussed the optimisation onto structural representative short correlation lengths, whereas spurious long-distance signals, which cannot be covered by the spatially limited model structure, were ignored. Selective weighting of correlation lengths is, in principle, also possible in reciprocal space, but complex band-pass filters would be required to do so (*cf.* section 2.1.7). In PDF space, however, such filters are easy and straightforward to implement by simple data masking or scaling as a function of $\mathbf{r}$. As it was shown, they may help to increase the model quality significantly.

6.5. Model optimisation via an alternative fitness function

6.5.1. The structural similarity index

Besides the optimisation method also the choice of an appropriate fitness function is a crucial aspect in structural modelling. The general intention is to have a function that measures the closeness of the model to the observation. The fitness function governs the speed and accuracy of the model's convergence towards the observed data. Different definitions of the measure of agreement may lead to different results. A common group of fitness functions used in numerical models are functions that evaluate the differences between individual model and observation data points. Various ways of summation and normalisation of these differences, and diverse weighting schemes are possible. The reliability factor R used for optimising the structural model of disorder in *d*-Al–Cu–Co (eq. 4.17) is such a variant, which is well-established in crystallography. In order to test the reliability of R and the significance of the optimised model found, an alternative evaluation function was tested on the same structural model of *d*-Al–Cu–Co.

The *structural similarity index* (SSIM; Wang *et al.*, 2004), is uncommon in crystallography, and was originally developed for quality estimations in digital image processing. It was designed to give a numerical estimate of the human eye perception, including analyses of the overall quantities luminance, contrast and structure of a data representation. Unlike the R value, this index is not based on direct voxel-to-voxel differences. It rather uses statistical properties instead, *i.e.* global means, variances and the covariance. Although the method was primarily intended for use with 2D images, it can be applied to 3D data like the ΔPDF.

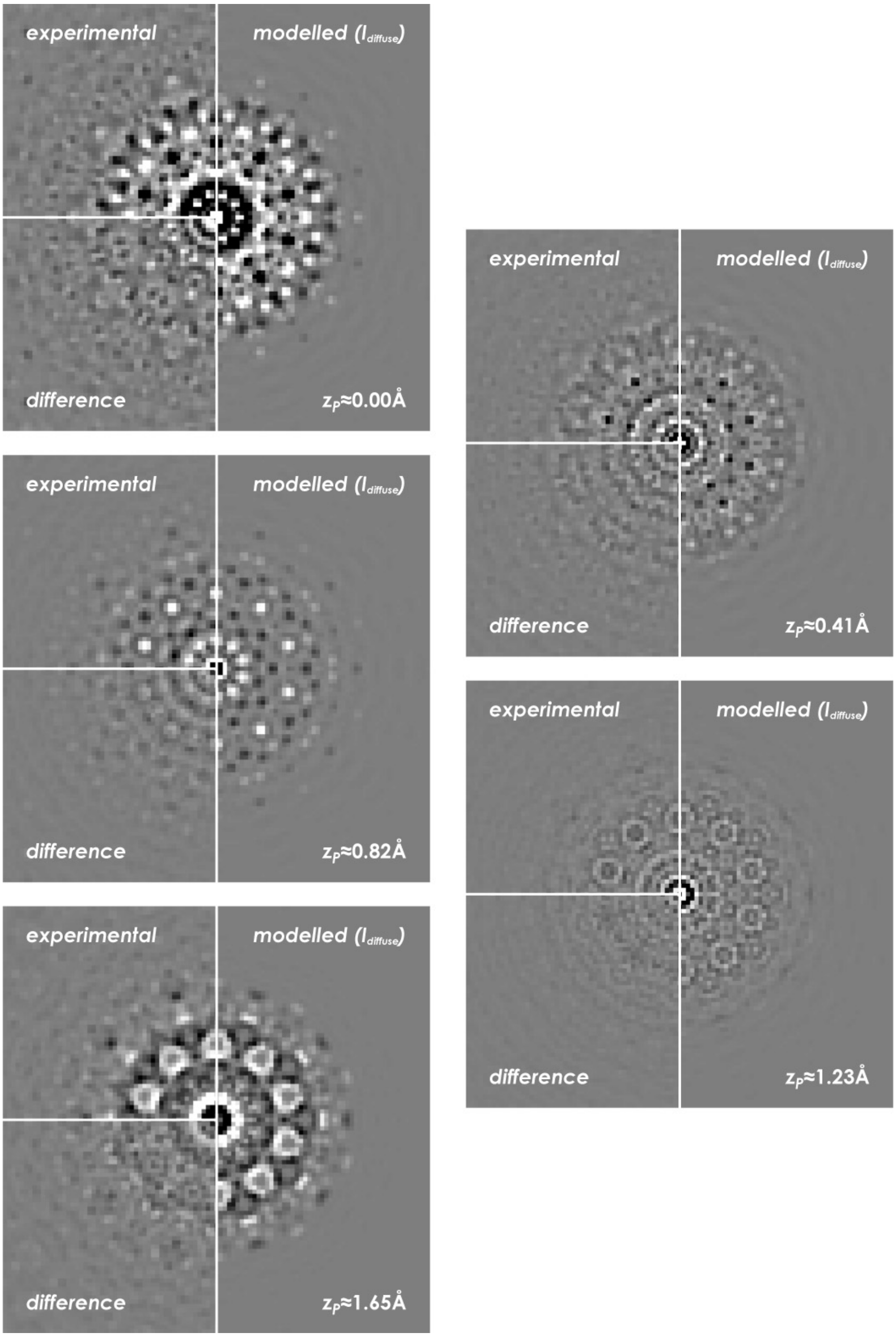

Figure 6.8: Comparison of of 2D (x_P,y_P)-sections through the experimental and the optimised modelled 3D-ΔPDF of the "complete" model (i) obtained by refinement based on diffuse scattering intensities ($I_{diffuse}$). In the lower left quadrant of each image, the difference between the experimental and the modelled 3D-ΔPDF is shown. Image sizes and the colouring scheme are the same as in Fig. 6.4.

The SSIM is defined as

$$SSIM = \frac{(2\mu_{obs}\mu_{calc} + C_1)(2\sigma_{obs,calc} + C_2)}{(\mu_{obs}^2 + \mu_{calc}^2 + C_1)(\sigma_{obs}^2 + \sigma_{calc}^2 + C_2)}. \qquad (6.8)$$

μ_{obs} and μ_{calc} are the arithmetic mean values of the observed and calculated ΔPDFs (wherein s is a scaling factor determined by least squares fitting, identical as in the calculation of R):

$$\mu_{obs} = \frac{\sum_{i=1}^{N} \Delta P_{obs,i}}{N}, \quad \mu_{calc} = \frac{\sum_{i=1}^{N} s\Delta P_{calc,i}}{N}. \qquad (6.9),\ (6.10)$$

σ_{obs} and σ_{calc} are the variance terms of the two ΔPDFs, and $\sigma_{obs,calc}$ is their covariance:

$$\sigma_{obs} = \frac{\sum_{i=1}^{N} (\Delta P_{obs,i} - \mu_{obs})^2}{N-1}, \quad \sigma_{calc} = \frac{\sum_{i=1}^{N} (s\Delta P_{calc,i} - \mu_{calc})^2}{N-1}, \qquad (6.11),\ (6.12)$$

and

$$\sigma_{obs,calc} = \frac{\sum_{i=1}^{N} (\Delta P_{obs,i} - \mu_{obs})(s\Delta P_{calc,i} - \mu_{calc})}{N-1}. \qquad (6.13)$$

The constant values C_1 and C_2 stabilise the value of the SSIM when its denominator becomes very small. $C_1 = (K_1 L)^2$ and $C_2 = (K_2 L)^2$. L is the dynamic range of the data, which was assigned here as the differences of the maximum and minimum value of ΔP_{obs}, *i.e.* $L = \Delta P_{max} - \Delta P_{min}$. K_1 and K_2 are arbitrary values; in the presented investigation they were chosen so that their order of magnitude was inverse to the dynamic range. They were set to $K_1 = 1 \cdot 10^{-7}$ and $K_2 = 3 \cdot 10^{-7}$. If data sets ΔP_{obs} and ΔP_{calc} are identical, the SSIM has value 1, otherwise it is less. For an extended discussion of the SSIM see Wang *et al.*(2004).

The "complete" structural model of disorder was refined by the use of the SSIM as fitness function. The starting model and the setup were identical as in the optimisation refined against R_P (see section 4.3.6). For consistency with R_P, the SSIM was minimised as 1 - *SSIM*.

6.5.2. Results and discussion

The model run converged to a minimum index value of 1 - *SSIM* = 0.0550. The optimised parameter values of the refinement are listed in Table 6.2. Fig. 6.9 shows the evolution of the fitness measured by the SSIM as a function of generations.

The general evolution of 1 - *SSIM* was similar to the evolution of R_P (*cf.* Fig. 6.6). There is a steep drop-off within the initial 100 to 200 generations. The final best individual was found after 1400 generations. The optimised model is equivalent to the optimised model found by means of R_P

(see Table 6.2). Aside from a few negligible small differences, the parameter values are all identical in both refinements. Only the scattering weighting factors show slight variances, which are rather a consequence of the susceptibility of these parameters to compensate minor displacements than of a significant inadequacy of the used fitness functions. The corresponding R_P value of the SSIM-based model is 0.300. Inversely, the R_P-based model (i) ($R_P = 0.300$) yields $1 - SSIM = 0.0550$. Accordingly the results are equivalent irrespective of which of the fitness functions, *R* or *SSIM*, was chosen for optimisation.

Hence, optimisation of difference structure models by differential evolution is not strongly governed by the choice of the fitness function. The characteristics of the progression of the model evolution were similar in both cases. It is somewhat surprising that optimisation by means of the SSIM, which is not based on direct pixel-wise comparison, yielded exactly the same result as the optimisation by means of *R*.

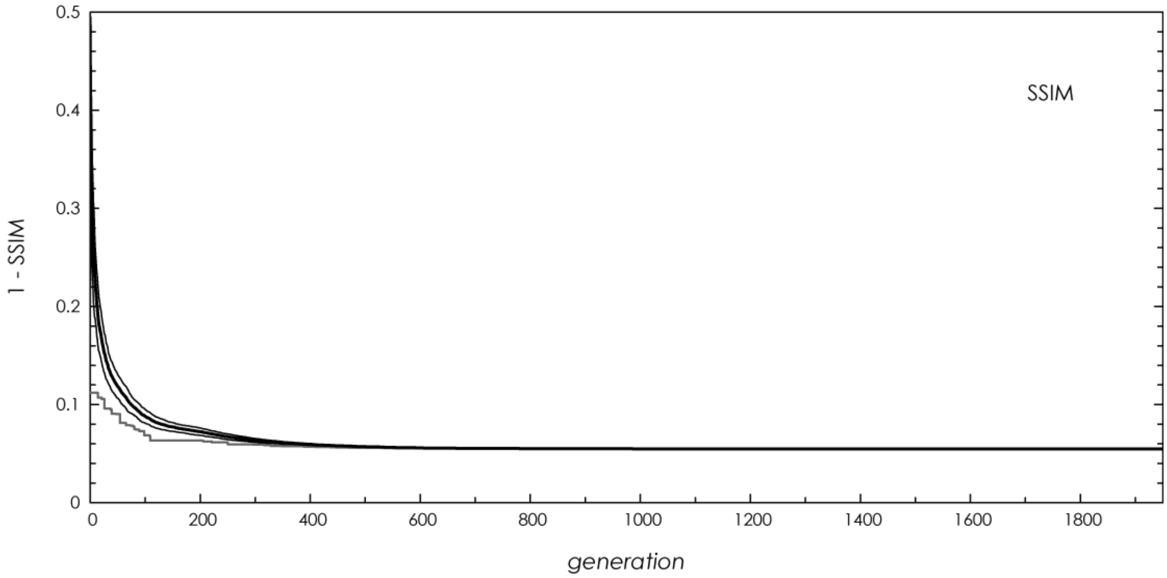

Figure 6.9: Evolution of the value 1 - *SSIM* in a refinement of the "complete" model (i) as a function of the number of generations of the run. The thick black curve shows the mean index value of the population, thin black lines indicate the standard deviation of the population. The grey curve shows the value of 1 - *SSIM* of the current best individual found.

Table 6.2: Comparison of the refined model parameters of the "complete" model (i) of *d*-Al–Cu–Co, optimised by the use of differential evolution based on R_P, and the parameters of a identical model refined based on the SSIM. For definitions of the model parameters see Fig. 4.7 and Table 4.1.

	R_P	*SSIM*
parameter		
r_{pi}	4.802 Å	4.801 Å
r_{po}	7.395 Å	7.394 Å
Δz_{pi}	0.208 Å	0.209 Å
Δz_{po}	0.368 Å	0.369 Å
α_{pi}	-1.46°	-1.46°
α_{po}	-0.29°	-0.29°
r_{fo1}	5.407 Å	5.408 Å
r_{fo2}	6.360 Å	6.361 Å
α_{fo1}	9.86°	9.86°
α_{fo2}	-2.67°	-2.67°
r_{fi}	3.866 Å	3. 865 Å
α_{fi}	-5.29°	-5.29°
a	0.059 Å^{-1}	0.059 Å^{-1}
o_{po}	0.712	0.711
o_{fo2}	1.259	1.259
o_{fo1}	*1.000* [1]	*1.000* [1]
o_{pi}	1.284	1.298
o_{fi}	1.297	1.282
minimal value	$R_\mathrm{P} = 0.300$	1 - *SSIM* = 0.0550
best individual 1st time found in generation		
	1401	1400
population size		
	150	150

[1] fixed value

7. Summary & Outlook

7. SUMMARY & OUTLOOK

7.1. 3D-ΔPDF analysis and modelling

In this work concepts of 3D-PDF analysis, and in particular 3D-ΔPDF analysis were illustrated. The usability of 3D-ΔPDF analysis was demonstrated on two example structures. The obtained results reveal that 3D-ΔPDF method has great potential for further applications. In principle ΔPDF analysis can be applied on any disordered crystal structure. The conditions that have to be fulfilled in practice are that the crystal possesses an average structure that is sufficiently known, and that the diffraction pattern shows diffuse scattering intensities that can be separated from Bragg intensities in some way. Qualitative 3D-ΔPDF analysis yielded meaningful results for both of the investigated structures. It is, hence, a promising tool, which could become a standard method in characterisation of disordered single crystal structures.

The practical application of difference structure modelling by 3D-ΔPDF fitting could be shown on the characterisation of a disordered prototype cluster of *d*-Al–Cu–Co. Although the model optimisation by means of differential evolution yielded significant results, the method still suffers from the performance of the optimisation becoming poor with increasing number of generations. An improved optimisation process, *e.g.* by a combination of differential evolution with least squares techniques, is required for a broad and effective usage of this method. Another limiting point in ΔPDF modelling is the high demand on computing power and memory capacity. For instance, the modelled 3D-ΔPDF of *d*-Al–Cu–Co contained 800'000 discrete density values, which were computed from a scattering data set of the same size. By the use of the highly efficient *FFTW* software library (Frigo & Johnson, 2005) time consumption of the Fourier transform was comparable small for a single data set. But in the complete process of the refinement, it took 1401 generations with 150 data representations of individuals in each to reach the optimal fit, *i.e.* $1.68 \cdot 10^{11}$ voxel values with PDF densities, making up 626 gigabyte of single precision floating point values, had to be computed. Apart from the expense for computing firstly the diffraction patterns and subsequently Fourier transforming them, this huge amount of data also causes bottlenecks in the computer's data bus, in memory allocation and in *I*/*O*-processes. For truly continuous 3D scattering intensities, which are not constricted to a layered distribution in reciprocal space as it was the case for *d*-Al–Cu–Co and *N,N',N''*-tris-*t*-butyl-1,3,5-benzene tricarboxamide, the amount of scattering data increases by several orders of magnitude. For a regular application of ΔPDF modelling, adjustments and enhancements in software design are strongly required, thus. The continual improvement of computing resources may facilitate this process, though. A possibility to improve computing performance of model optimisation is to parallelise the computations on a cluster of processors. In differential evolution optimisation it is an easy task to distribute the computations of the independent individuals to separate processors, as it was partially realised in the optimisation process of *d*-Al–Cu–Co (see section 4.3.6). On the level of individuals it is additionally possible to parallelise the Fourier Transform of the 3D scattering intensities as a distributed-memory transform on multiple processors. High-performance algorithms for parallel 3D transforms are available (*e.g.* Brass & Pawley, 1986; Takahashi, 2003, and references therein).

The simple *"punch-and-fill"* filter implementation applied to eliminate Bragg peaks uses a fixed punch window and an isotropic fill function. However, treatment of complex scattering features, such as weak diffuse scattering beneath strong Bragg peaks, or superposition of Bragg peaks with narrow diffuse streaks, also requires enhanced data filters for the extraction of diffuse intensities.

In principle it is possible to develop ΔPDF analysis and modelling further to an *ab initio* method, which sets up a complete model of disorder starting from a suggested average structure, without any further assistance. For this approach, additional techniques for automated assignment of vectors in PDF space to structural features in real space have to be available. This could be done either on a computationally intensive trial-and-error basis, or by fully developed, but complex to implement, pattern recognition algorithms.

7.2. Total scattering 3D-PDF analysis and modelling

In this work, the practical application of total scattering 3D-PDF analysis was not addressed. Nevertheless, also this approach has great potential for future research. Principles and concepts of total scattering 3D-PDF analyses are mainly the same as discussed for the ΔPDF, except that the separation of Bragg and diffuse scattering intensities is omitted. The field of possible applications of 3D-PDF analysis is wide, comprising for instance: refinement of disorder in crystalline phases having diffraction patterns in which Bragg and diffuse scattering cannot be separated satisfactorily; direct refinement of the real structure of crystalline phases, including simultaneously features of the average structure and the difference structure; or the investigation of non-crystalline phases that show any kind of internal structural anisotropy (*e.g.* paracrystals). Many of such materials are nowadays examined by 1D (powder) PDF methods. 3D-PDF analysis might provide a direct access to the 3D structure of these materials and reveal additional structural information, which is not accessible with 1D techniques. However, 3D-PDF analysis is only applicable if samples of sufficient size and with macroscopic anisotropy are available.

In order to allow collecting strong Bragg and weak diffuse scattering intensities at the same time even if the signals lie close together, data collection for total scattering 3D-PDF analysis requires detector systems that cover the full dynamic range of the diffraction intensities of the sample, and that have low intrinsic noise and a narrow point spread function. Such measurements become possible with recent area detectors such as the *PILATUS* detector system (Weber *et al.*, 2008; Kraft *et al.*, 2009).

7.3. Disorder in *N,N',N''*-tris-*t*-butyl-1,3,5-benzene tricarboxamide

On the example of *N,N',N''*-tris-*t*-butyl-1,3,5-benzene tricarboxamide it could be demonstrated that qualitative interpretation of the 3D-ΔPDF is an expedient and easy-to-use method for deriving a qualitative model of disorder based on a well-known average structure. Investigation in PDF space allowed straightforwardly linking pair correlation vectors to structural features in real space.

The qualitative results on *N,N',N''*-tris-*t*-butyl-1,3,5-benzene tricarboxamide reported in chapter 3 serve as a solid basis for further structural investigations of this compound. There will be a refined structural description published in a forthcoming paper (Simonov *et al.*, in preparation). This model of disorder allows for lateral displacements of the molecular columns, and for atomic displacement parameters. Correlation parameters across seven molecular shells were refined by least squares optimisation of the 3D-ΔPDF.

7.4. Disorder in *d*-Al–Cu–Co and other decagonal quasicrystals

In the study on *d*-Al–Cu–Co, a prototypic disordered structural motif could be identified, even though disorder phenomena in this quasicrystal are complex, and knowledge on the average structure was limited. Although the structural description of decagonal quasicrystals is embedded in 5D space, the disordered twofold superstructure could be characterised with a 3D method in 3D space. The presented structural model of disorder (see chapter 4) is the most accurate known description of a disordered motif in a decagonal quasicrystal so far. Nevertheless, many questions about the structure, formation and stabilisation of *d*-Al–Cu–Co and decagonal quasicrystals in general remain open, and further investigations are required. With regard to *d*-Al–Cu–Co, PDF analysis of the thermal evolution could reveal additional information on the stability and alterations of disordered structural motifs (cf. Weber *et al.*, 2004, for a study on temperature dependence of *d*-Al–Ni–Co). Additional analysis of the weak medium-range pair correlation peaks longer than ~14.5Å, which were ignored so far in ΔPDF analysis, could elucidate the relations between distinct disordered motifs.

A comparative study of ΔPDFs of different decagonal phases, particularly *d*-Al–Ni–Co, would surely be greatly beneficial to the universal understanding of decagonal quasicrystals.

References

For references cited in *chapters 3 and 4* see the references sections there.

Billinge, S. J. L. (2008). *J. Solid State Chem.* **181**, 1695-1700.

Billinge, S. J. L., DiFrancesco, R. G., Kwei, G. H., Neumeier, J. J. & Thompson, J. D. (1996). *Phys. Rev. Lett.* **77**, 715-718.

Black, P. J. (1955). *Acta Cryst.* **8**, 43-48.

Borie, B. & Sparks, C. J. (1971). *Acta Cryst. A* **27**, 198-201.

Bozin, E. S., Kwei, G. H., Takagi, H. & Billinge, S. J. L. (2000). *Phys. Rev. Lett.* **84**, 5856-5859.

Bracewell, R. N. (1983). *Journal of the Optical Society of America* **73**, 1832-1835.

Bracewell, R. N. (1984). *Proceedings of the IEEE* **72**, 1010-1018.

Brass, A. & Pawley, G. S. (1986). *Parallel Computing* **3**, 167-184.

Bürgi, H. B., Hostettler, M., Birkedal, H. & Schwarzenbach, D. (2005). *Z. Kristallogr.* **220**, 1066-1075.

Burkov, S. E. (1993). *Phys. Rev. B: Condens. Matter* **47**, 12325-12328.

Burnett, R. M. & Rossmann, M. G. (1971). *Acta Cryst. B* **27**, 1378-1387.

Butler, B. D. & Welberry, T. R. (1993). *Acta Cryst. A* **49**, 736-743.

Cowley, J. M. (1995). *Diffraction physics*, Third rev. ed. Amsterdam: Elsevier.

Deloudi, S. (2008). PhD thesis*,* ETH Zürich.

Dove, M. T., Keen, D. A., Hannon, A. C. & Swainson, I. P. (1997). *Phys. Chem. Miner.* **24**, 311-317.

Egami, T. & Billinge, S. J. L. (2003). *Underneath the Bragg peaks: structural analysis of complex materials*. New York: Pergamon.

Frey, F. (1995). *Acta Cryst. B* **51**, 592-603.

Frey, F. (2000). *Mater. Sci. Eng., A* **294**, 178-185.

Frey, F. (2003). *Lecture Notes in Physics* **610**, 133-166.

Frey, F. & Steurer, W. (1993). *J. Non-Cryst. Solids* **153**, 600-605.

Frey, F. & Weidner, E. (2003). *Z. Kristallogr.* **218**, 160-169.

Frigo, M. & Johnson, S. G. (2005). *Proceedings of the IEEE* **93**, 216-231.

Guinier, A. & Griffoul, R. (1948). *Acta Cryst.* **1**, 188-193.

Hao, H. & Bracewell, R. N. (1987). *Proceedings of the IEEE* **75**, 264-266.

Harker, D. (1936). *J. Chem. Phys.* **4**, 381-390.

Hendricks, S. & Teller, E. (1942). *J. Chem. Phys.* **10**, 147-167.

Jeong, I. K., Proffen, T., Mohiuddin-Jacobs, F. & Billinge, S. J. L. (1999). *J. Phys. Chem. A* **103**, 921-924.

Kabsch, W. (1993). *J. Appl. Cryst.* **26**, 795-800.

Keen, D. A. (2001). *J. Appl. Cryst.* **34**, 172-177.

Kobas, M., Weber, T. & Steurer, W. (2005). *Phys. Rev. B: Condens. Matter* **71**, 224205.

Kopský, V. & Litvin, D. B. (2010). Editor. *Subperiodic Groups*, 2nd ed. Chicester: John Wiley & Sons, Ltd.

Kraft, P., Bergamaschi, A., Broennimann, C., Dinapoli, R., Eikenberry, E. F., Henrich, B., Johnson, I., Mozzanica, A., Schleputz, C. M., Willmott, P. R. & Schmitt, B. (2009). *J. Synchrotron Rad.* **16**, 368-375.

Lonsdale, K. (1948). *Acta Cryst.* **1**, 12-20.

Louca, D. & Egami, T. (1999). *Phys. Rev. B: Condens. Matter* **59**, 6193-6204.

McGreevy, R. L. (2001). *J. Phys.: Condens. Matter* **13**, R877-R913.

McGreevy, R. L. & Pusztai, L. (1988). *Molecular Simulation* **1**, 359-367.

Metropolis, N., Rosenbluth, A. W., Rosenbluth, M. N., Teller, A. H. & Teller, E. (1953). *J. Chem. Phys.* **21**, 1087-1092.

Neder, R. B. & Korsunskiy, V. I. (2005). *J. Phys.: Condens. Matter* **17**, S125-S134.

Nield, V. M., Keen, D. A. & Mcgreevy, R. L. (1995). *Acta Cryst. A* **51**, 763-771.

Nordman, C. E. & Nakatsu, K. (1963). *JACS* **85**, 353-354.

Patterson, A. L. (1934). *Physical Review* **46**, 372-376.

Patterson, A. L. (1935). *Z. Kristallogr.* **90**, 517-542.

Petkov, V., DiFrancesco, R. G., Billinge, S. J. L., Acharya, M. & Foley, H. C. (1999). *Philos. Mag. B* **79**, 1519-1530.

Proffen, T. & Billinge, S. J. L. (1999). *J. Appl. Cryst.* **32**, 572-575.

Proffen, T., Billinge, S. J. L., Egami, T. & Louca, D. (2003). *Z. Kristallogr.* **218**, 132-143.

Proffen, T. & Kim, H. (2009). *J. Mater. Chem.* **19**, 5078-5088.

Proffen, T. & Welberry, T. R. (1997). *Acta Cryst. A* **53**, 202-216.

Proffen, T. & Welberry, T. R. (1998). *Phase Transitions* **67**, 373-397.

Schaub, P., Weber, T. & Steurer, W. (2007). *Philos. Mag.* **87**, 2781-2787.

Schaub, P., Weber, T. & Steurer, W. (2011). *J. Appl. Cryst.* **44**, accepted.

Simonov, A., Weber, T., Schaub, P. & Steurer, W. (in preparation).

Steurer, W. & Deloudi, S. (2009). *Crystallography of quasicrystals: concepts, methods and structures*. Berlin: Springer.

Steurer, W. & Frey, F. (1998). *Phase Transitions* **67**, 319-361.

Steurer, W. & Kuo, K. H. (1990). *Acta Cryst. B* **46**, 703-712.

Takahashi, D. (2003). *Comput. Phys. Commun.* **152**, 144-150.

Toby, B. H. & Egami, T. (1992). *Acta Cryst. A* **48**, 336-346.

von Laue, M. (1918). *Annalen der Physik* **56**, 497-506.

von Laue, M. (1941). *Röntgenstrahl-Interferenzen*. Leipzig: Akademische Verlagsgesellschaft Becker & Erler.

Wang, Z., Bovik, A. C., Sheikh, H. R. & Simoncelli, E. P. (2004). *IEEE Transactions on Image Processing* **13**, 600-612.

Warren, B. E., Averbach, B. L. & Roberts, B. W. (1951). *J. Appl. Phys.* **22**, 1493-1496.

Weber, T. (2005). *Z. Kristallogr.* **220**, 1099-1107.

Weber, T. & Bürgi, H. B. (2002). *Acta Cryst. A* **58**, 526-540.

Weber, T., Deloudi, S., Kobas, M., Yokoyama, Y., Inoue, A. & Steurer, W. (2008). *J. Appl. Cryst.* **41**, 669-674.

Weber, T., Kobas, M. & Steurer, W. (2004). *Ferroelectrics* **305**, 213-216.

Weber, T. & Steurer, W. (2008). *Z. Kristallogr.* **223**, 833-838.

Welberry, T. R. (2009). *Diffuse x-ray scattering and models of disorder*, Reprinted ed. New York: Oxford University Press.

Welberry, T. R. & Butler, B. D. (1994). *J. Appl. Cryst.* **27**, 205-231.

Welberry, T. R. & Butler, B. D. (1995). *Chem. Rev.* **95**, 2369-2403.

Welberry, T. R. & Proffen, T. (1998). *J. Appl. Cryst.* **31**, 309-317.

Welberry, T. R., Proffen, T. & Bown, M. (1998). *Acta Cryst. A* **54**, 661-674.

Acknowledgements

'Begin at the beginning,' the King said gravely, 'and go on till you come to the end: then stop.'

Lewis Caroll, *Alice's Adventures in Wonderland*, 1865

I would like to express my gratitude to everybody who contributed – actively or passively –to the development of this doctoral thesis. In particular, I want to thank:

- Prof. Walter Steurer for supervising the thesis.
- Dr. Thomas Weber for supervising the thesis and for always being present with useful advice. He contributed many ideas to this work, which were mostly fruitful, but sometimes just stressful.
- Prof. Reinhard Neder, University of Erlangen, for co-examining the thesis.
- All members of the Laboratory of Crystallography at ETH Zürich for supporting me in all kinds of situations, and especially for the warm, friendly, and even familiar atmosphere.

Curriculum Vitae

Philippe Schaub

born 3rd June 1978 in Basel, Switzerland

1985 - 1989	Primary school, Basel, Switzerland
1989 - 1997	Grammar school (*Gymnasium*), Basel, Switzerland
1997 - 2004	Diploma studies in Earth Sciences, University of Basel, Switzerland. Diploma thesis: "Spektrometrische Untersuchungen an Al-Spinellen" under supervision of Prof. H.A. Hänni, Institute of Mineralogy & Petrography; and "Geologische Kartierung im Gebiet 'Stürmen' (Laufen, BL)" under supervision of PD Dr. P.G. Jordan.
2005 - 2010	Doctoral studies at Laboratory of Crystallography, ETH Zürich, Switzerland. Thesis: "Three-dimensional Pair Distribution Function analysis of disordered crystals" under supervision of Prof. W. Steurer and Dr. Th. Weber.
